

GPO PRICE \$ _____

CFSTI PRICE(S) \$ _____

Hard copy (HC) 3.00

Microfiche (MF) .65

ff 653 July 65

39

RECEIVED
JUN 21 12 33 PM '68
OFFICE OF
UNIVERSITY AFFAIRS

CORNELL UNIVERSITY

Center for Radiophysics and Space Research

RESEARCH REPORT RS-73

Radar Studies of the Lunar Surface Emphasizing Factors Related to Selection of Landing Sites

April 1968

FACILITY FORM 602

N 68-31594

(ACCESSION NUMBER)

(THRU)

(PAGES)

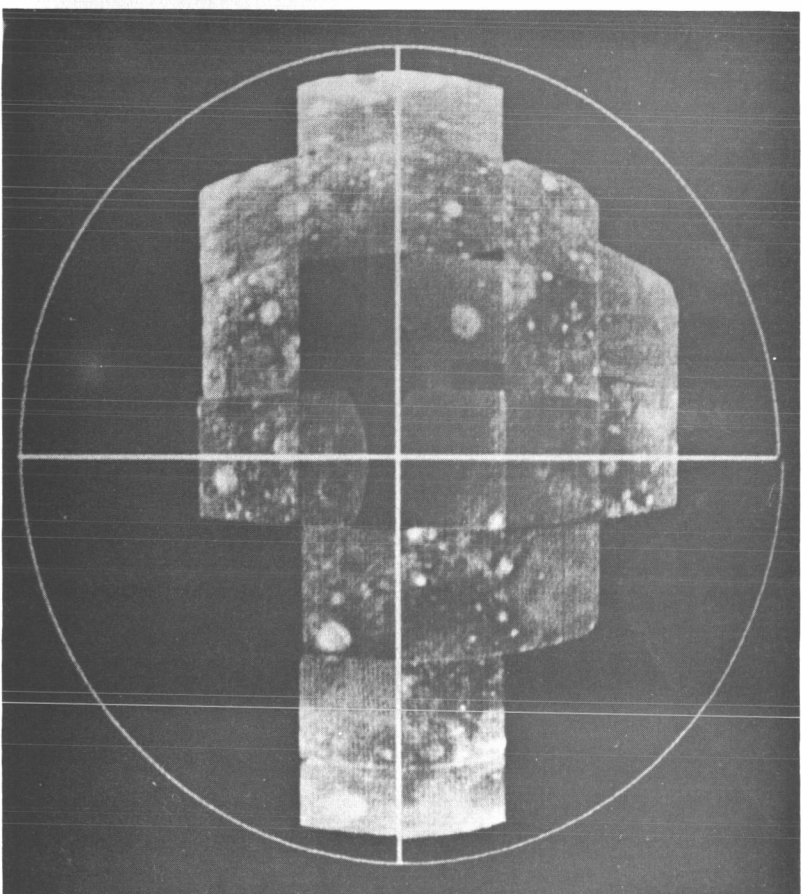
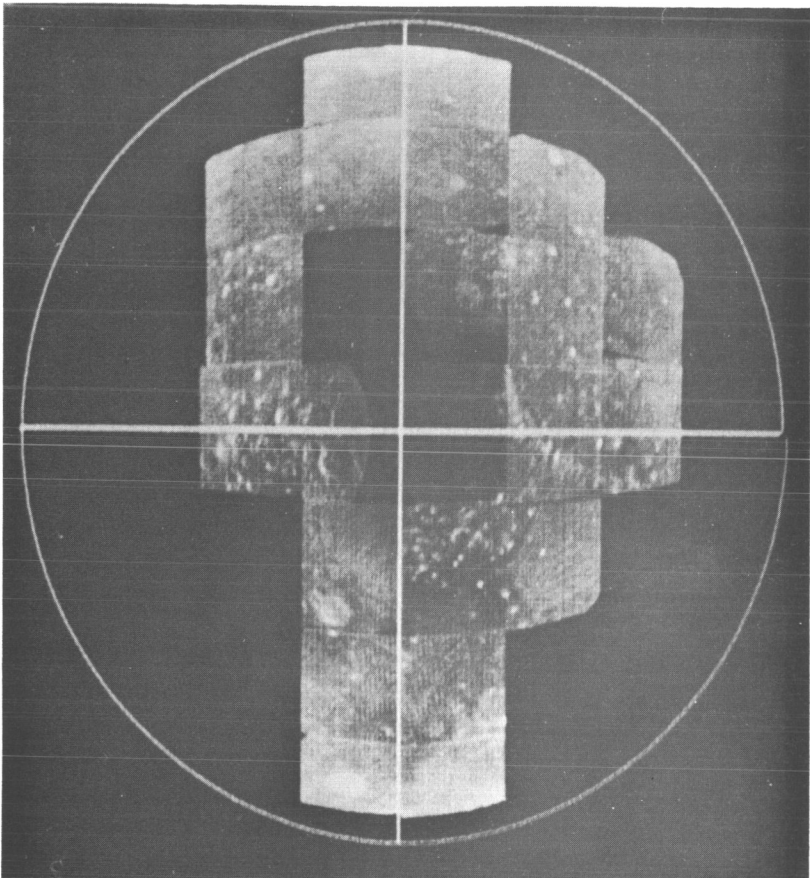
(CODE)

(NASA CR OR TMX OR AD NUMBER)

(CATEGORY)

Final Report

[Supported by NASA Grant No. NGR 33-010-024]



Radar Maps for approximately one-third of the lunar surface as viewed at Mean Libration. Both maps show normalized echoes (including projection effects). Right-hand circular polarization was transmitted. Echoes in the left-hand circular polarization are on the left, and echoes in the right-hand circular polarization are on the right.

CENTER FOR RADIOPHYSICS AND SPACE RESEARCH
CORNELL UNIVERSITY
Ithaca, New York

RESEARCH REPORT RS 73

RADAR STUDIES OF THE LUNAR SURFACE
EMPHASIZING FACTORS RELATED TO
SELECTION OF LANDING SITES

Thomas W. Thompson

Final Report

April 1968

Research conducted under NASA Grant No. NGR 33-010-024 for
1 July 1966 to 31 December 1967.

TABLE OF CONTENTS

	PAGE
FOREWORD	iii
ABSTRACT	iv
I. INTRODUCTION	1
II. DELAY-DOPPLER MAPPING	7
III. DISCUSSION OF THE MAPPING RESULTS	15
IV. SUMMARY AND CONCLUSIONS	23
APPENDIX A. DESCRIPTION OF THE RADAR SYSTEM FOR MAPPING LUNAR ECHOES	24
APPENDIX B. DATA	38
APPENDIX C. MEASUREMENT OF POWER VERSUS DELAY AT 7.5 METERS	42
REFERENCES	46
ACKNOWLEDGMENT	48

FOREWORD

This report is the final report under NASA Grant NGR 33-010-024, "Radar Studies of the Lunar Surface, Emphasizing Factors Related to the Selection of Landing Sites." The measurements were carried out at frequencies of 40 Mhz ($\lambda = 7.5$ m) and 430 Mhz ($\lambda = 70$ cm) at the Arecibo Ionospheric Observatory (AIO).^{*} Sections I through III describe the mapping of radar reflectivity at the wavelength of 70 cm. Appendix A describes the radar system for mapping lunar echoes, and Appendix B presents the data. The measurement of the mean scattering behavior of the moon at the wavelength of 7.5 m is described in Appendix C.

A joint report with Lincoln Laboratory, to be published under separate cover, will compare the results of this project with the lunar radar studies carried out by Lincoln Laboratory under NASA Contract NSR-22-009-106.

*

The Arecibo Ionospheric Observatory is operated by Cornell University with the support of the Advanced Research Projects Agency under a research contract with the Air Force Office of Scientific Research.

ABSTRACT

The radar reflectivity of one-third of the visible lunar surface was mapped at a wavelength of 70 cm using the delay-Doppler technique. The resolution of the radar echo in either time delay or frequency was equivalent to localizing the deflecting areas to strips with widths of 5-10 km. The depolarization of the echo was studied by transmitting a circularly polarized wave and simultaneously receiving opposite circular polarizations.

It was possible to infer differences in roughness of the lunar surface on a meter scale from the depolarization of the radar echo. Both rayed and young craters were found to be rough. Several craters had only rough rims, which may be the result of an aging process that selectively smooths the floor of a crater. The mountains were found to be rougher than the adjacent maria. Differences in roughness within a mare were observed, and in one case, the difference could not be correlated with optical features.

The scattering behavior of the moon, power as a function of delay, was measured at a wavelength of 7.5 m. (See Appendix C.) This agreed with previous measurements at a wavelength of 6 m.

I. INTRODUCTION

The major portion of this study was a mapping of the radar reflectivity of nearly one-third of the visible surface of the moon by the delay-Doppler technique. This technique was proposed by Green¹ as a method for measuring a radar echo from a localized area of the lunar (or planetary) surface, and was successfully applied to lunar radar echoes by Pettengill.² Pettengill and Henry³ discovered strong reflections associated with the rayed crater Tycho. In 1964 at the AIO, Thompson and Dyce^{4,5} resolved the ambiguity inherent in delay-Doppler mapping in a single observation, and several selected regions were mapped. These observations at the AIO were refined and became the basis of the present study.

The results of these earlier mappings can be summarized as follows:

1. The rayed craters had stronger backscattering than their environs.
2. The young, nonrayed craters also had stronger echoes than their environs, with some differences in backscattering being as great as those observed for the rayed craters.
3. The older craters showed no difference in backscattering.
4. A depolarization of the return was found for the few craters which had scattering enhancements that were observed in opposite polarizations.

5. The backscattering from the highlands was consistently stronger than that of the maria, the differences having a two-to-one ratio.

What do these differences in the radar backscattering imply about the characteristics in the lunar surface? Increased roughness (i.e., irregularities with dimensions of the radar wavelength) and slopes tilted toward the radar appear to be responsible for the observed differences in backscattering. The slopes can be studied in great detail optically. However, the roughness of the lunar surface on a meter scale has been observable only for areas near the Surveyor spacecrafts or the areas photographed with the highest resolution by the Orbiter spacecrafts; therefore the detection of rough areas by radar mapping is an extremely valuable adjunct to the Surveyor and Orbiter findings. The radar mappings at meter wavelengths will detect the meter-sized irregularities, that will hinder the safe landing of spacecraft and will be dangerous to lunar vehicles and astronauts.

The major problem in the interpretation of the radar results is distinguishing between backscattering enhancements resulting from rough areas and enhancements resulting from tilting. Fortunately, these mechanisms have different reflection characteristics when observed in opposite polarizations.

The observations of this report, as well as most other radar studies of the moon at meter wavelengths, were made by

transmitting and receiving circular polarizations, so that there was no fading from Faraday rotation in the earth's ionosphere. The polarized echo represents the power in circular polarization opposite to that transmitted. This is the polarization expected for a reflection from a plane, dielectric (or conducting) interface placed perpendicular to the radar's line of sight. The depolarized echo represents the power in the circular polarization that is the same as the transmitted polarization. This polarization is opposite to that of the polarized echo. Transmission in one circular polarization with reception of the opposite circular polarizations does not give all possible combinations of depolarization (it yields only two of the five nonzero terms of the Mueller matrix⁶), but it is sufficient to show a depolarization of the echo by rough areas.

Radar backscattering has shown that the lunar surface is smooth and undulating, but interlaced with rough surfaces that make up a small percentage of the surface. The smooth surface backscatters only where it has facets perpendicular to the radar's line of sight. The rough scatterers are irregularities with linear dimensions on the order of the radar wavelength. These smooth and rough areas of the lunar surface have different reflecting characteristics, as shown in Figure 1. The quasi-specular component (the echo from the smooth areas) is entirely in the polarized echo, and has a sharp decrease in power with increasing angle of incidence.

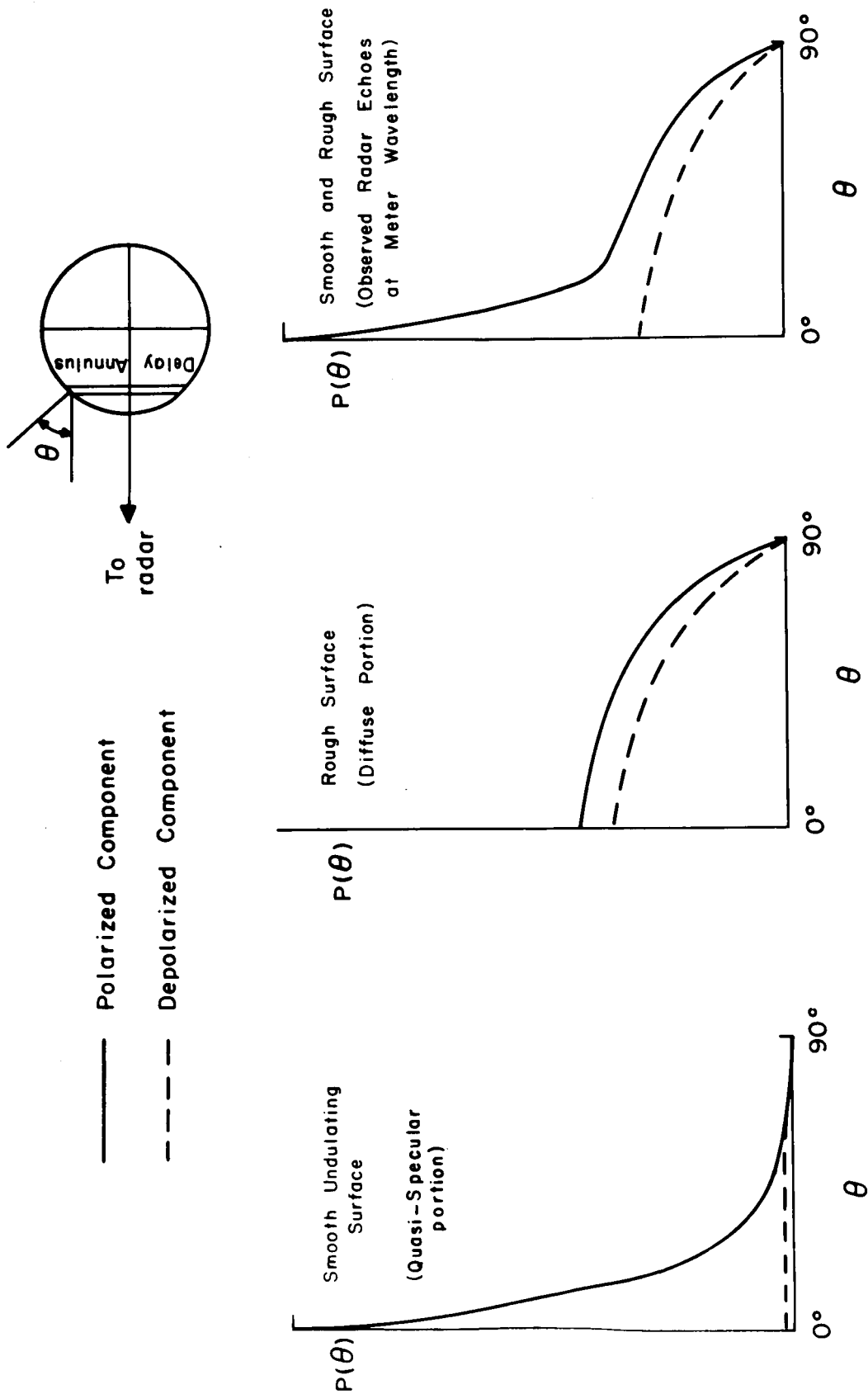


FIGURE 1. Average Radar Backscattering from Lunar Surface as Contributed by Smooth and Rough Surfaces; $P(\theta)$ is the Observed Power at the Angle of Incidence, θ . (The return at a particular angle of incidence can be studied by transmitting very short pulses, so that the echo is confined to a narrow strip, the delay annulus.)

The diffuse component (the echo from the rough scatterers) has comparable power in the polarized and depolarized echo, and a gradual decrease in power with increasing angle of incidence. The mean scattering behavior of the moon is the sum of these two components.

With increasing roughness, the radar echo shows a decrease in the quasi-specular component and an increase in the diffuse component. Except for areas very near the subradar point, this results in an enhancement in the polarized echo and an even larger enhancement in the depolarized echo. Near the subradar point, a rough area shows a decrease in the polarized echo and an increase in the depolarized echo.

Any area, rough or smooth, will exhibit an enhanced echo when tilted toward the radar, as all natural surfaces have backscattering such that the reflected power decreases with increasing angle of incidence. Unless an area is entirely rough, the enhancement in the polarized echo will be greater than the enhancement in the depolarized echo, because of the stronger dependence of the polarized echo upon the angle of incidence.

Equal scattering enhancements in the polarized and depolarized echoes might be expected for an area that has a higher albedo and a roughness equal to its environs; however, none of the radar data suggests this difference in surface properties.

Thus, the rough areas can be distinguished from the slopes by their enhancements. The rough areas give greater enhancements in the depolarized echo (a depolarization of the backscattered power); the slopes give greater enhancements in the polarized return (a specular highlight). These reflections are controlled by the electrical properties of the surface to a depth of a few wavelengths; therefore comparison of radar mappings at different wavelengths should yield information on subsurface conditions.

II. DELAY-DOPPLER MAPPING

Roughness was studied for small areas of the lunar surface by simultaneously resolving the radar echo in time delay and frequency. The geometry of reflecting areas is shown in Figure 2. The annulus D is the area that reflects power at a particular delay; the semiannulus F is the area that reflects power at a particular frequency. The two areas P and P', which are common to both annuli, reflect power at the same delay and frequency. These areas were carefully chosen to have an angular separation such that only area P was illuminated by the mean beam of the antenna. The power at that delay and frequency was therefore positively associated with P. This was possible at the AIO because the antenna beam (at 430 Mhz) was 10', or approximately one-third of the angular width of the moon.

An apparent rotation is imparted to the moon by both the orbital motion of the moon and the motion of the radar about the center of the earth. This apparent rotation is indicated in Figure 2 by an apparent axis of rotation and an apparent equator. The reflecting areas P and P' are equidistant from the apparent equator. The area near the lunar equator was observed only when the apparent and actual axes of rotation were separated by a large angle.



FIGURE 2. Geometry of Radar Echoes from the Lunar Surface.

The lunar coordinates of P were found by transformations between the Cartesian coordinate systems, x_d, y_d, z_d , and ξ, η, ζ shown in Figure 2. The x_d, y_d, z_d coordinate system was radar based. The y_d axis was along the apparent axis of rotation, and z_d axis was along the radar line of sight; thus, z_d was linearly related to delay, and x_d was linearly related to frequency. The lunar coordinates, ξ, η, ζ , formed a second Cartesian coordinate system, where the lunar equator was in the $\xi - \zeta$ plane, and the actual axis of rotation was the η axis. Both coordinate systems were selenocentric and had the lunar radius as a unit length. Thus, a transformation between them involved only rotations, as described in Appendix A.

In order to construct a map, this transformation was performed for many consecutive delays and frequencies. However, the samples of the radar echo included some experimental biases, such as the position of the reflecting area in the antenna beam, background noise, and the size of the reflecting area. Also, the scattering behavior of the moon gave a large variation in echo power with the delay. To help in the identification of subtle differences in the reflecting properties of the lunar surface, these predictable variations were removed by normalizing the radar return, which consisted of taking the ratio between the observed power (after subtraction of noise) and the expected power from homogeneous scattering' (see Appendix A).

Generally, the reflecting areas were not rectangular, therefore a measure of the size of the reflecting area was taken to be the widths of the delay and frequency annuli as measured along the lunar surface. The width of the delay annulus when projected onto the radar line of sight was $c\tau/2$, where c is the velocity of light, and τ is the transmitter pulse length. The width of the frequency annulus when viewed from the earth was $b\Delta f/F_{cl}$, where b is the lunar radius, Δf is the filter bandwidth, and F_{cl} is the difference in frequency between the leading edge and the limb. These widths increased when measured along the lunar surface. The frequency bandwidth was 0.02 hz, so that up to 70 spectra were obtained in an observation of 40 min. This resulted in a frequency resolution of 5-10 km, as shown in Figure 3b. Equivalent range resolutions of 3 - 7 km could be obtained by the use of a transmitter pulse length of 20 μ s, as shown in Figure 3a.

Radar echoes were mapped if they had reflecting areas in the main beam of the antenna, and conjugate reflecting areas in the antenna side lobes. Only 100 delay and 140 frequency samples were permitted by the data-storage capability of the computer programs for data taking and analysis. In some cases, the range resolution was slightly degraded to ensure that an area of interest was within coverage of the number of delay samples permitted.

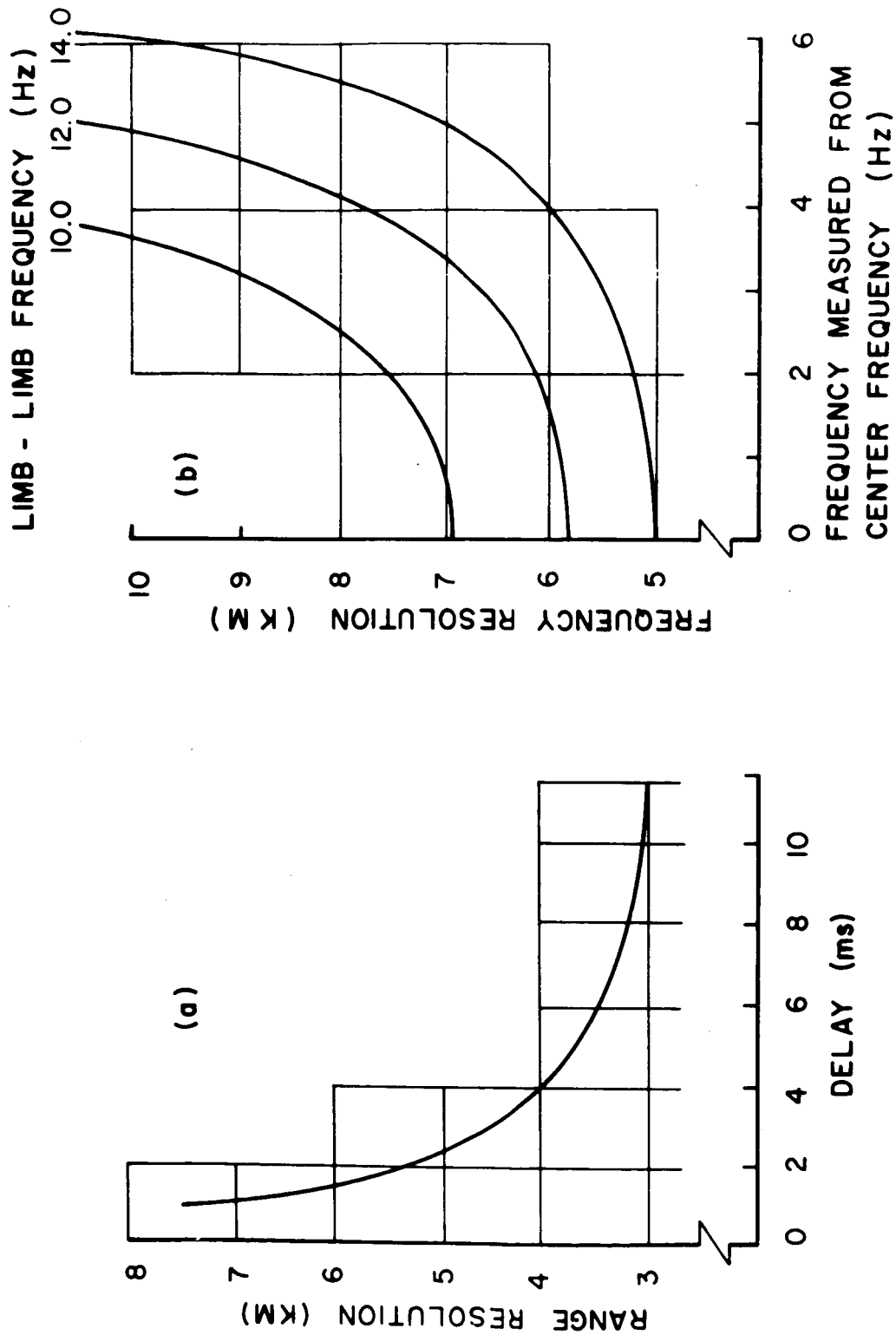


FIGURE 3. (a) Range Resolution for Transmitter Pulse Length of 20 μ s Plotted Versus Delay from the Leading Edge; (b) Frequency Resolution for Bandwidth of 0.02 Hz and for Typical Limb-Limb Frequencies.

The objective of this program was to map the areas shown in Series 1 and 2 of the LAC charts.⁷ These charts show the area near the lunar equator, where the first astronauts are to land. Beyond the equatorial regions, the radar mapping was of areas shown on the charts LAC 24, LAC 25, and the maps B3a Taurus, C2a Caucasus, C7a Maurolycus, D2a Plato, and D7a Tycho of the Orthographic Lunar Atlas.⁸ The area of chart LAC 76 was not successfully observed under favorable libration conditions. The total mapped area covers one-third of the visible lunar surface. (See Figure 4.)

Four areas were mapped with a twofold improvement in the delay and frequency resolutions. These areas were centered on the rayed craters Tycho and Copernicus, and the Lunar Orbiter Sites II-P-2* and II-P-6.**

Ratio maps were generated to distinguish between backscattering differences caused by rough surfaces and slopes. These show the ratio of the normalized depolarized echo to the normalized polarized echo. Higher values in these maps (the bright areas in the intensity-modulated plots) showed a depolarization of the echo, an indication of a rougher surface; lower returns show the specular highlights, an indication of slopes.

* Lunar Orbiter Site II-P-2 is the area near longitude $34^{\circ}00'$ East and latitude $2^{\circ}40'$ North.

** Lunar Orbiter Site II-P-6 is the area near longitude $23^{\circ}27'$ East and latitude $0^{\circ}45'$ North.

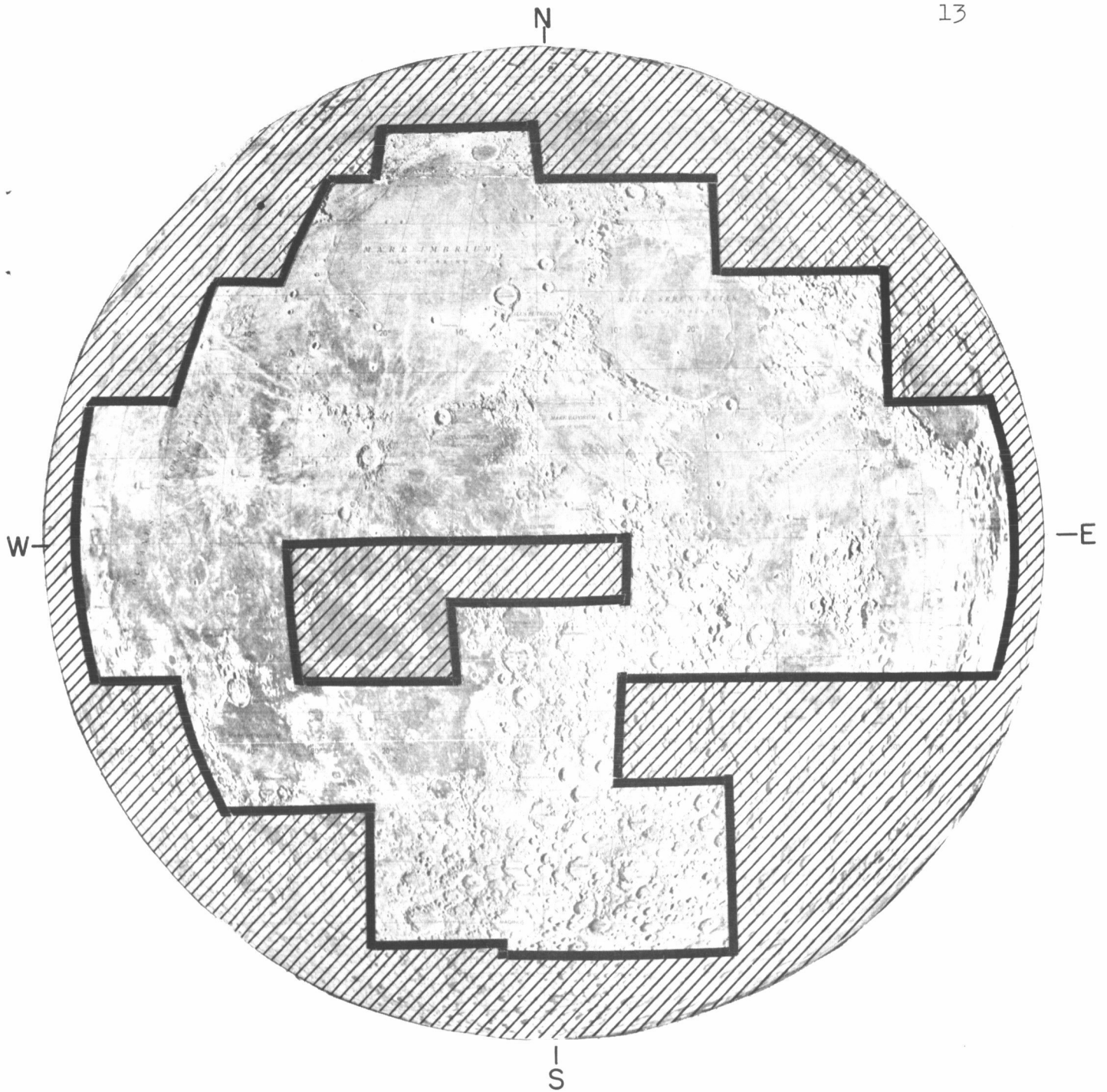


FIGURE 4. Area of the Moon Mapped with the 430 Mhz Radar at the AIO. (Background Map is USAF Reference Mosaic.⁷)

The 10,000 values of normalized reflectivity for each map are presented in two ways. The magnitudes of the back-scattering differences are best shown in isometric plots; whereas the positions of scattering differences are indicated in the intensity-modulation plots, where the brightness is proportional to the normalized radar reflectivity. The displacements along the abscissa and the ordinate are proportional to lunar coordinates. All maps are presented in the data section (Appendix B).*

A few differences in reflected power appeared to be associated with observational errors. The uniform difference in power across the radar map of LAC 75 Letronne (Plate XV) probably resulted from an error in antenna tracking. A smearing of the echo along contours of constant delay appears in the radar maps of LAC 42 Mare Serenitatis (Plate VI) and LAC 93 Mare Humorum (Plate XX). This probably resulted from an incorrect compensation for changes in the Doppler frequency. Two areas showed a depolarized enhancement but no polarized enhancements, probably caused by a leakage of a high polarized return from the conjugate reflecting areas into the depolarized return. The crater Tycho could have caused the high returns seen in the radar map of LAC 40 Timocharis (Plate IV). Similar high returns appear in the radar map of LAC 94 Pitatus (Plate XXI). Nearly identical results were obtained for independent observations of three areas, as shown in the Plates XXXII through XXXIV of the data section (Appendix B).

* A compilation of the radar maps for the LAC charts as projected onto the ξ - η coordinates is shown in the frontispiece.

III. DISCUSSION OF THE MAPPING RESULTS

The optimum terrain for spacecraft landing sites is a smooth area. In the radar maps such an area would appear as an area of low returns; however, no area of very low returns was found. From the ubiquity of the depolarized return, one can infer that the roughness that gives the diffuse component of radar scattering is common to all areas of the moon.

Enhancements in backscattering appeared to be associated with:

1. Craters
2. Isolated mountain peaks and ridges in the maria
3. Highland-mare differences
4. Intramare differences.

1. Craters

The brightest features in the radar maps are the large rayed craters listed in Table 1. Each of these was identified as a very rough area, since it showed a large enhancement in the depolarized return and a somewhat weaker enhancement in the polarized return. These enhancements were confined to the crater and its rim. Differences in backscattering associated with the rays were not apparent except, possibly, for the crater Tycho.

TABLE 1
Rayed Craters Resolved by the Radar

Crater	Plate	Map	
Aristarchus	Plate III	LAC 39	Aristarchus
Aristillus	Plate II Plate XXVI	LAC 25 D2a	Cassini Plato
Bullialdus	Plate XXI	LAC 94	Pitatus
Copernicus	Plate IX Plate XXX	LAC 58 Crater	Copernicus Copernicus
Kepler	Plate VIII	LAC 57	Kepler
Langrenus	Plate XIX	LAC 80	Langrenus
Theophilus	Plate XVII Plate XXIX	LAC 78 Lunar Orbiter	Theophilus II-P-6
Tycho	Plate XXVII Plate XXXI	D7a Crater	Tycho Tycho

Several nonrayed craters were observed to be rough areas, though smaller enhancements were observed for these craters in comparison to the rayed craters. Specular enhancements were often observed, where inner rims of the crater were tilted toward the radar. The outer rims of the craters showed smaller specular enhancements, an expected result, since the inner rims are steeper than the outer rims.

Many craters showed backscattering enhancements, but were not resolved. Several of these showed nearly equal enhancements in the opposite polarizations, which probably resulted from the specular enhancements of the crater rims equaling the enhancements resulting from greater roughness. None of the craters that were resolved showed equal enhancements in the opposite polarizations, an indication of a higher albedo. Many craters did not show enhancements, as expected from previous studies.^{4,5} Several older craters had enhancements at their rims while their floors had moderate or no enhancements. These are listed in Table 2.

The roughness and age of the crater appear to be correlated. The rayed craters, the youngest, were the roughest. The young, nonrayed craters were also rough. Somewhat older craters had rough rims, but smooth floors. The oldest had smooth rims and floors, and showed only specular highlights where their rims were favorably tilted toward the radar.

TABLE 2
Craters with Rough Rims and Smooth Floors

Crater	Plate		Map
Archimedes	Plate V	LAC 41	Montes Apenninus, and
	Plate XXVI	D2a	Plato
Pitatus	Plate XXI	LAC 94	Pitatus
Plato	Plate XXVI	D2a	Plato
Posidonius	Plate XXIII	B3a	Taurus
Taruntius	Plate XII	LAC 61	Taruntius

2. Isolated Mountain Peaks and Ridges

In addition to the craters, several mountain peaks and ridges in the maria showed enhanced backscattering. These appeared to be rough, since they gave a depolarization of the echo. Table 3 lists examples of this type of feature.

TABLE 3
Isolated Mountain Peaks and Ridges
Showing Enhancements

Feature	Plate	Map	
<u>Mountain Peaks</u>			
La Hire	Plate IV	LAC 40	Timocharis
Pico	Plate II, Plate XXVII	LAC 25 D2a	Cassini and Plato
Pico β	Plate II, Plate XXVII	LAC 25 D2a	Cassini and Plato
Piton	Plate II, Plate XXVII	LAC 25 D2a	Cassini and Plato
<u>Ridges</u>			
Flamsteed Ring	Plate XV	LAC 75	Letronne
Montes Recti	Plate XXVI	D2a	Plato
Montes Spitzbergensis	Plate II, Plate XXVI	LAC 25 D2a	Cassini and Plato
Montes Teneriffe	Plate II, Plate XXVI	LAC 25 D2a	Cassini and Plato

3. Highland-Mare Differences

A systematic difference in roughness was observed between the mountains and the adjacent maria. Although this effect had been observed in previous studies,^{4,5} the observations in opposite polarizations showed that this difference resulted from the highlands being rougher than the adjacent mare regions. Examples of this type of difference are given in Table 4.

4. Intramare Differences

A surprising result of the radar mapping was the discovery of differences in roughness within a mare. The eastern and southern "shore" of Mare Serenitatis (see Plate VI) was smoother than adjacent areas in the same mare. This shore is dark in full-moon photographs. The Montes Harbinger, a number of hills near the crater Aristarchus in Oceanus Procellarum, were slightly rougher than the surrounding mare (see Plate III).

The largest difference in scattering from within a mare was observed in Mare Imbrium, between the craters Aristillus and Plato (see Plates II, XXVI, and XXXII). This was even more surprising, since this area is not differentiated when viewed optically.

TABLE 4
Examples of Mountain-Mare Differences

Mountain-Mare	Plate	Map
Montes Jura surrounding Sinus Iridum	Plate I	LAC 24 Sinus Iridum
Palus Somnii and to Mare Tranquillitatis	Plate XII	LAC 61 Taruntius
Highlands between Mare Crisium and Mare Fecunditatis	Plate XIII	LAC 62 Mare Undarum
Highland surrounding Grimaldi on eastern shore of Oceanus Procellarum	Plate XIV	LAC 74 Grimaldi
Montes Pyrenaei between Mare Fecunditatis and Mare Nectaris	Plate XVIII	LAC 79 Colombo
Montes Taurus between Mare Serenitatis and Mare Tranquillitatis	Plate XXIII	B3a Taurus
Montes Caucasus between Mare Serenitatis and Mare Imbrium	Plate XXIV	C2a Caucasus
Montes Alpes on northeastern shore of Mare Imbrium	Plate XXVI	D2a Plato
Montes Pyrenaei and Mare Tranquillitatis	Plate XXVIII	Lunar Orbiter II-P-2

Such differences were not observed in highland areas. This may be a selection effect, however, since two maps include only highland areas, while ten maps have only maria. Furthermore, a general trend may be very difficult to detect among the specular highlights caused by the multitude of slopes in a highland area.

IV. SUMMARY AND CONCLUSIONS

In conclusion, the mapping of lunar radar echoes at 70 cm showed (1) that differences in roughness existed within a mare, (2) that mountains were rougher than the adjacent mare regions, and (3) that several older craters had rough rims. The differences in scattering known to exist for young and rayed craters were studied with finer resolution and appeared to result from increased roughness. The ubiquity of the depolarized return indicates that roughness on the meter scale is common to all areas of the moon.

The moon was also observed at 7.5 m (see Appendix C for details). Only the variation of the power in the polarized echo with delay was measured, and was found to agree with measurements at 6 m reported by Klemperer.⁹

APPENDIX A. DESCRIPTION OF RADAR SYSTEM FOR MAPPING LUNAR RADAR ECHOES

The mapping of lunar radar reflectivity at the AIO was accomplished by the radar system and off-line processing shown in Figure A.1. There were three steps in the data processing,

1. Phase-quadrature samples of the radar echo were taken for many consecutive delays at a spacing equal to the transmitter pulse width and for many consecutive transmitter pulses.

2. The spectrum at a particular delay was obtained from a Fourier analysis of the phase-quadrature samples of step 1. At the end of this step, the radar echo can be considered as a matrix of power with delay aligned in rows and frequency aligned in columns.

3. The scattering efficiencies (normalized powers) for selenographic positions were computed from the matrix of observed power of step 2. This was performed in two steps, where the normalized power was first computed and then transformed into lunar coordinates.

1. Recording the Radar Echo

The first objective of the radar system was to establish the radar echo on a narrow strip of the lunar surface (the delay annulus of Figure 2, Section II) by transmitting and

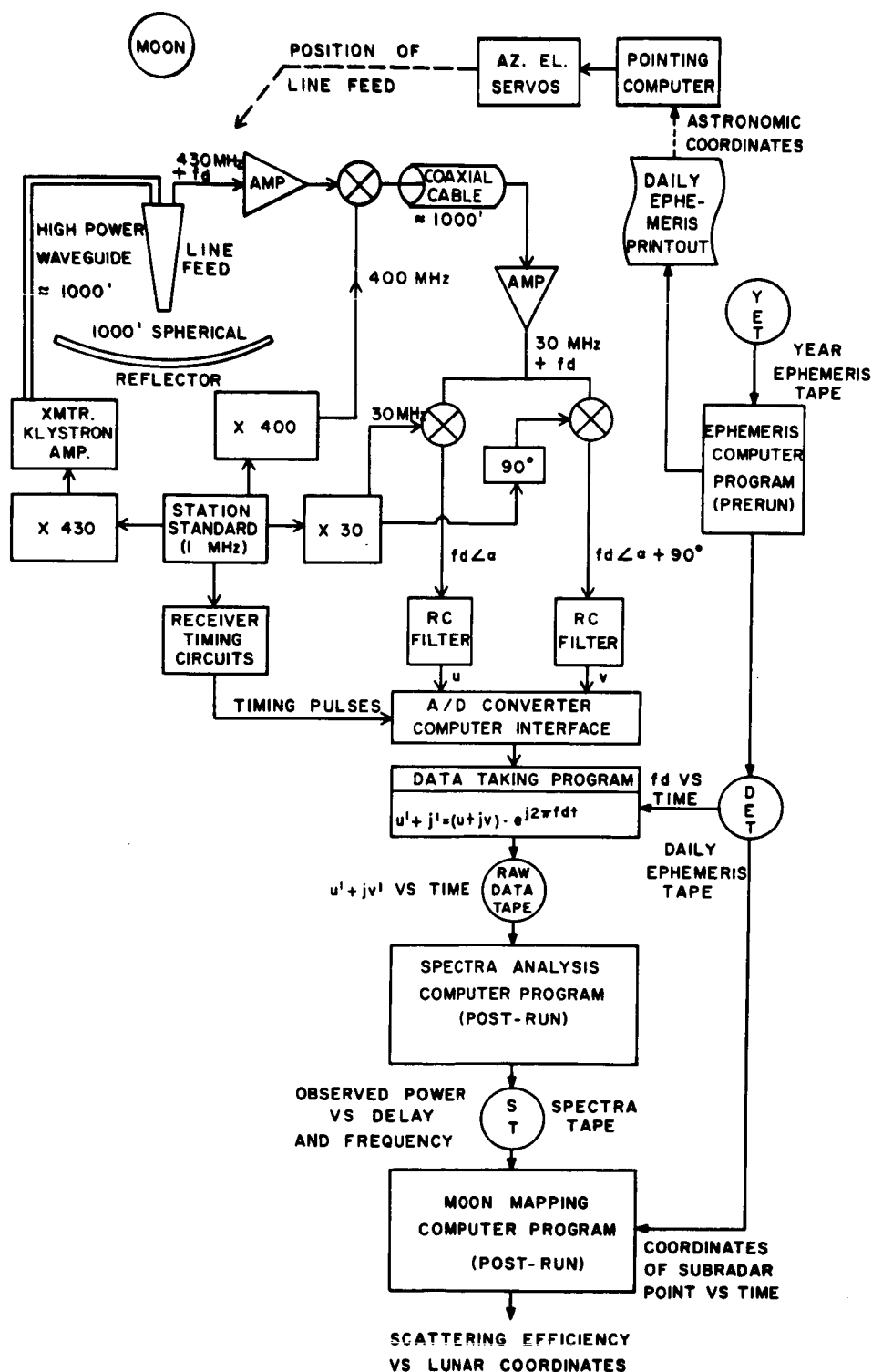


FIGURE A.1. Diagram of the Radar System and Computer Processing used in the Mapping of Lunar Radar Reflectivity.

receiving short pulses. A coherent system was used, so that subsequent frequency analysis established the radar echo on a second narrow strip of the lunar surface (the frequency annulus of Figure 2, Section II).

The coherent transmission and reception of short pulses was provided by the radar system shown in Figure A.1. The short pulses were generated at the transmitter and carried to the line feed by a high-power waveguide. After transmission from the line feed, the energy in the short pulses was reflected by the 1000 ft. diameter reflector and collimated in a beam of angular width of $10'$ of arc. The direction of the beam in space was controlled by the position of the line feed over the reflector as directed by the outputs of a small digital computer. The inputs to this computer were the coordinates of right ascension and declination for a lunar position as provided by a precomputed ephemeris.

The reflection from the lunar surface was collected by the reflector and line feed, amplified, heterodyned to 30 Mhz, and fed to the receiving equipment through a coaxial cable. (This coaxial cable was very long because of the long distances from the line feed to the bulk of the receiving equipment.) The return signal was amplified and split into two equal parts. Each part was heterodyned with a 30 Mhz signal and passed through RC filters. These filters, which had a time constant of one-third the transmitter pulse width,

approximated a matched filter. The frequency of these signals was equal to the Doppler frequency created by the motion of the lunar surface with respect to the radar. There was a spread in frequencies, since different parts of the lunar surface had different velocities along the radar line of sight. The RC filter outputs represented the real and imaginary parts of the echo phasor, since one of the 30 Mhz signals was delayed by 90° .

The last step in the data recording was to perform a complex multiplication of the observed phasor with the phasor, $e^{j2\pi f_d t}$, where f_d is the Doppler frequency of a specified lunar position, and t is time. This multiplication simulated a beating of the signal to zero frequency, so that the post-run Fourier analysis could be performed quickly by the Cooley-Tukey algorithm.* A listing of the Doppler frequencies was provided by daily ephemeris tape produced by the ephemeris program.

The transmission frequency of 430 Mhz and the heterodyning frequencies of 400 Mhz and 30 Mhz had to be accurate to 0.01 hz in order to carry out the subsequent Fourier analysis. This was accomplished by generating these frequencies from the station standard, a local oscillator running at a frequency of 1 Mhz with an accuracy of one part in 10^{11} .

* The coding for this algorithm was provided by Norman Brenner of the computing staff of the Haystack radar site of the Lincoln Laboratory, M.I.T.

2. Spectral Analysis

After the samples of the radar echo were stored for many consecutive transmitter pulses, the spectral analysis was performed. Here, the phasors for a given range box were correlated with unit vectors rotating at a given set of frequencies. This correlation was carried out for a number of pulses, which in real time was equal to the reciprocal of the frequency resolution. Thus, the phasors were correlated for 50 seconds of real time (512 pulses) in order to realize a frequency resolution of $1/50$ hz. These spectral outputs were stored for each correlation, to be used subsequently as inputs to the mapping program.

The spectral analysis was carried out using the Cooley-Tukey algorithm, which for this application was five times faster than the usual spectral analysis.

3. Mapping Program

After the spectral analysis was completed, the third and final step of the mapping was performed. Here, an array of normalized power versus lunar positions was derived from the spectral output of power versus delay and frequency. This was accomplished in two steps, in which the echo was first normalized and then mapped onto lunar coordinates.

Both the normalization and the mapping were facilitated by the radar coordinate system x_d , y_d , z_d described in

Section II. This coordinate system was selenocentric: the z_d axis was directed toward the radar; the apparent axis of rotation was in the $y_d - z_d$ plane; and the surface of the moon was assumed to be a unit sphere. The relations between x_d , y_d , z_d , delay and Doppler frequency for the parallel-ray case were:

$$\begin{aligned} x_d &= 1 - \frac{d}{D_o} \\ y_d &= \pm \left[1 - x_d^2 - z_d^2 \right]^{1/2} \\ z_d &= \frac{f_o - f}{F_{c\ell}} \end{aligned} \quad (A.1)$$

where

- d = round-trip delay from the leading edge of the moon,
- D_o = round-trip delay from the leading edge to the limb of the moon,
- f_o = Doppler frequency of the leading edge of the moon,
- f = Doppler frequency of the point of interest,
- $F_{c\ell}$ = difference in Doppler frequency from the leading edge to the limb.

The ambiguity inherent in delay-Doppler mapping occurs in the choice of the sign of y_d . At the AIO, the sign was determined from knowledge of the direction of the antenna beam. An imaginary root in y_d indicated that the delay and Doppler frequency used to determine x_d and z_d were not possible for a reflection from the lunar surface.

a. Normalization of Echo

The normalization of the radar echo, the first task of the mapping program, removed the predictable variations in reflected power resulting from:

1. the position of the scattering area in the antenna beam,
2. the variation in scattering area with different delays and frequency, and
3. the decrease in reflected power with increasing delay.

The antenna beam was assumed to be Gaussian, so each radar return in the delay-frequency matrix was multiplied by $\exp [\alpha R^2]$. The term R was the angular distance between the point of interest and the center of the beam, as given by

$$R = S \left[(x_d - x_{db})^2 + (y_d - y_{db})^2 \right]^{1/2} \quad (\text{A.2})$$

where

- x_d, y_d = the radar coordinates of the point of interest,
 x_{db}, y_{db} = the radar coordinates of the center of the
 main beam, and
 S = the semidiameter of the moon.

The term α was chosen so that this multiplying factor was 0.25 at the half-power beamwidth of 5.0' of arc. Reflecting areas were not mapped if they were outside the main beam or if the conjugate area (the area with radar coordinates $x_d, -y_d, z_d$) was in the main beam of the antenna.

The size of the scattering area was assumed to be inversely proportional to the radar coordinate y_d .⁵ The variation of the echo with delay was given by the mean scattering law, which gave the power for a given angle of incidence θ . For the assumption that the moon was spherical, the angle of incidence was related to the radar coordinate z_d and delay by

$$\cos(\theta) = z_d = 1 - \frac{d}{D_0} \quad . \quad (A.3)$$

This formulation neglected local differences in angle of incidence caused by slopes. The mean scattering law of the polarized echo was an empirical fit to the measurements reported by Hagfors,⁶ which were performed at a wavelength of 68 cm using transmitter pulses of 12 μ s duration. The mean scattering law for the depolarized echo was assumed to have a Euler law dependence, $P(\theta) \propto \cos \theta$. This dependence is strongly suggested by the measurements reported by Evans and Pettengill,¹⁰ which were also performed at a wavelength of 68 cm, but with a transmitter pulse of 200 μ s.

The normalized radar echo $P_n(d,f)$, at a particular delay and Doppler frequency d,f was then,

$$P_n(d,f) = \text{constant} \left[\frac{y_d \exp(\alpha R^2)}{P(\theta)} \right] (P_o(d,f) - N) \quad (A.4)$$

where

$P(\theta)$ = the mean scattering law,

$P_o(d,f)$ = the observed power, and

N = the estimate of the noise.

The constant of Equation (A.4) was chosen so that the average normalized echo was near 100. This normalization was performed before mapping the return into lunar coordinates, since each normalization was directly related to delay and frequency.

b. Mapping into Lunar Coordinates

The second task of the mapping program was to transform the matrix of normalized power in delay and frequency into a matrix of normalized power versus lunar positions. The lunar coordinates of interest were either the longitude-latitude (λ , β) coordinates or the direction cosines ξ , η , ζ . These are related by,

$$\xi = \cos(\beta) \sin(\lambda)$$

$$\eta = \sin(\beta)$$

$$\zeta = \cos(\beta) \cos(\lambda)$$

$$\beta = \arctan \left[\eta / (\xi^2 + \zeta^2)^{1/2} \right]$$

$$\lambda = \arctan(\xi / \zeta).$$

For the parallel-ray case, the transformation into lunar coordinates from the radar coordinates required only

a rotation about the center of the moon. This transformation was not accurate because of parallax effects. For the mapped area, however, the variation in differences between the exact and parallel-ray determination of delay and frequency was considerably less than the resolution of the mapping. If the delay sampling and spectral analysis were taken so that a given lunar position near the center of the mapped area was at a particular delay and frequency, the delay and frequency of any other lunar position in the mapped area could be computed using the parallel-ray equations.

Another problem was that the transformation between the two coordinates systems changed significantly in an hour, the time needed to reduce the statistical fluctuations of radar returns. Thus, it was impossible to find one transformation that would correctly map the data for one hour, and the alternative approach of mapping every spectrum would have been too time consuming. A compromise between these two extremes was used. The spectra were summed until one of the end points of the map had deviated in delay or frequency by the resolution of the measurement. These summed spectra were then normalized and mapped onto lunar coordinates. This was repeated until all the spectra were mapped. Generally, 5-10 spectra were summed for a particular transformation, and up to 50 spectra were summed for the entire map.

The mapping of delay and frequency given in terms of the radar coordinates x_d, y_d, z_d into the lunar coordinates ξ, η, ζ

was a rotation about the center of the moon. The amount of rotation was computed from the longitude and latitude of the subradar point, ℓ' , b' , and their rates of change. It was convenient to use a third angle, da , the angle between the apparent and actual axes of rotation as viewed by the radar given in an earlier study⁵:

$$da = \arctan \left[\frac{-\frac{db'}{dt}}{\cos(b') \frac{d\ell'}{dt}} \right] . \quad (A.6)$$

The transformation of interest was from lunar coordinates into radar coordinates, so that the delay and Doppler frequency of a particular selenographic position could be computed. This transformation was:

$$\begin{aligned} x_d &= a_{11} \xi + a_{12} \eta + a_{13} \zeta \\ y_d &= a_{21} \xi + a_{22} \eta + a_{23} \zeta \\ z_d &= a_{31} \xi + a_{32} \eta + a_{33} \zeta \end{aligned} \quad (A.7)$$

where

$$a_{11} = \cos(da) \cos(\ell') + \sin(da) \sin(b') \sin(\ell')$$

$$a_{12} = -\sin(da) \cos(b')$$

$$a_{13} = -\cos(da) \sin(\ell') + \sin(da) \sin(b') \cos(\ell')$$

$$a_{21} = \sin (da) \cos (\ell') - \cos (da) \sin (b') \sin (\ell')$$

$$a_{22} = \cos (da) \cos (b')$$

$$a_{23} = -\sin (da) \sin (\ell') - \cos (da) \sin (b') \cos (\ell')$$

$$a_{31} = \cos (b') \sin (\ell')$$

$$a_{32} = \sin (b')$$

$$a_{33} = \cos (b') \cos (\ell') . \quad (A.8)$$

During the radar observation, a specific lunar position, ξ_s, η_s, ζ_s was made to fall at a delay box, id_s , and particular frequency box, if_s . The delay and frequency box, (id, if) , of any other lunar position was therefore:

$$id = id_s - \frac{\Delta z_d}{\Delta d} D_o = id_s - \frac{D_o}{\Delta d} (a_{31} \Delta \xi + a_{32} \Delta \eta + a_{33} \Delta \zeta)$$

$$if = if_s - \frac{\Delta x_d}{\Delta f} F_{cl} = if_s - \frac{F_{cl}}{\Delta f} (a_{11} \Delta \xi + a_{12} \Delta \eta + a_{13} \Delta \zeta)$$

(A.9)

where

$$\Delta \xi = \xi - \xi_s$$

$$\Delta \eta = \eta - \eta_s$$

$$\Delta \zeta = \zeta - \zeta_s$$

Δd = separation in time delay between samples

Δf = separation in frequency between samples.

The power at a particular delay and frequency was a complicated average of the power reflected for an area on the lunar surface, the size of which was determined by the transmitter pulse length and the frequency bandwidth of spectral analysis. The spacing of the samples was such that these areas were adjacent and covered some area of interest. In the same way, the echoes were mapped onto a grid of lunar positions, where each grid point had an area associated with it. These areas were roughly equal to the area associated with a delay-frequency sample. The normalized power for a given lunar position was:

$$P_{ij} = \frac{1}{A_{ij}} \sum_{m,n} A(m,n) P(m,n) \quad (A.10)$$

where

P_{ij} = normalized power of the i^{th} , j^{th} lunar grid point,

A_{ij} = area associated with the i^{th} , j^{th} lunar grid point,

$P(m,n)$ = power associated with the m^{th} , n^{th} delay-frequency grid point,

$A(m,n)$ = common area between the A_{ij} and the area associated with the delay-frequency grid point.

An approximation to this summation was performed in the mapping program. The lunar cell was divided into $N \times N$ subcells, and

the power for each subcell was taken to be the power of the nearest delay-frequency point. The power of a lunar grid point was the average of the powers from all subcells. For this approximation to be valid, the area associated with the lunar position had to be equal to or larger than the area associated with the delay-frequency grid.

4. Summary

The mapping program produced a measure of the reflecting properties for the area surrounding each point of a set of grid points in lunar coordinates. The spacing of grid points approximately matched the resolution in time delay and frequency provided by the radar system and subsequent Fourier analysis. Normalization of the radar echo in the mapping program removed experimental variations that would mask subtle differences in the reflectivity of the lunar surface.

APPENDIX B. DATA

The maps of the radar reflectivity for approximately one-third of the visible lunar surface are presented here. Maps correspond to either a LAC chart⁷ or a map from the Orthographic Lunar Atlas,⁸ as listed in Table 5.

Independent mappings of three areas and four mappings at a finer resolution are also presented. The range resolution, frequency resolution, and dates of observations are given in Table 6.

The intensity-modulation plots are labelled in capital Roman numerals as Plates I through XXXIV, and the isometric plots are labelled in lower-case Roman numerals as Plates i through xxxiv. In the isometric plots, the tick marks on the ordinate are separated by the mean normalized power, with every fifth tick mark accented. The tick marks on the abscissa are separated by either two degrees of longitude or every 0.050 in ξ , depending upon the coordinates of the map. In the intensity-modulation plots, the abscissa is longitude or direction-cosine ξ , the ordinate is latitude or direction-cosine η ; the intensity is proportional to the normalized radar return. The grid lines in the intensity-modulated plots do not necessarily correspond to integer values of degrees in latitude or longitude.

TABLE 5

List of Radar Maps

Plate No.	Chart No.	Title	Plate No.	Chart No.	Title
<u>LAC Charts</u>					
I	LAC 24	Sinus Iridum	XXI	LAC 94	Pitatus
II	LAC 25	Cassini	XXII	LAC 95	Purbach
III	LAC 39	Aristarchus	<u>Maps from Orthographic Lunar Atlas</u>		
IV	LAC 40	Timocharis	XXIII	B3a	Taurus
V	LAC 41	Montes Apenninus	XXIV	C2a	Caucasus
VI	LAC 42	Mare Serenitatis	XXV	C7a	Maurolycus
VII	LAC 56	Hevelius	XXVI	D2a	Plato
VIII	LAC 57	Kepler	XXVII	D7a	Tycho
IX	LAC 58	Copernicus	<u>Maps with Finer Resolution</u>		
X	LAC 59	Mare Vaporum	XXVIII	Enviorns of Lunar Orbiter Site II-P-2	
XI,	LAC 60	Julius Caesar	XXIX*	Enviorns of Lunar Orbiter Site II-P-6, and Crater Theophilus	
XII	LAC 61	Taruntius	XXX	Crater Copernicus and its enviorns	
XIII	LAC 62	Mare Undarum	XXXI	Crater Tycho and its enviorns	
XIV	LAC 74	Grimaldi	<u>Independent Mappings of the Same Area</u>		
XV	LAC 75	Letronne	XXXII	LAC 25	Cassini
XVI	LAC 77	Ptolemaeus	XXXIII	LAC 56	Hevelius
XVII	LAC 78	Theophilus	XXXIV	LAC 80	Langrenus
XVIII	LAC 79	Colombo			
XIX	LAC 80	Langrenus			
XX	LAC 93	Mare Humorum			

* This map is given only as intensity-modulation plots of the normalized polarized and depolarized returns.

Table 6
Observational Data for Moon Radar Maps

Plate	Title	Range Resolution (km)	Frequency Resolution (km)	Date Observed
I	LAC 24	7.9	7.6	17 April 1967 23:37 - 24:10
II	LAC 25	8.2	6.5	17 April 1967 22:43 - 23:22
III	LAC 39	6.6	5.9	1 Nov. 1966 06:05 - 06:45
IV	LAC 40	7.9	5.9	1 Nov. 1966 07:17 - 07:44
V	LAC 41	10.5	5.1	15 Mar. 1967 20:14 - 20:42
VI	LAC 42	7.2	7.0	3 Nov. 1966 07:36 - 08:10
VII	LAC 56	4.5	8.2	19 Feb. 1967 00:10 - 00:48
VIII	LAC 57	7.8	5.8	17 Feb. 1967 23:36 - 24:00
IX	LAC 58	8.8	5.1	12 Mar. 1967 17:50 - 18:22
X	LAC 59	8.1	6.1	26 Oct. 1967 09:12 - 09:50
XI	LAC 60	10.3	7.3	20 Apr. 1967 01:22 - 02:04
XII	LAC 61	8.3	7.3	13 June 1967 21:53 - 22:33
XIII	LAC 62	6.6	8.6	13 June 1967 20:30 - 21:10
XIV	LAC 74	6.5	9.5	19 Apr. 1967 23:40 - 24:19
XV	LAC 75	7.1	7.0	06 Dec. 1966 11:39 - 12:12
XVI	LAC 77	8.5	4.9	20 Sept. 1967 04:39 - 05:10
XVII	LAC 78	9.9	5.6	17 Feb. 1967 22:16 - 22:56
XVIII	LAC 79	6.3	6.1	15 Mar. 1967 19:06 - 19:46
XIX	LAC 80	4.9	11.2	18 Feb. 1967 23:11 - 23:47
XX	LAC 93	7.4	7.8	04 Nov. 1966 08:18 - 08:57

Table 6 (Cont'd.)

Plate	Title	Range Resolution (km)	Frequency Resolution (km)	Date Observed	
XXI	LAC 94	8.6	6.6	22 Apr.	1967 01:38 - 02:18
XXII	LAC 95	6.5	5.0	02 June	1967 08:27 - 08:55
XXIII	B3a	6.1	7.4	06 Nov.	1966 11:55 - 12:30
XXIV	C2a	6.0	6.7	03 Nov.	1966 08:41 - 09:20
XXV	C7a	7.2	7.3	04 Nov.	1966 09:36 - 10:16
XXVI	D2a	8.0	6.8	17 Apr.	1967 23:37 - 24:10
XXVII	D7a	10.2	6.5	17 Apr.	1967 21:38 - 22:17
XXVIII	Orbiter	2.3	3.9	27 Sept.	1967 10:58 - 11:55
XXIX	Theophilus	3.7	2.8	21 Sept.	1967 06:16 - 07:15
XXX	Copernicus	4.0	2.7	21 Sept.	1967 05:00 - 06:00
XXXI	Tycho	2.6	3.2	26 Sept.	1967 10:03 - 11:00
XXXII	LAC 25a	8.2	6.5	17 Apr.	1967 22:43 - 23:22
	LAC 25b	8.4	6.8	24 Jan.	1967 03:37 - 03:57
XXXIII	LAC 56a	4.5	8.2	19 Feb.	1967 00:10 - 00:48
	LAC 56b	7.0	7.1	03 July	1967 13:32 - 14:09
XXXIV	LAC 80a	4.9	11.2	18 Feb.	1967 23:11 - 23:47
	LAC 80b	6.7	7.8	03 July	1967 12:17 - 12:55

APPENDIX C. MEASUREMENT OF POWER
VERSUS DELAY AT 7.5 METERS

The antenna at the AIO is also equipped with a radar operating at a wavelength of 7.5 m (a frequency of 40 Mhz). The moon was observed with this system also, although only the mean scattering behavior of the polarized echo was measured. These measurements agree with those at a wavelength of 6 m,⁹ although the new measurements at the AIO showed slightly stronger backscattering for high angles of incidence.

The scattering behavior near the leading edge was investigated with transmitter pulses of 20 μ s duration (see Figure C.1). The scattering behavior beyond the leading edge was investigated with longer pulses of 100 μ s duration (see Figures C.2 and C.3). When these longer pulses were used, the echo from the leading edge was not accurately determined, because it often exceeded the dynamic range of the recording equipment. This resulted from the use of a high gain, which was necessary to observe echoes near the limb. When plotted, the power of these echoes was fixed at 22 db below the leading edge echo at a delay of one ms. The scattering behavior toward the limb tended toward

$$P(\theta) \propto \cos^{1.3 \pm 0.1} (\theta)$$

where $P(\theta)$ is the power at the angle of incidence θ .

$\lambda = 7.5 \text{ m}$

TRANSMITTER PULSE LENGTH = $20 \mu\text{sec}$

RC FILTER TIME CONSTANT = $7 \mu\text{sec}$

TRANSMITTING RH CIRCULAR

RECEIVING LH CIRCULAR

• KLEMPERER'S MEASUREMENTS

AT 6 METERS

I OBSERVED FLUCTUATION

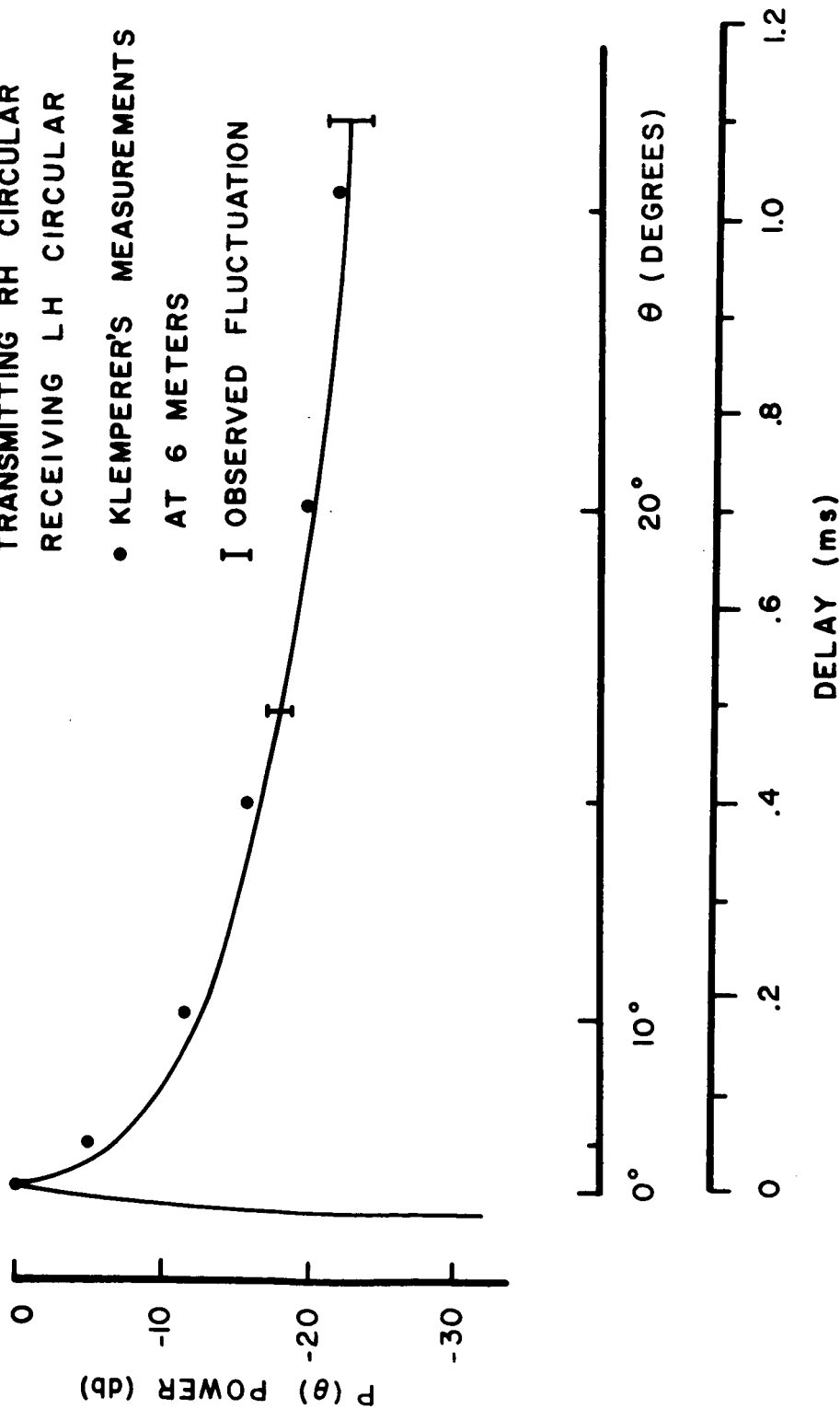


FIGURE C.1. Mean Backscattering Behavior of the Leading Edge of the Moon at a Wavelength of 7.5 m as Examined with Very Short Pulses.

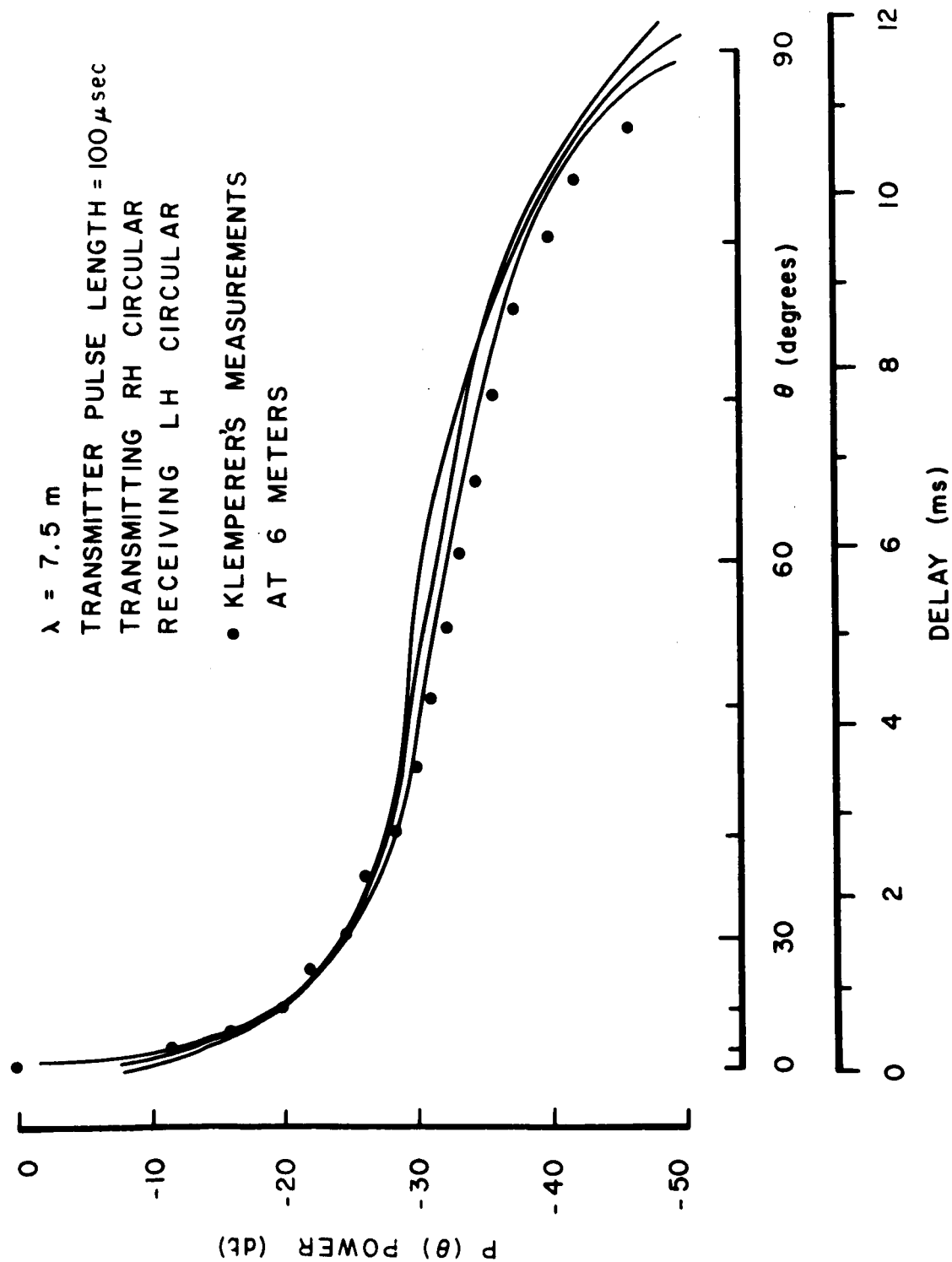


FIGURE C.2. Mean Backscattering Behavior of the Moon at a Wavelength of 7.5 m. (Each curve shows an independent observation. All curves were assumed to be at -22 db at a delay of 1 ms.)

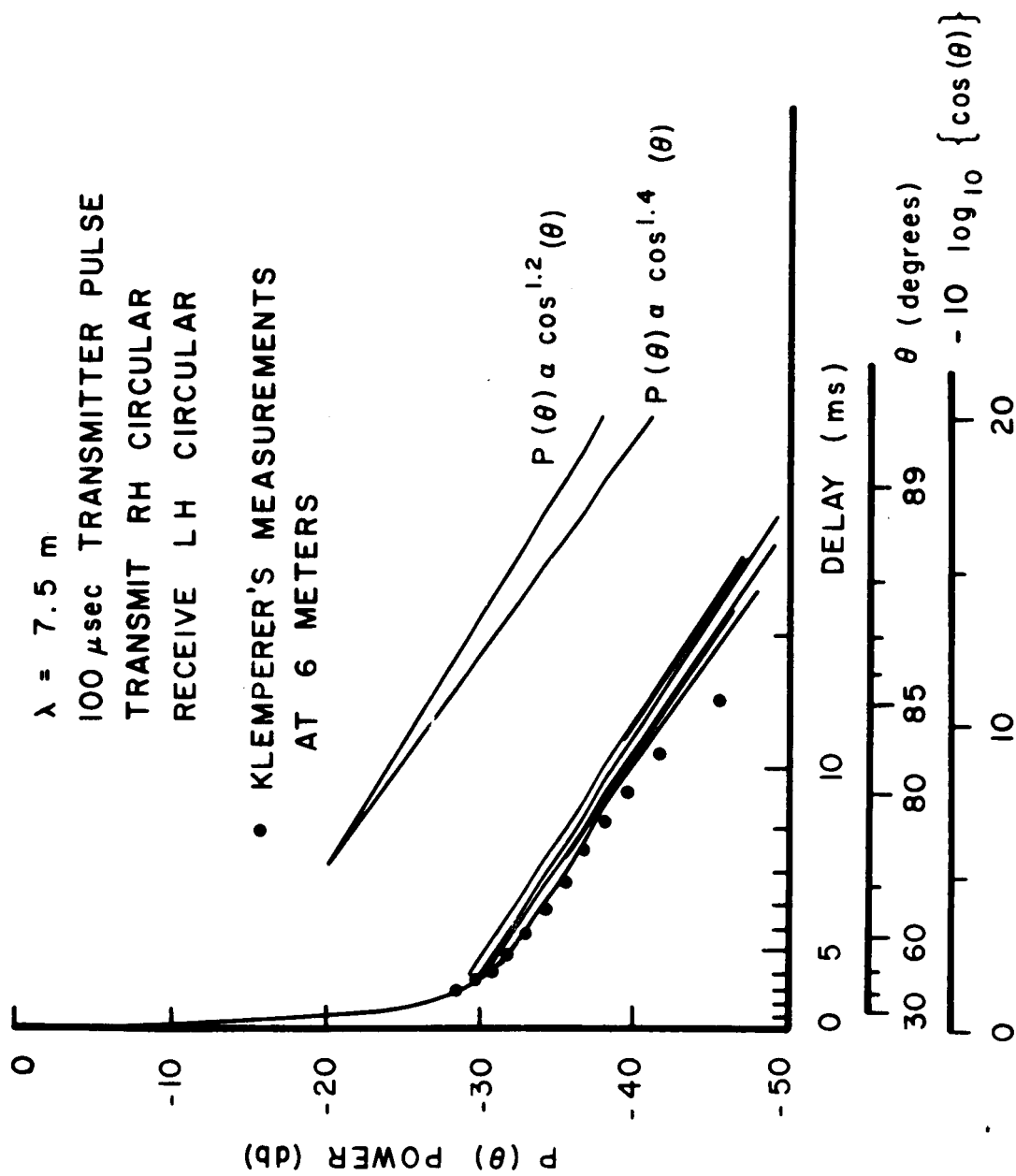


FIGURE C.3. Mean Backscattering Behavior of the Moon for Large Angles of Incidence at a Wavelength of 7.5 m. (Each curve shows an independent observation. All curves were assumed to be at -22 db at a delay of 1 ms.)

REFERENCES

1. R.L. Leadabrand, "Radar Astronomy Symposium Report," Jour. Geophys. Res., 65, 1103-1114, 1960.
2. G.H. Pettengill, "Measurements of Lunar Radar Reflectivity Using the Millstone Radar," Proc. I.R.E., 48, 933-934, 1960.
3. G.H. Pettengill, and J.C. Henry, "Enhancement of Radar Reflectivity Associated with the Lunar Crater Tycho," Jour. Geophys. Res., 67, 4881-4885, 1962.
4. T.W. Thompson and R.B. Dyce, "Mapping of Lunar Radar Reflectivity at 70 cm," Jour. Geophys. Res., 71, 4843-4853, 1965.
5. T.W. Thompson, A Study of Radar Scattering Behavior of Lunar Craters at 70 cm, Ph.D. thesis, published as Internal Report RS 64 (Ithaca, N.Y.: Center for Radio Physics and Space Research, Cornell University, November 1965).
6. T. Hagfors, "A Study of the Depolarization of Lunar Radar Echoes," Radio Science, 2 (new series), 445-465, May 1967.
7. U.S. Aeronautical Chart and Information Center, Lunar Charts, LAC 24 through LAC 95 (St. Louis, Mo., 1964).
8. G.P. Kuiper, Orthographic Atlas of the Moon (Supplement No. 1 to the Photographic Lunar Atlas, Tucson, Arizona: University of Arizona, 1963).

9. W.K. Klemperer, "Angular Scattering Law for the Moon at 6-Meter Wavelength," Jour. Geophys. Res., 70, 3798-4000, 1965.
10. J.V. Evans and G.H. Pettengill, "The Scattering Behavior of the Moon at Wavelengths of 3.6, 68, and 784 Centimeters," Jour. Geophys. Res., 68, 423-442, 1963.

ACKNOWLEDGMENTS

Without the aid and assistance of the following people, this report would not have been written, and the experiment would not have been performed. . Gordon Pettengill and the Computer Group of the Haystack Hill Radar of Lincoln Laboratory have performed invaluable service by providing the computer display of the mapped data and the coding of the Cooley-Tukey algorithm. The coding of computer programs at the AIO was performed by Hiram Cabassa. The observations were carried out with the help of the Observer Group at the AIO. Several drafts were typed by Mercedes Vives, and the final draft by Elma Weaver. This report was edited by A. M. Wilkinson.

PLATES OF RADAR MAPS

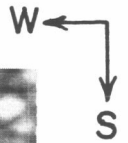
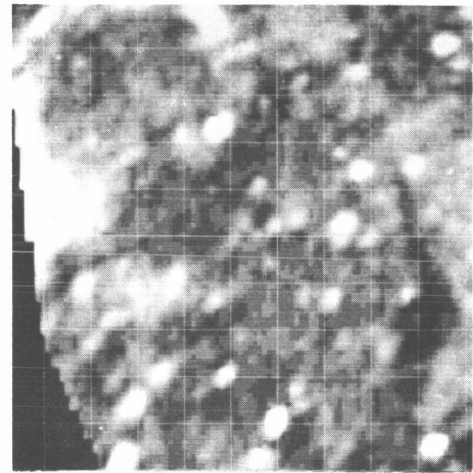
Plate I

LAC 24 SINUS IRIDUM

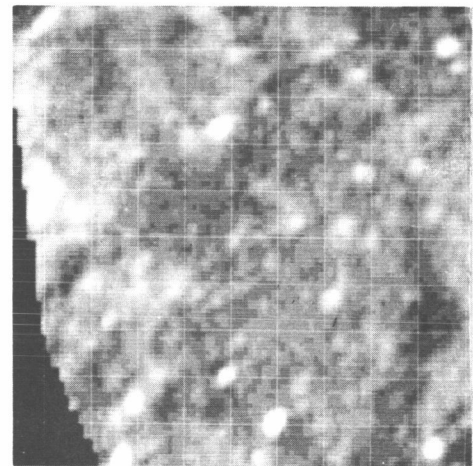
Longitude = -38° , -14° Latitude = 32° , 48°

The Montes Jura, which surrounds Sinus Iridum, were rougher than the adjacent maria regions. A difference in roughness was observed between longitudes -16° and -14° (right). This area is lighter in full-moon photographs. Many isolated craters showed enhanced back-scattering.

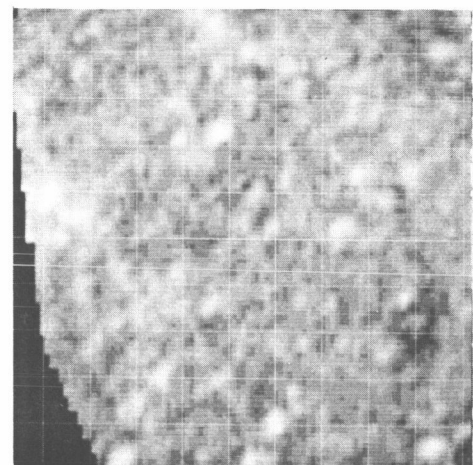
Depolarized



Polarized



Ratio



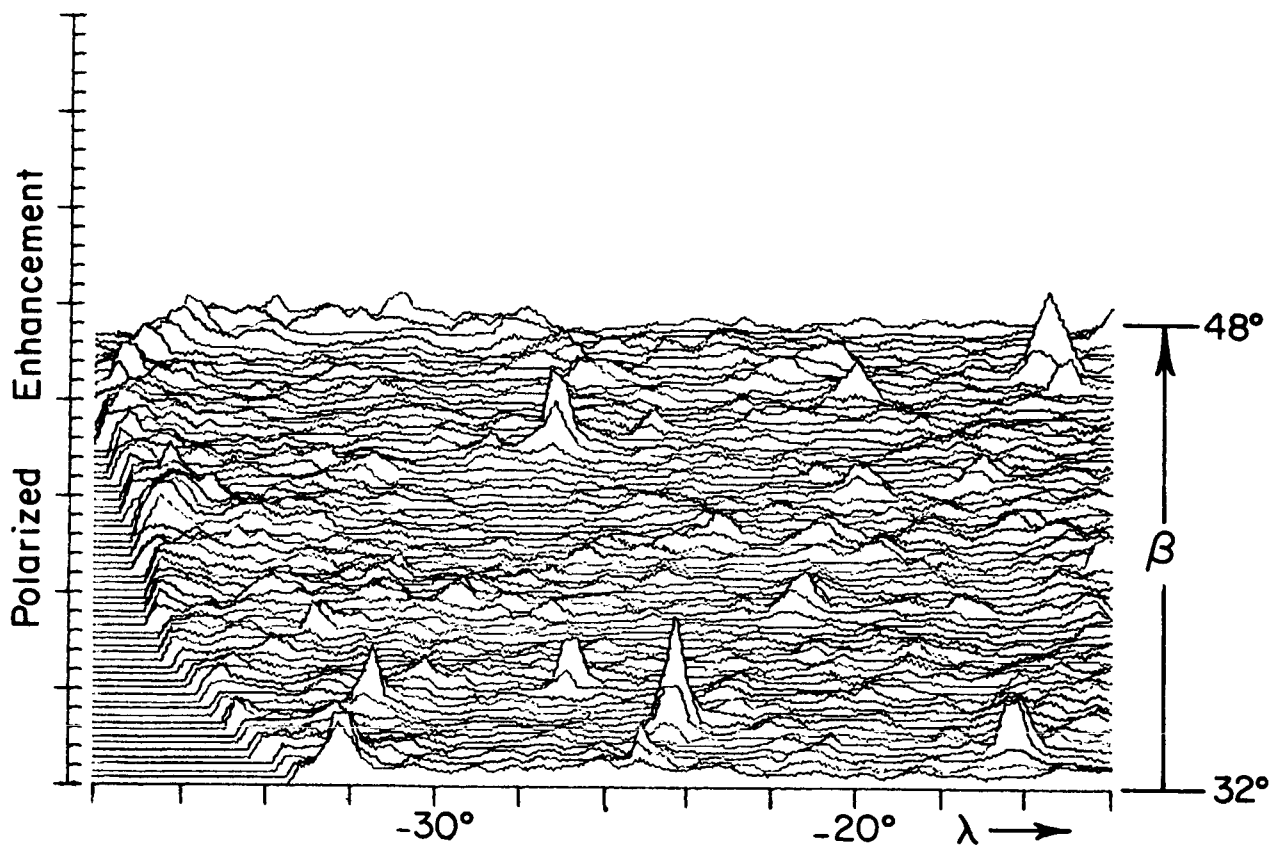
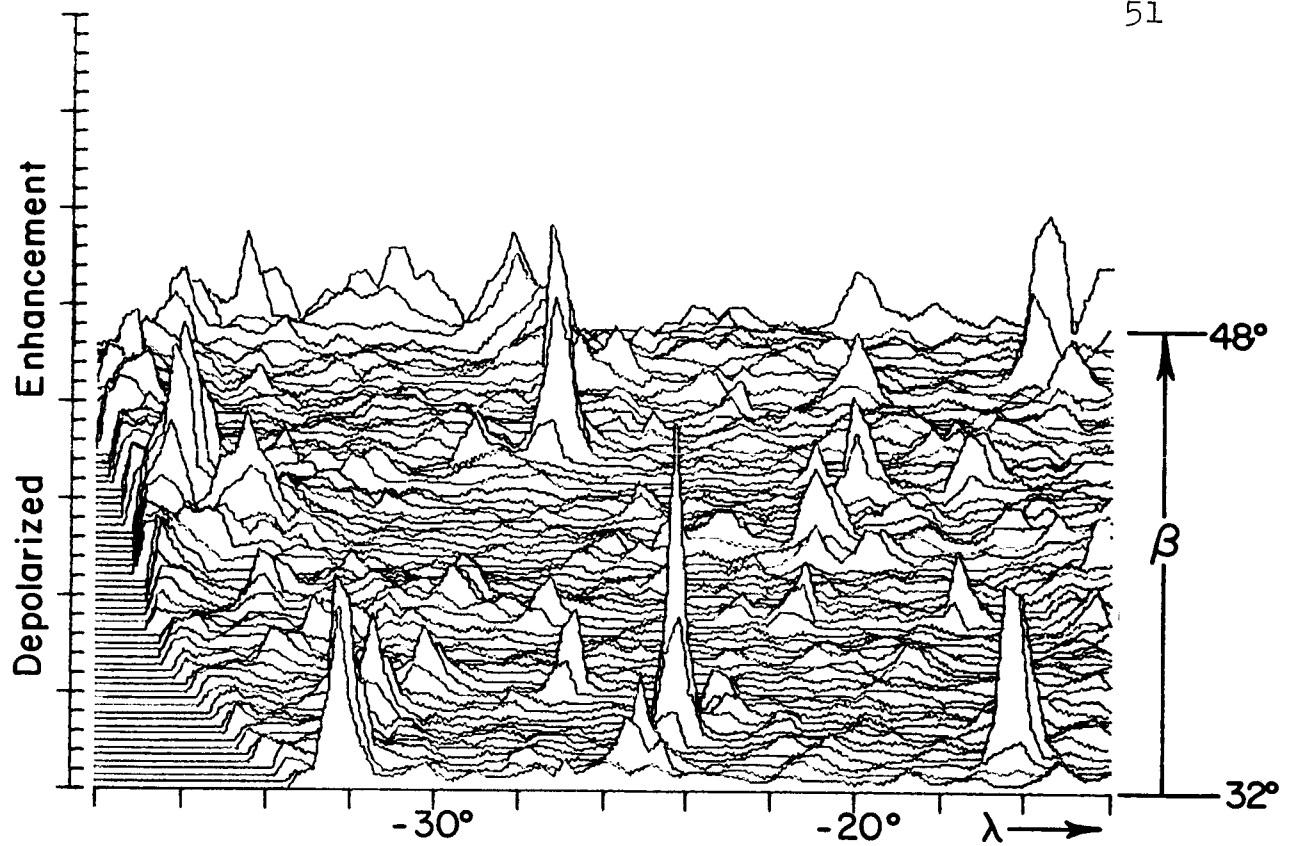


Plate i. Isometric Plot of Radar Map of Plate I,
LAC 24 Sinus Iridium.

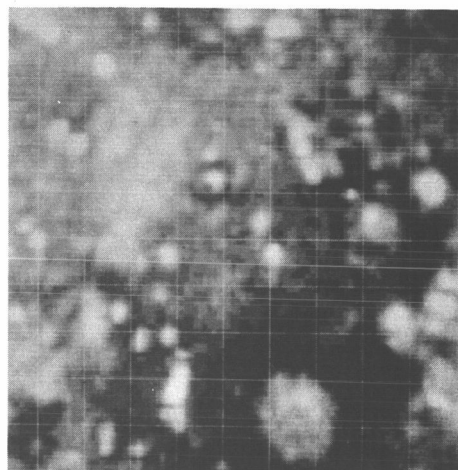
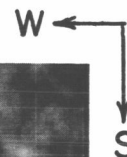
Plate II

LAC 25 CASSINI

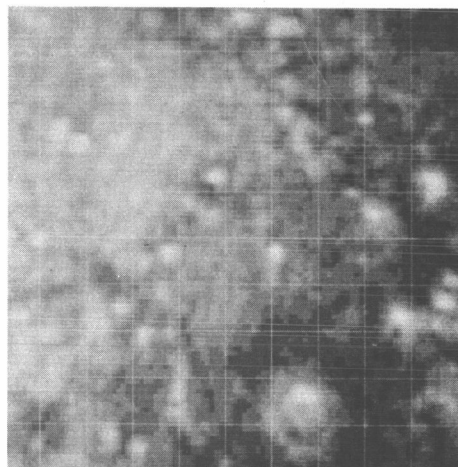
Longitude = -14° , 10° Latitude = 32° , 48°

The portion of Mare Imbrium observed as a rough area (middle left) is not correlated with any optical feature. The crater Aristillus was rough and showed a specular return from its far (north) rim. The mountain ridges of Montes Teneriffe and Montes Spitzbergensis, the isolated mountains of Pico, Pico β , and Piton, and the mountains on the eastern shore of Mare Imbrium were rougher than their environs. The Montes Caucasus in the south-east showed increased roughness. (See also Plates XXVI and XXXII.)

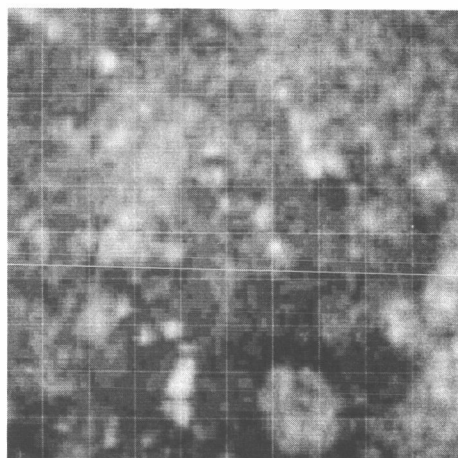
Depolarized



Polarized



Ratio



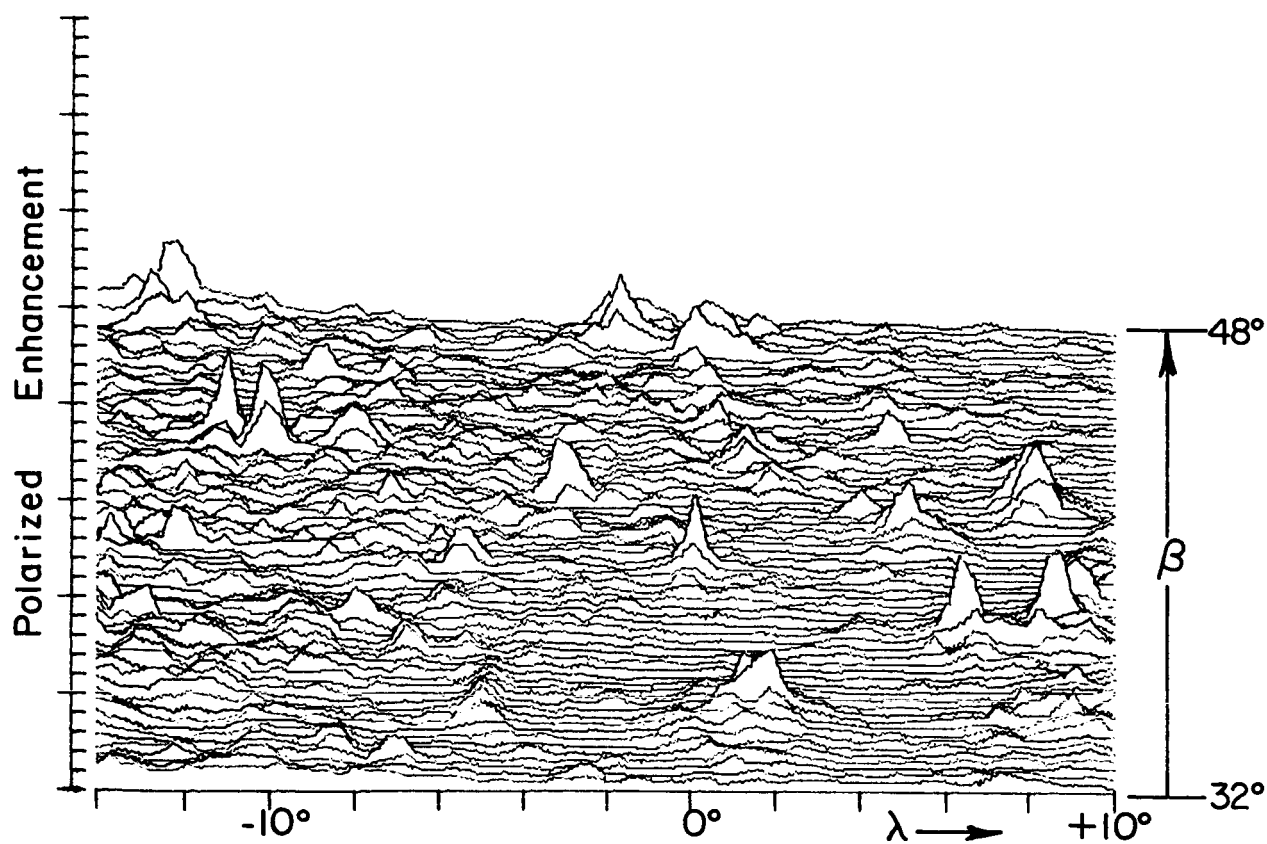
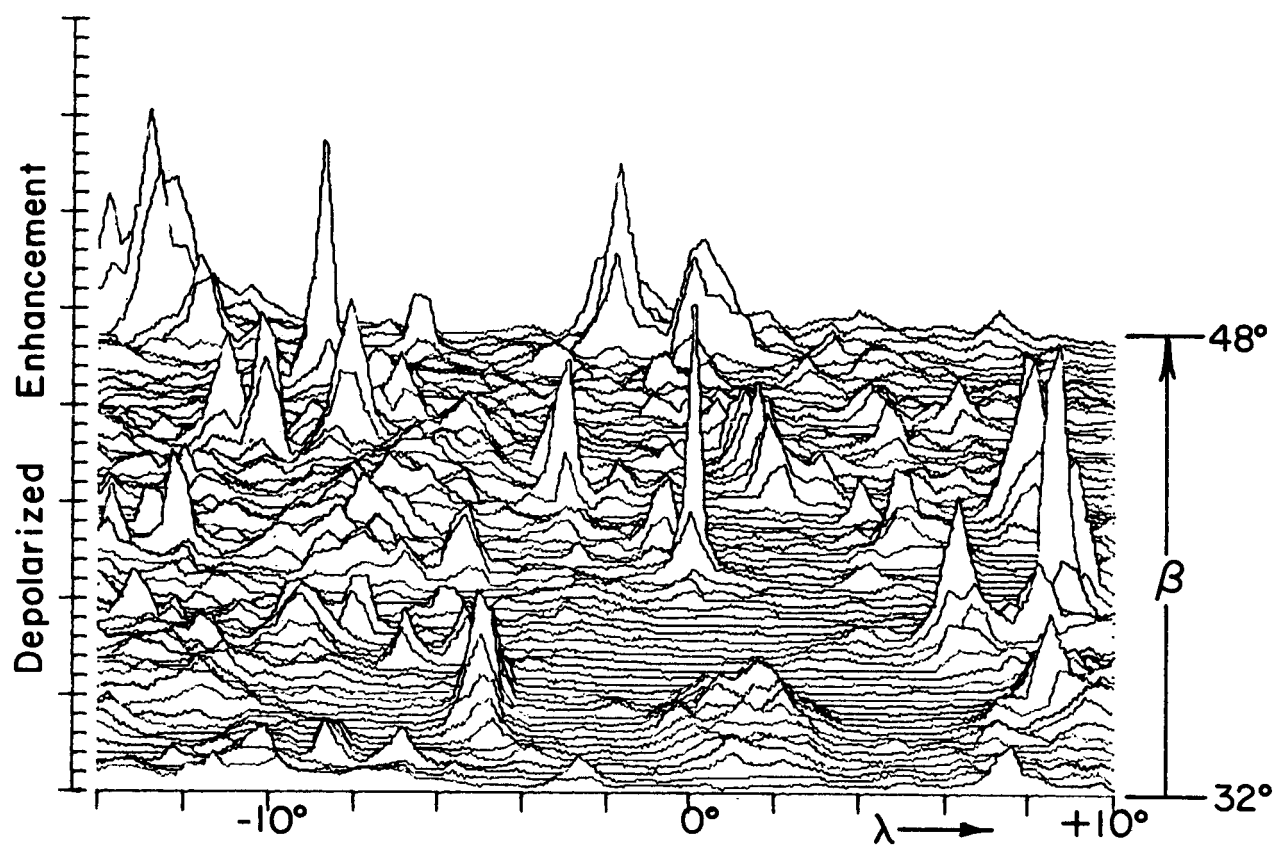


Plate ii. Isometric Plot of Radar Map of Plate II,
LAC 25 Cassini.

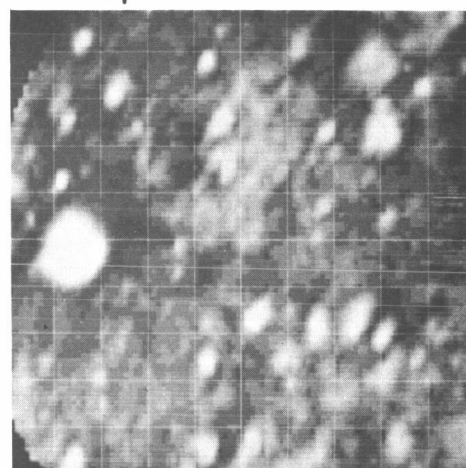
Plate III

LAC 39 ARISTARCHUS

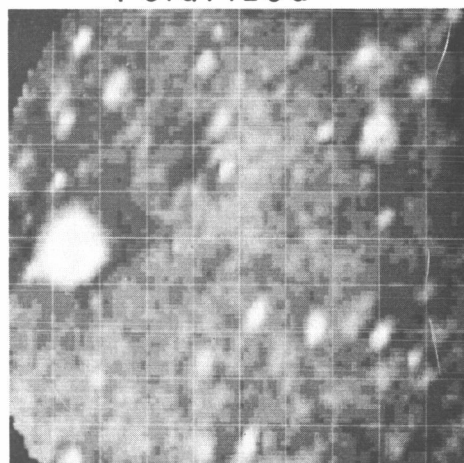
Longitude = -50° , -30° Latitude = 16° , 32°

The rayed crater Aristarchus was observed as the rough area in the west. The Montes Harbinger, which are east of Aristarchus, were slightly rougher than the adjacent maria. Numerous craters showed enhanced backscattering.

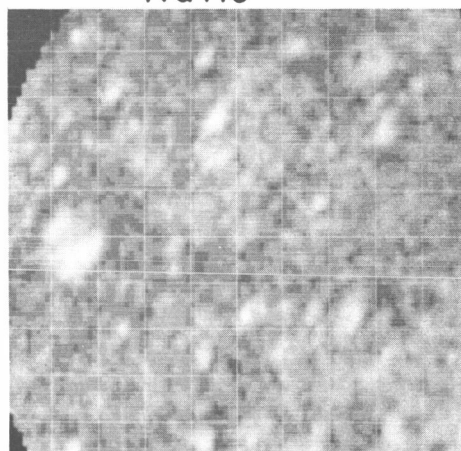
Depolarized



Polarized



Ratio



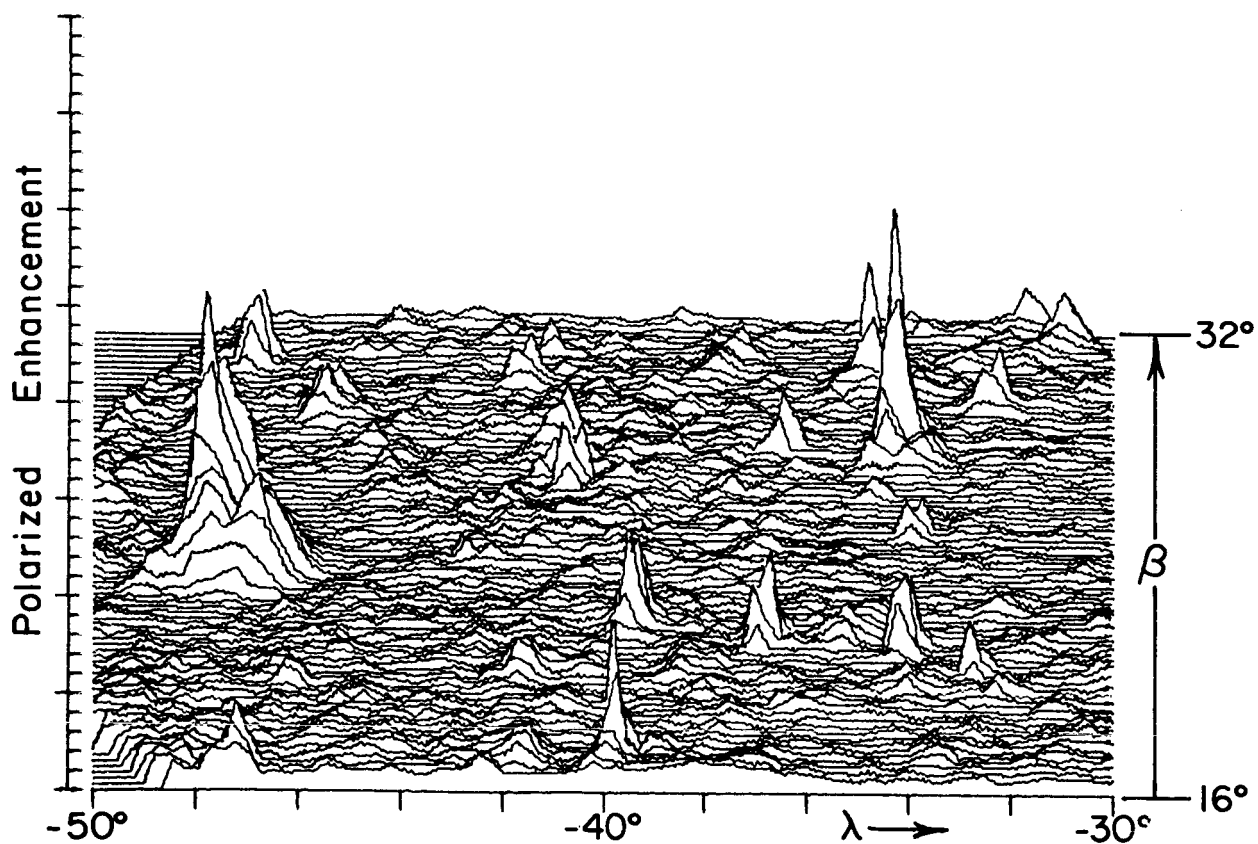
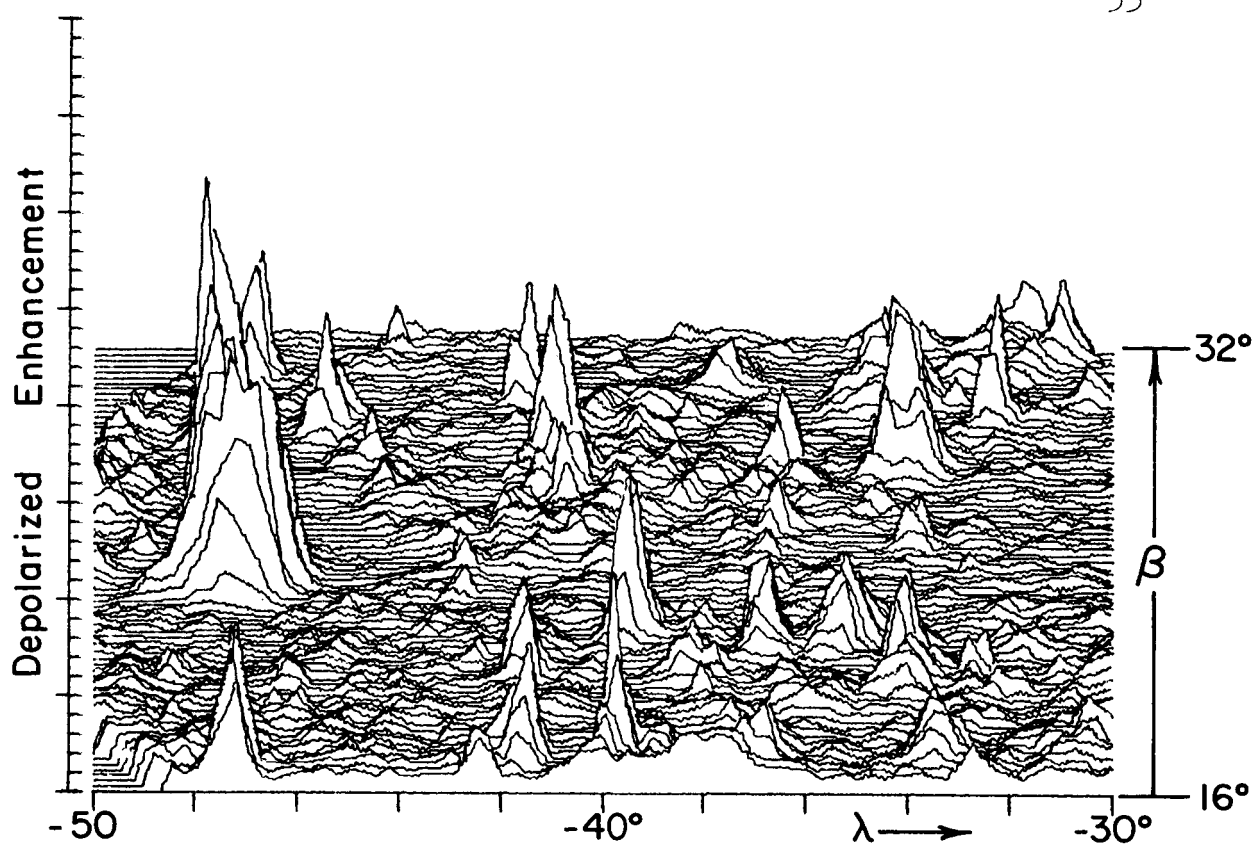


Plate iii. Isometric Plot of Radar Map of Plate III,
LAC 39 Aristarchus.

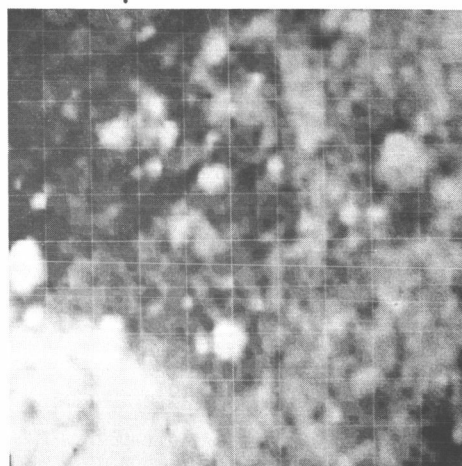
Plate IV

LAC 40 TIMOCHARIS

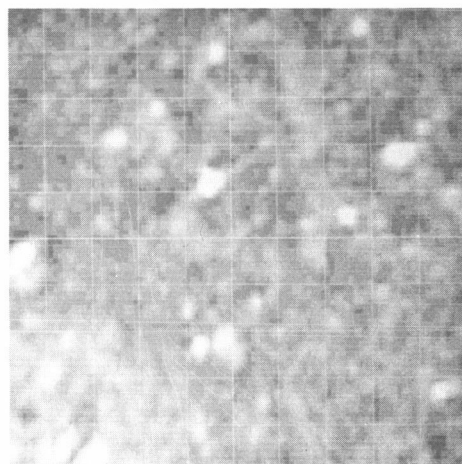
Longitude = -30° , -10° Latitude = 16° , 32°

The high returns in the southwest corner of the depolarized map are probably due to leakage of high polarized returns from the crater Tycho, which was in the conjugate reflecting area. La Hire, an isolated mountain peak, showed an enhancement that was due to increased roughness. All other backscattering enhancements were identified with craters. The larger craters showed specular highlights from their far (north) rims.

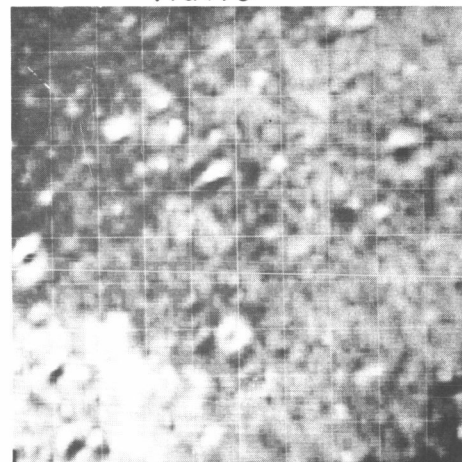
Depolarized



Polarized



Ratio



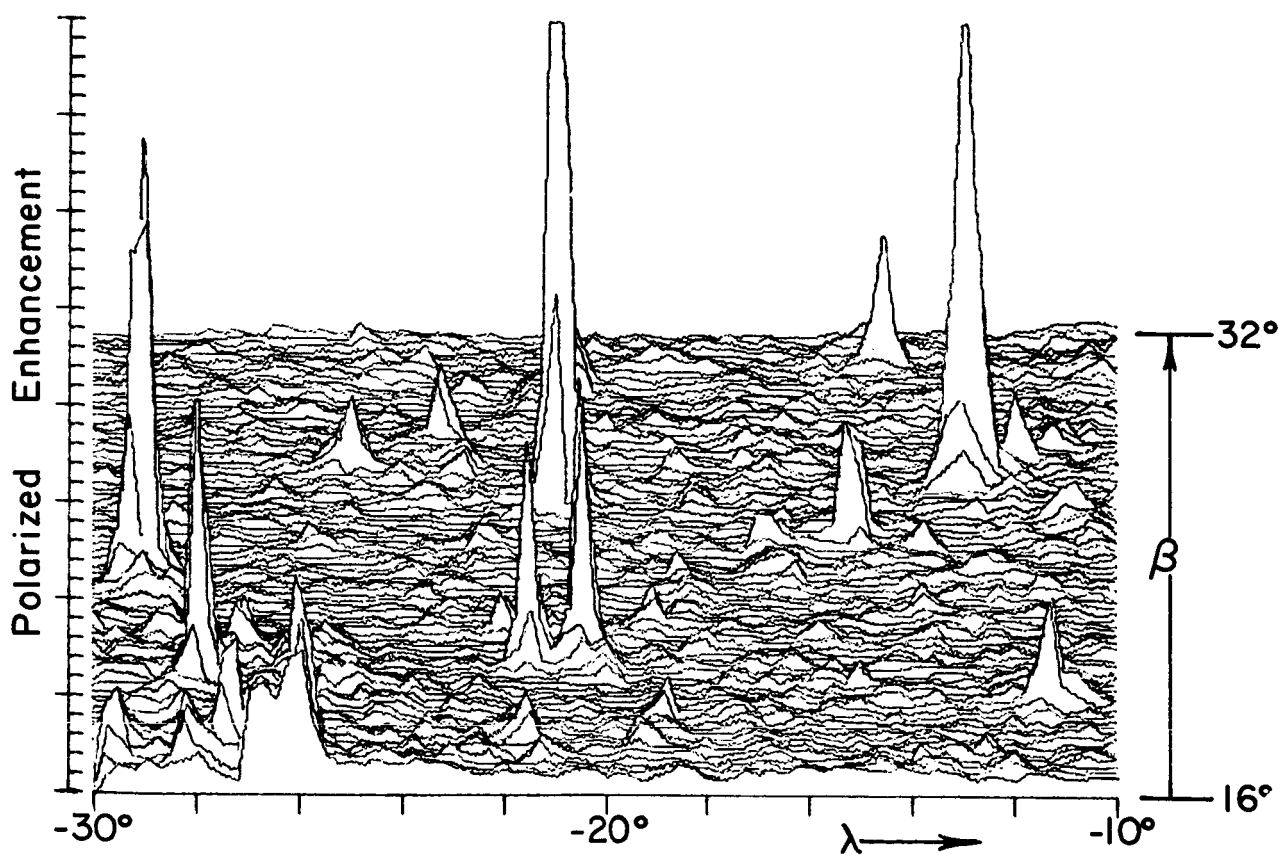
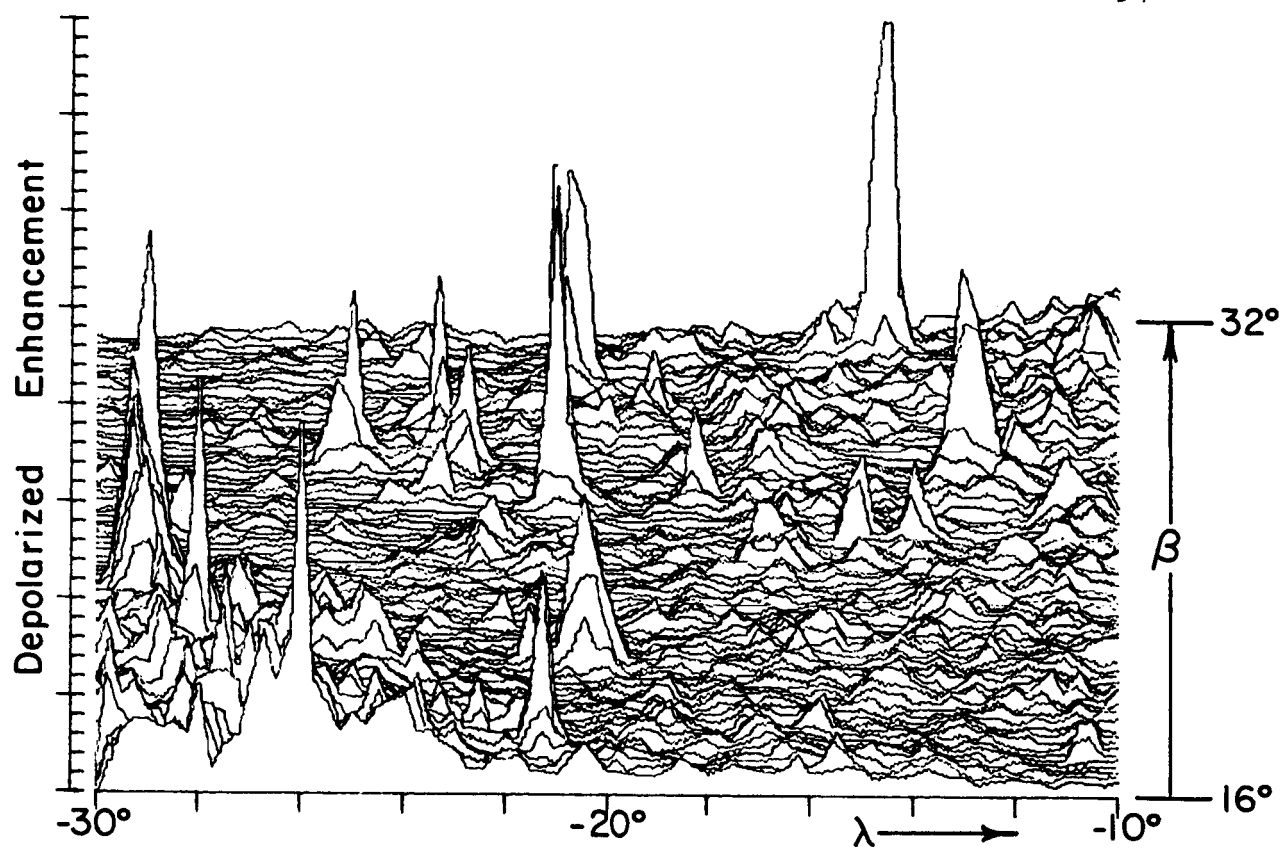


Plate iv. Isometric Plot of Radar Map of Plate IV,
LAC 40 Timocharis.

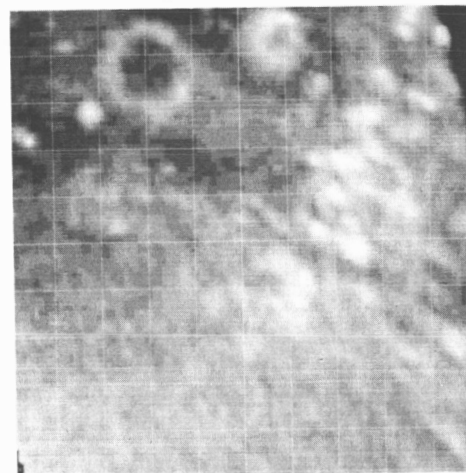
Plate V

LAC 41 MONTES APENNINUS

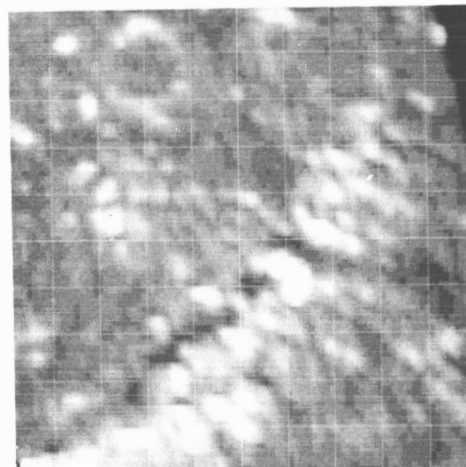
Longitude = -10° , $+10^{\circ}$ Latitude = 16° , 32°

The Montes Apenninus (center) showed specular highlights, an expected result for backscattering near the leading edge. The crater Archimedes, in the north, showed only a rough rim. The crater Autolycus, also in the north, appeared to be rough and showed a specular highlight from its far (north) rim. Several small craters showed specular highlights.

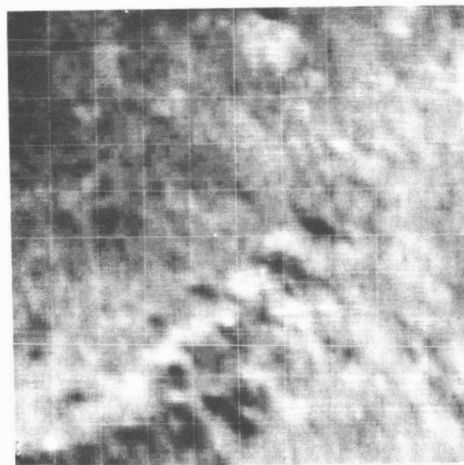
Depolarized



Polarized



Ratio



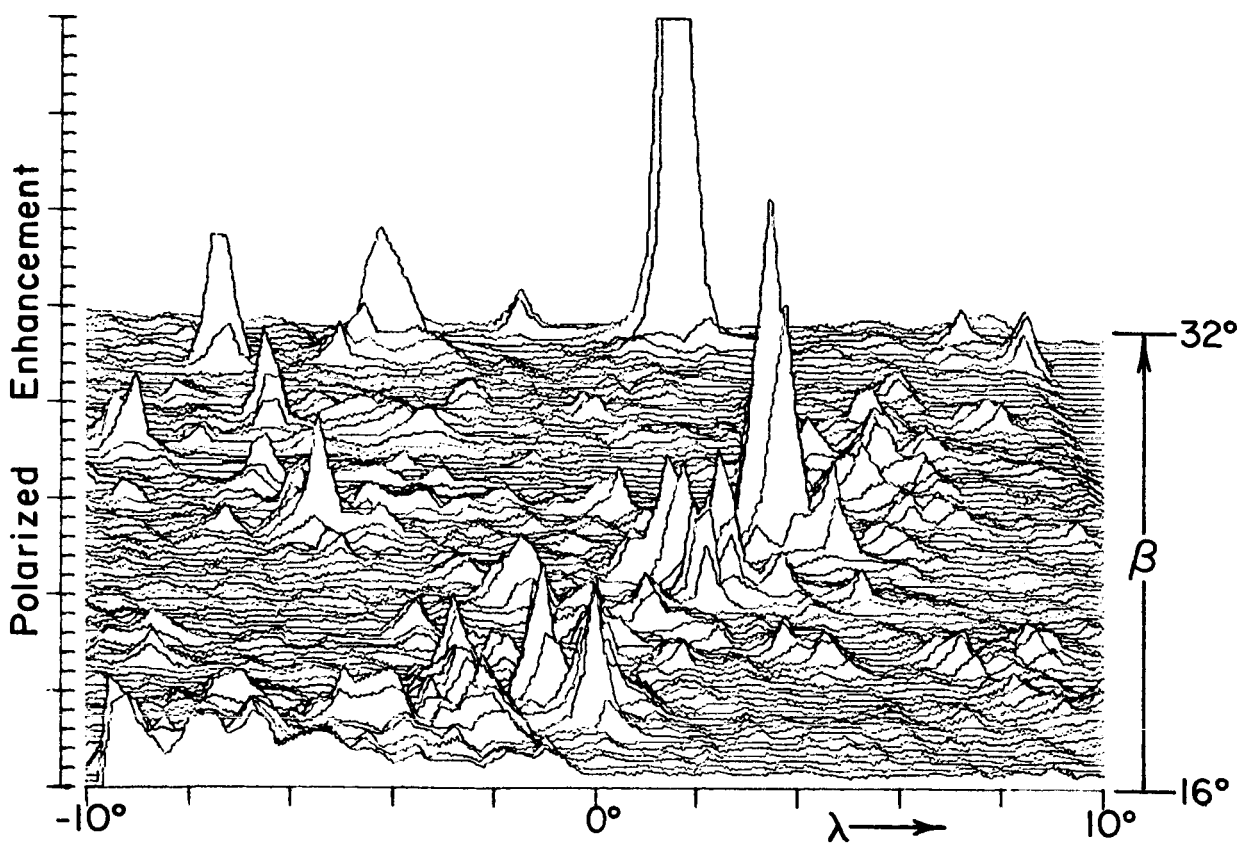
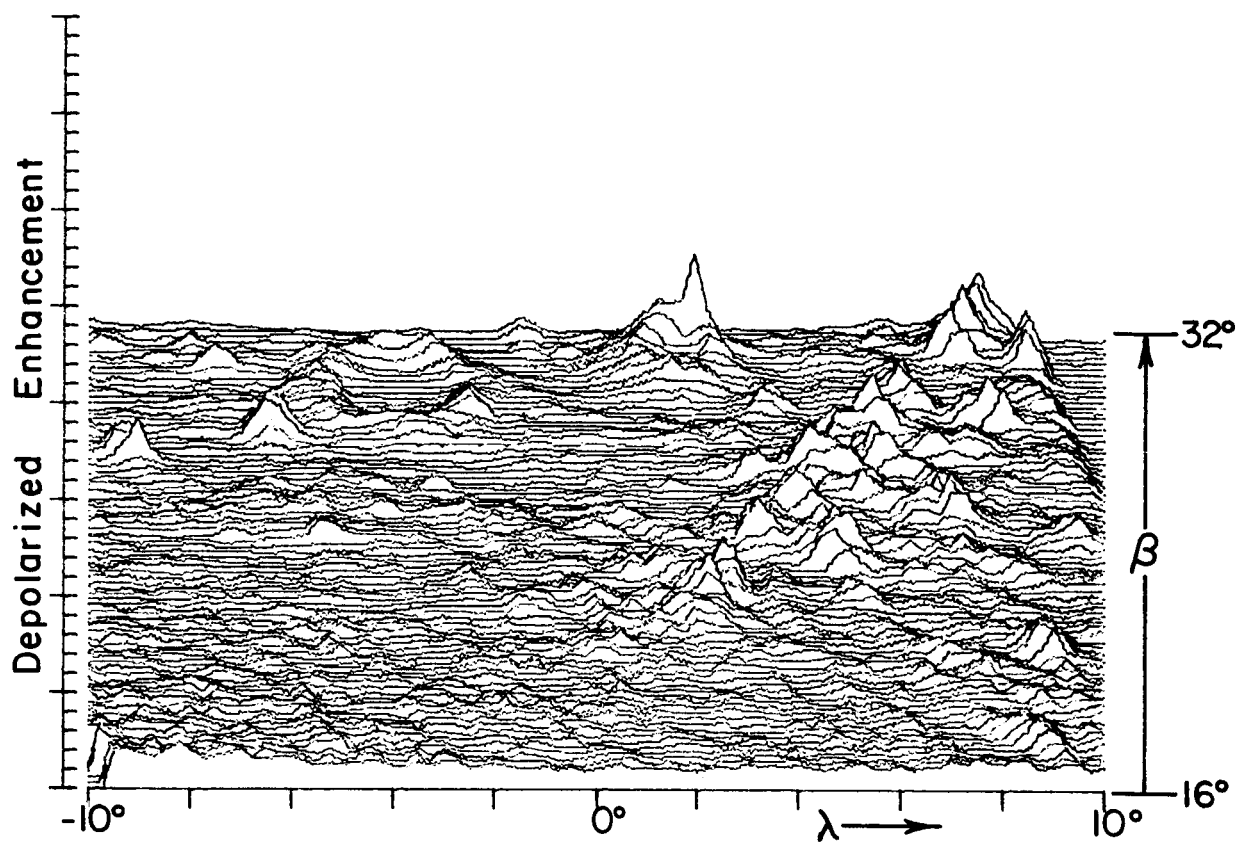


Plate v. Isometric Plot of Radar Map of Plate V,
LAC 41 Montes Apenninus.

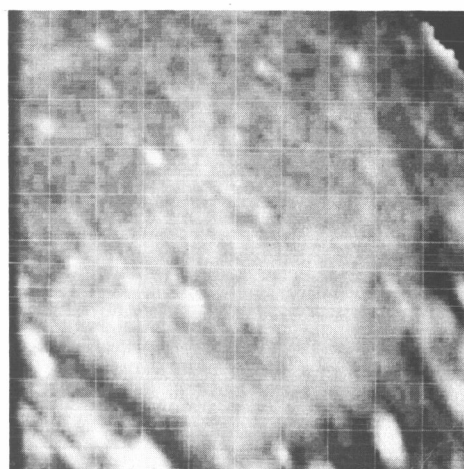
Plate VI

LAC 42 MARE SERENITATIS

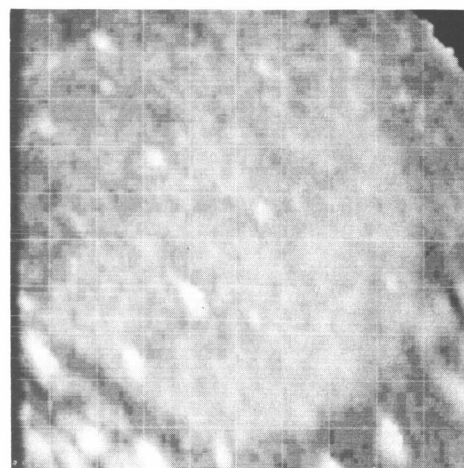
Longitude = 10° , 30° Latitude = 16° , 32°

The features of this map appear to be smeared along contours of constant delay, an indication of an error in the compensation for the Doppler frequency of the echo. The south and east "coasts" of Mare Serenitatis were smoother than the remaining maria and correspond to the dark coasts seen in the full-moon photographs. The famous crater Linne' showed an enhancement, but was not resolved. Several other small craters showed enhancements.

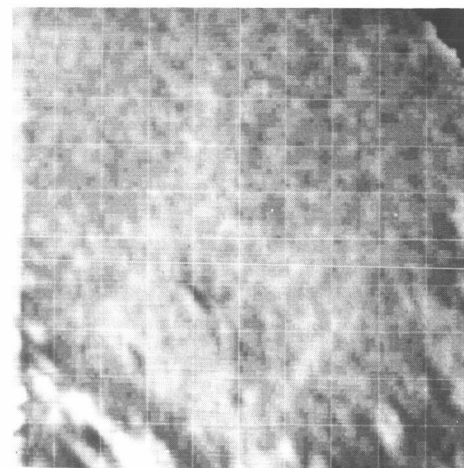
Depolarized



Polarized



Ratio



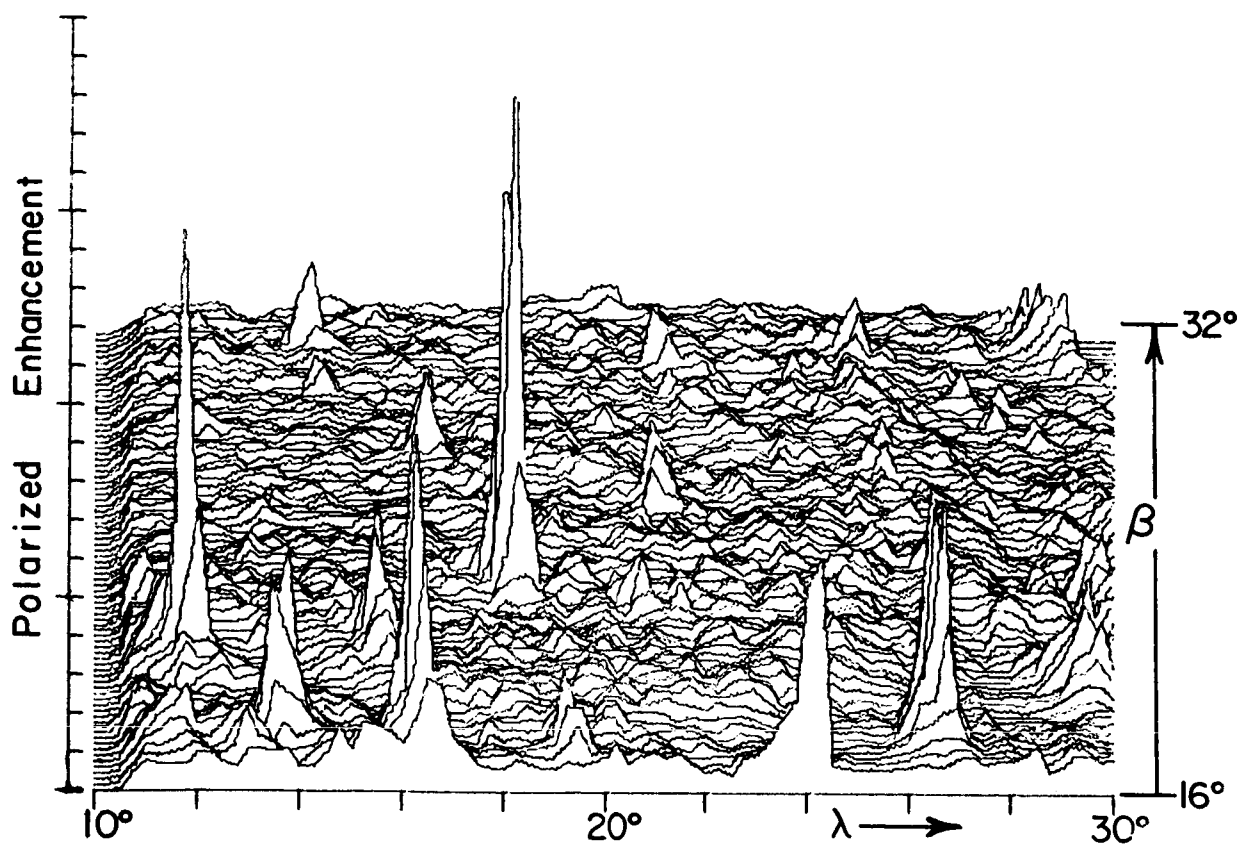
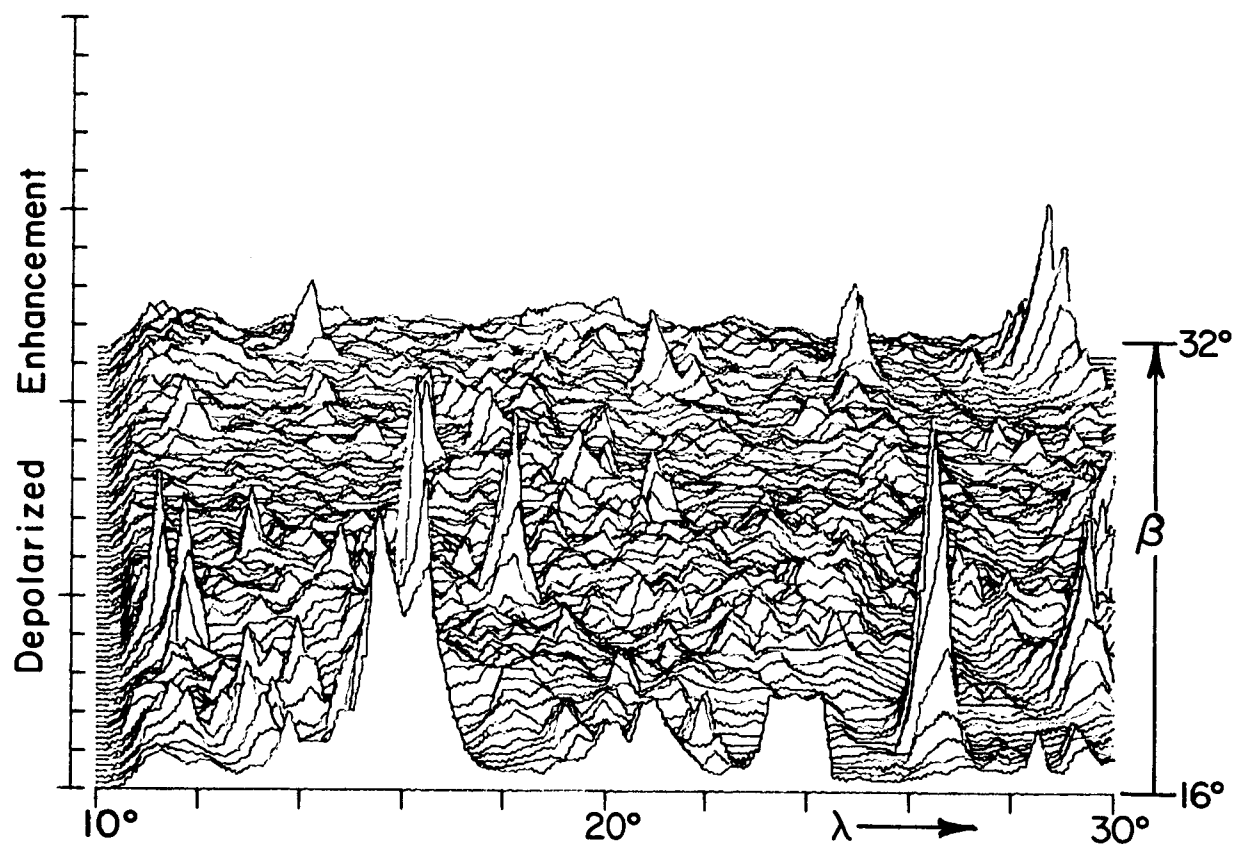


Plate vi. Isometric Plot of Radar Map of Plate VI,
LAC 42 Mare Serenitatis.

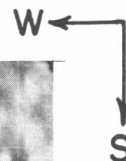
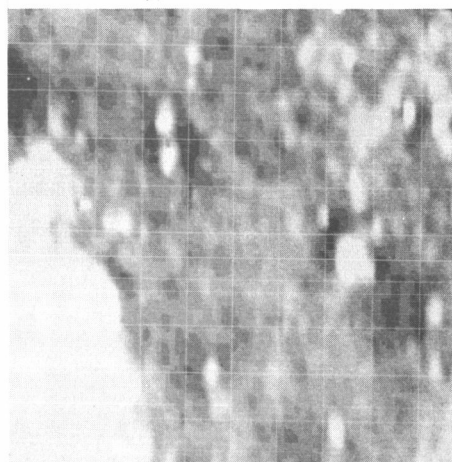
Plate VII

LAC 56 HEVELIUS

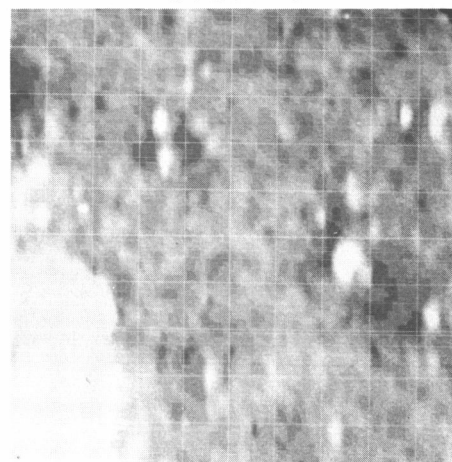
Longitude = -70° , -50° Latitude = 0° , 16°

The rough areas in the west are identified as the craters Hevelius and Cavalerius. The far (west) rims showed a highlight in both polarizations. The hills near Cavalerius D, in the west, and Marius, in the northeast, were slightly rougher than the adjacent maria. Enhancements were observed for several small craters. Another mapping of this area is shown in Plate XXXIII.

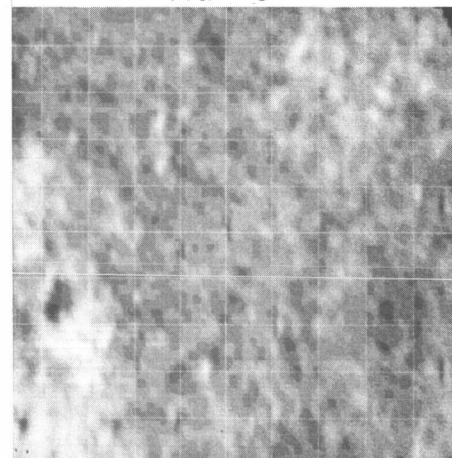
Depolarized



Polarized



Ratio



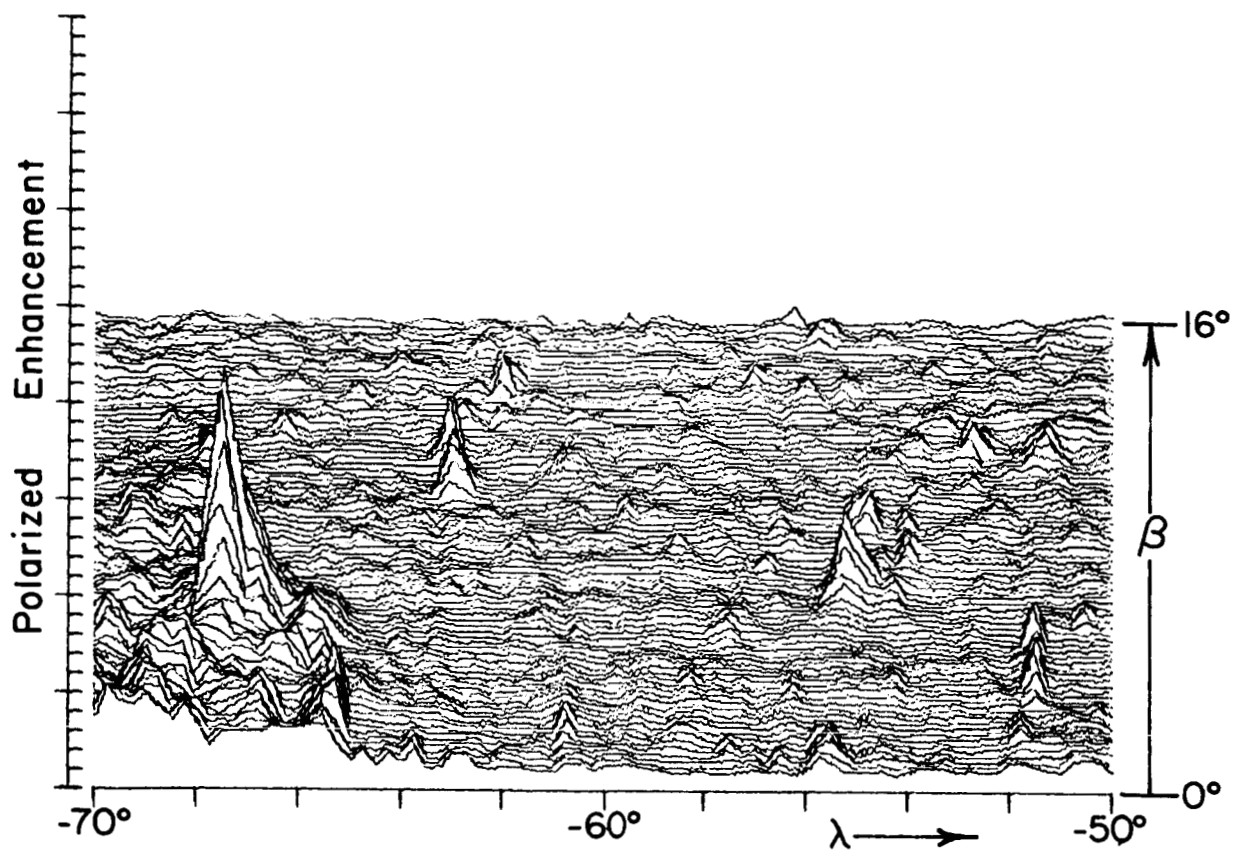
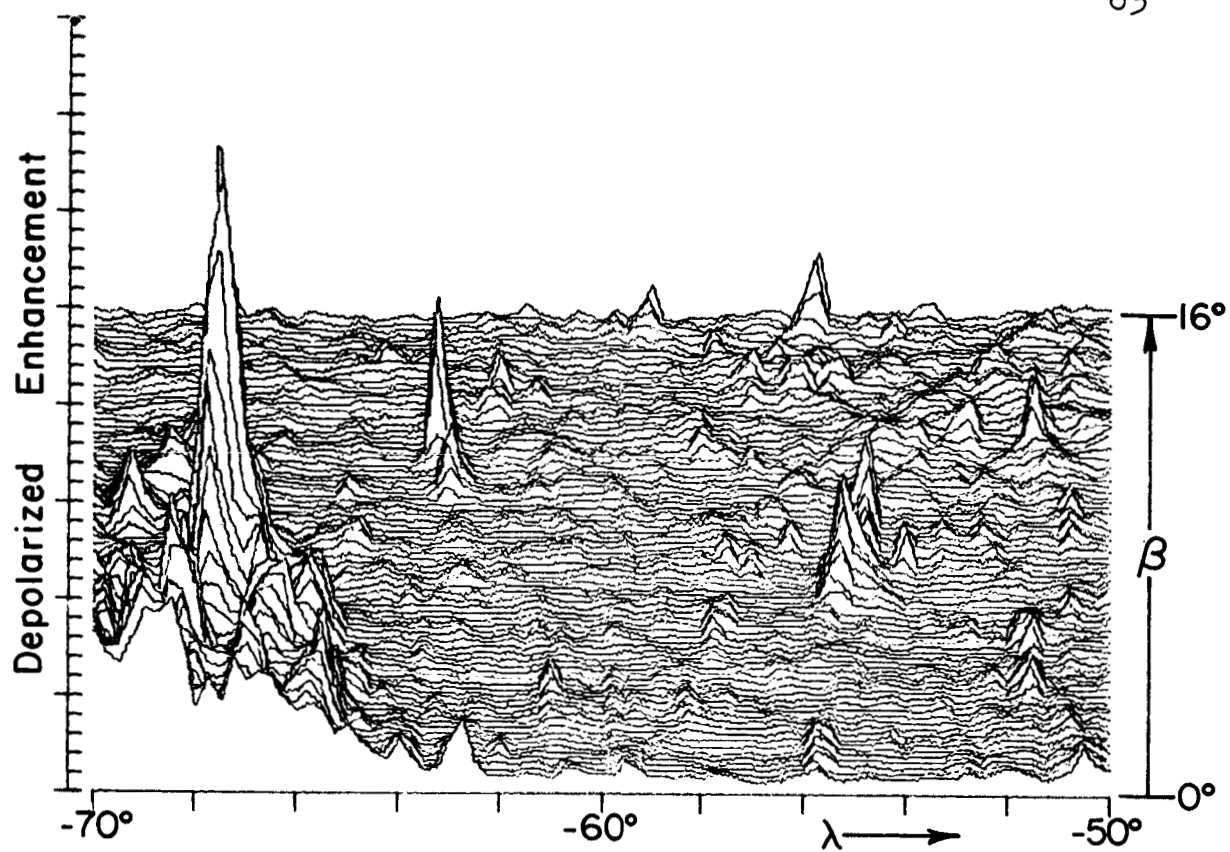


Plate vii. Isometric Plot of Radar Map of Plate VII,
IAC 56 Hevelius.

Plate VIII

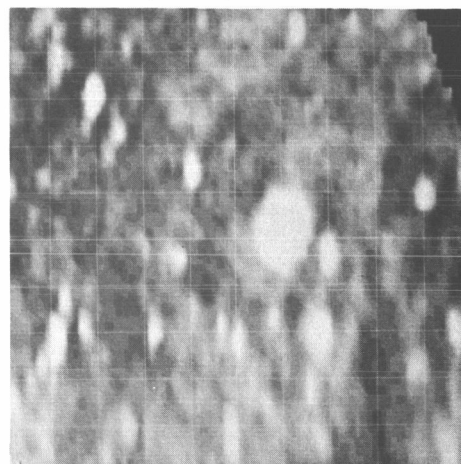
LAC 57 KEPLER

Longitude -50° , -30°

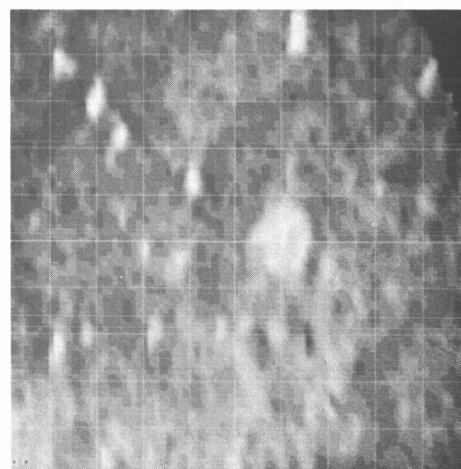
Latitude = 0° , 16°

The extremely rough feature near the center of the map is the rayed crater, Kepler. Many smaller craters also appeared to be rough.

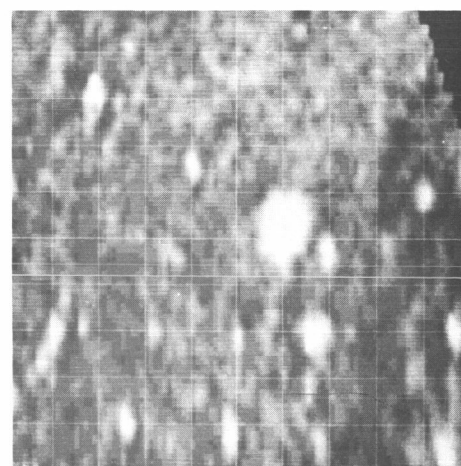
Depolarized



Polarized



Ratio



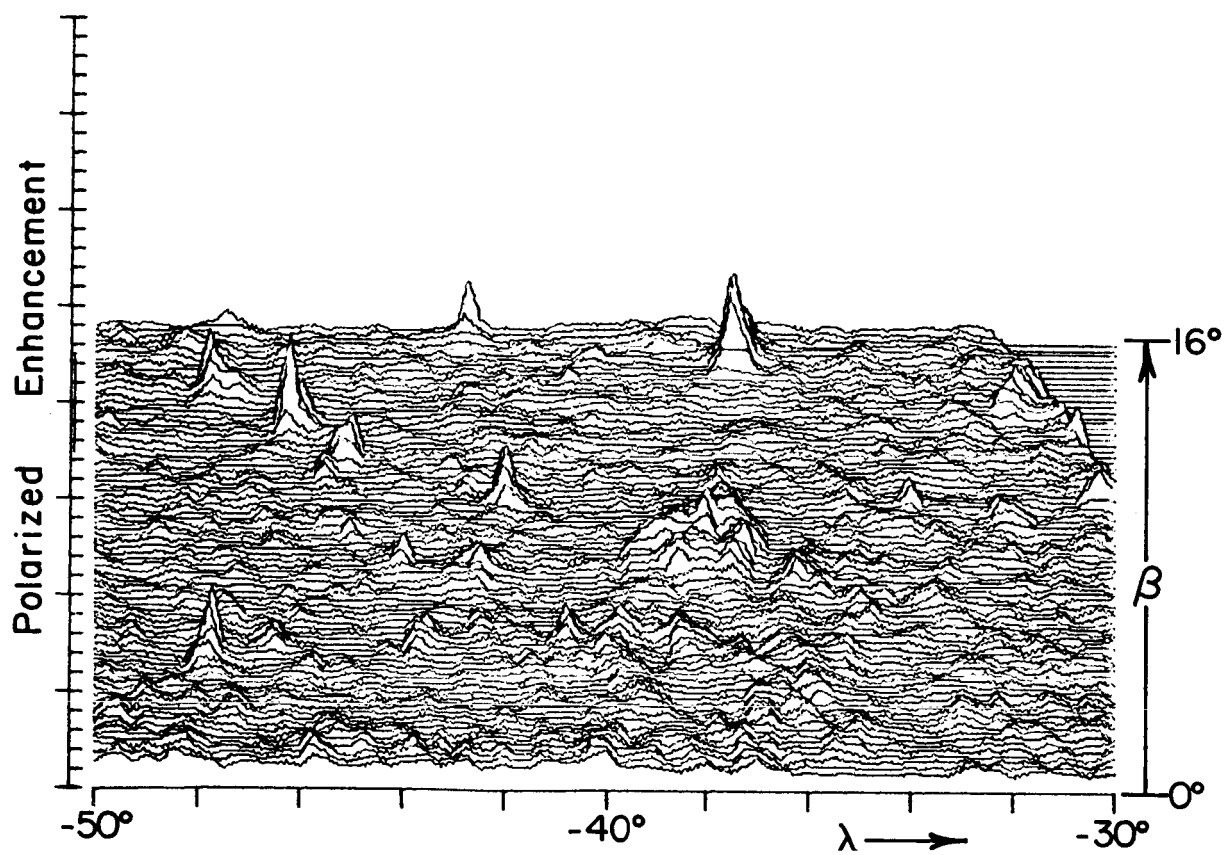
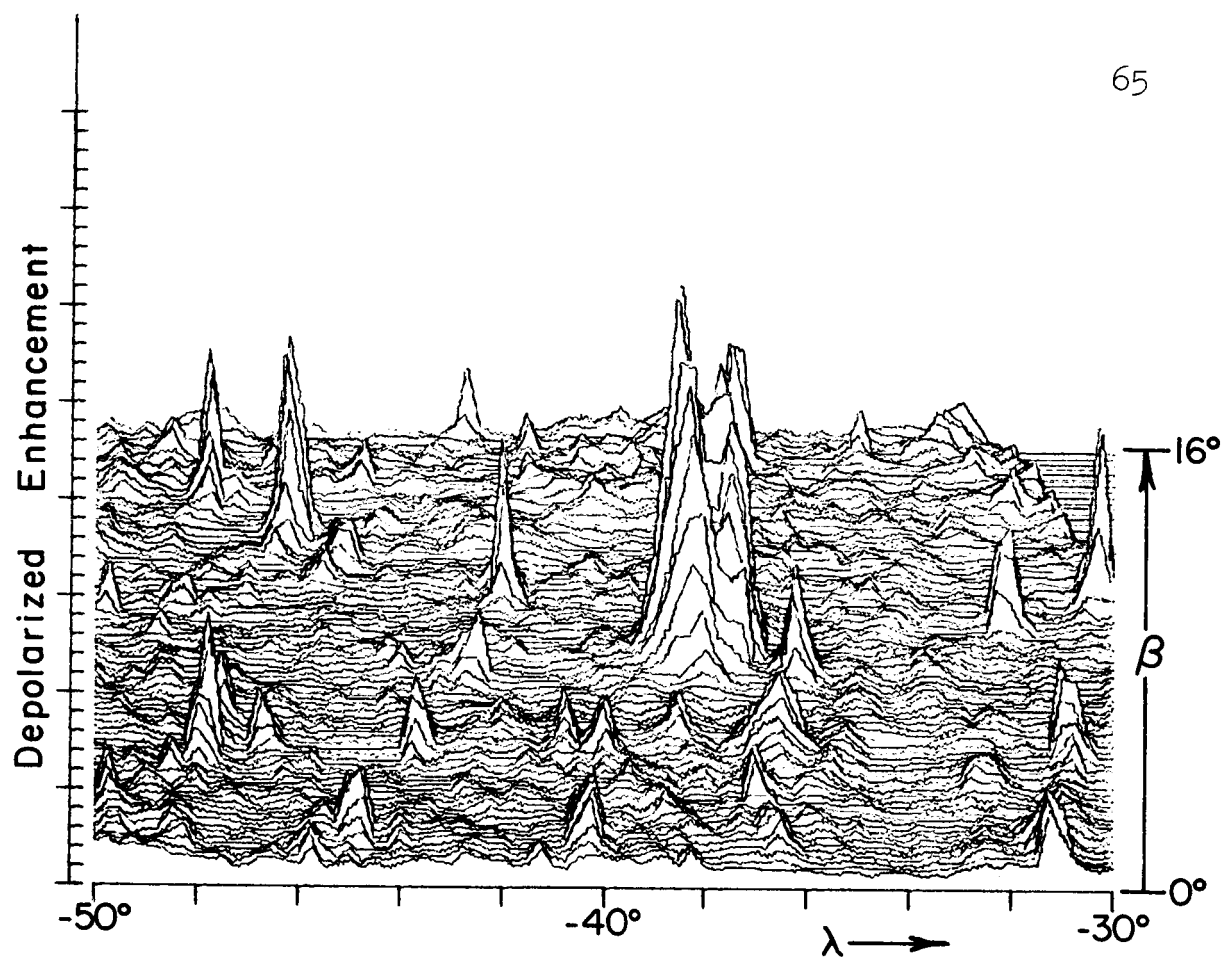


Plate viii. Isometric Plot of Radar Map of Plate VIII,
LAC 57 Kepler.

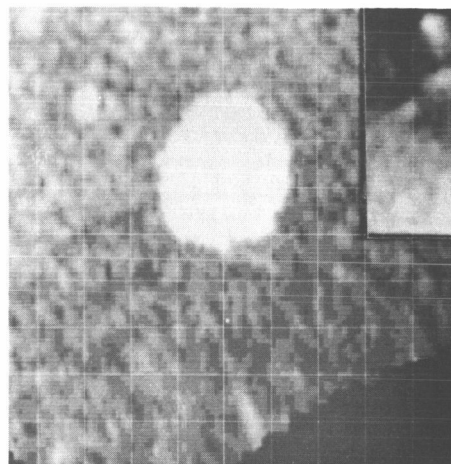
Plate IX

LAC 58 COPERNICUS

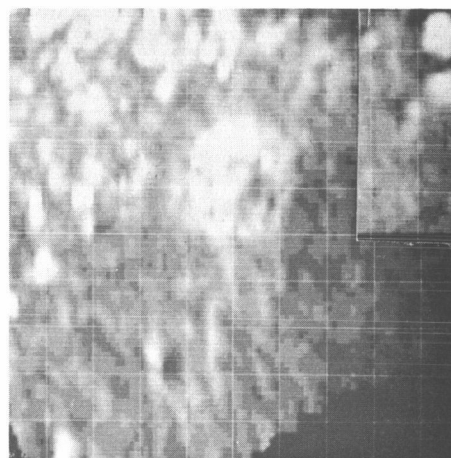
Longitude = -30° , -10° Latitude = 0° , 16°

The large rough area in the center of the map is the rayed crater Copernicus. Plate XXX shows this crater mapped with a twofold improvement in resolution. The Montes Carpatius in the north and several smaller craters showed specular highlights.

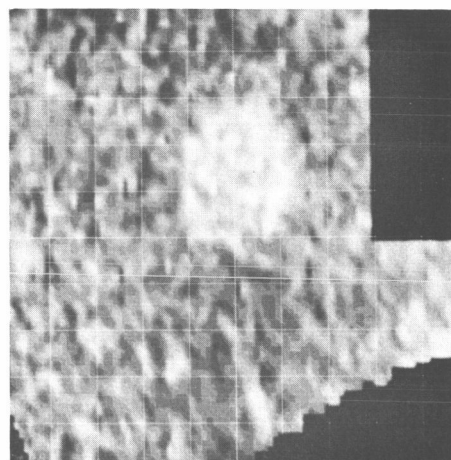
Depolarized



Polarized



Ratio



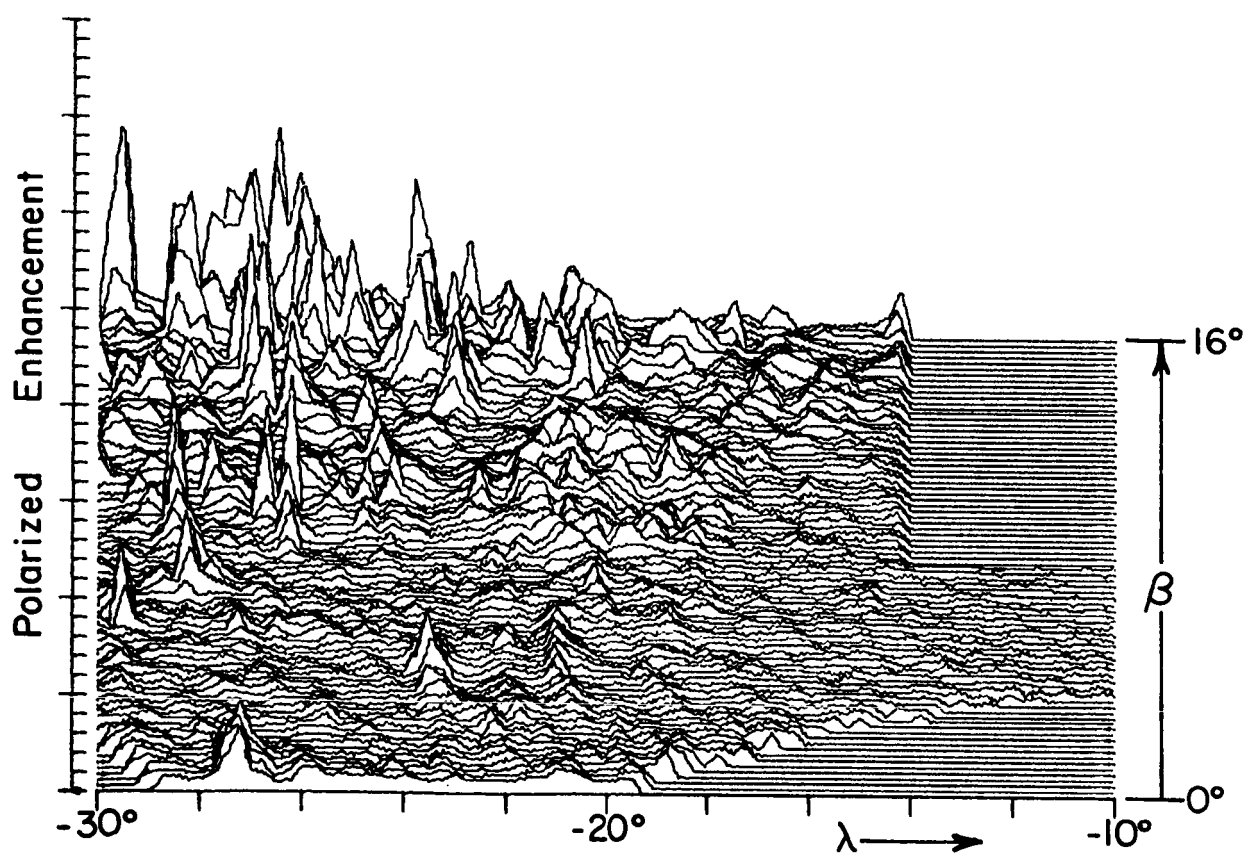
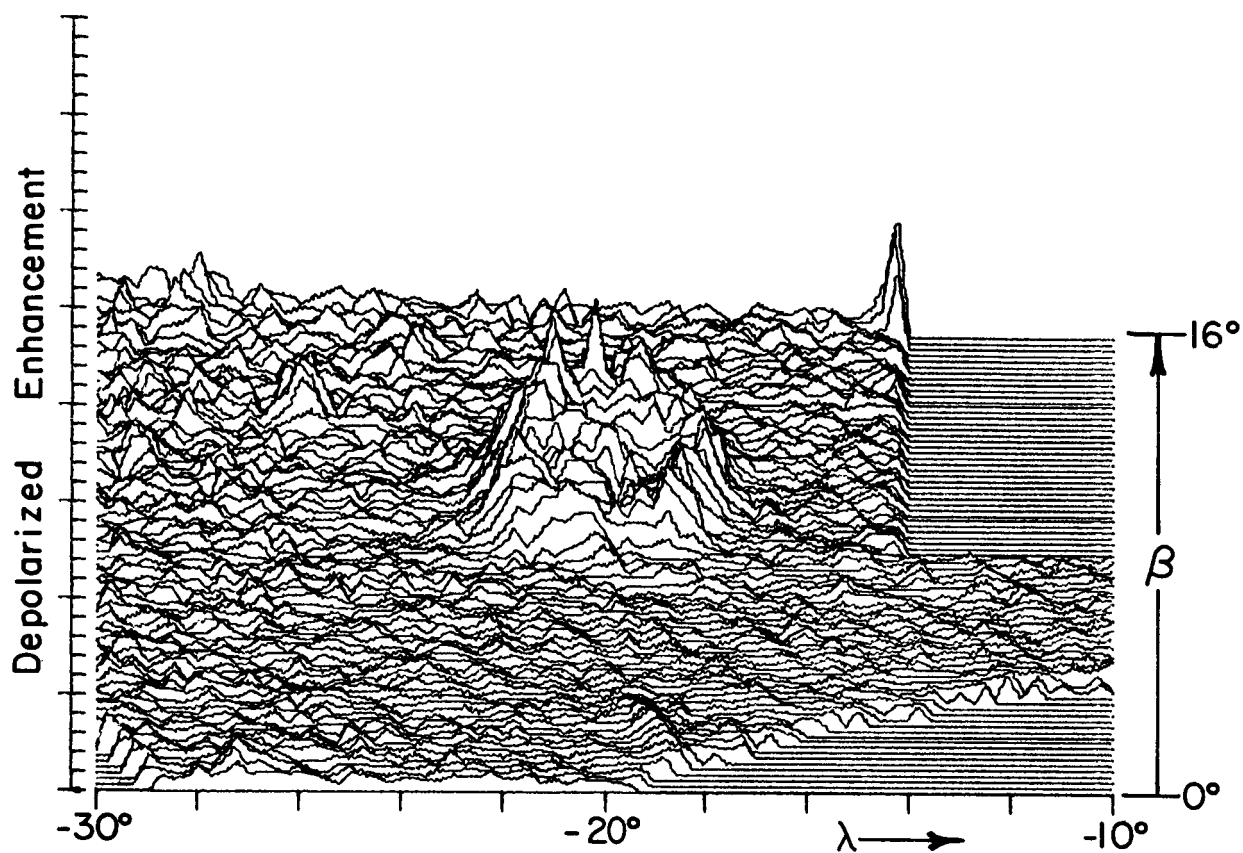


Plate ix. Isometric Plot of Map of Plate IX,
LAC 58 Copernicus.

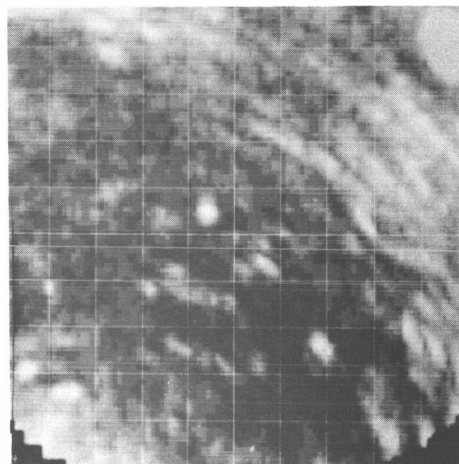
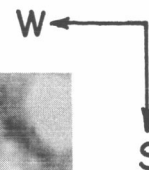
Plate X

LAC 59 MARE VAPORUM

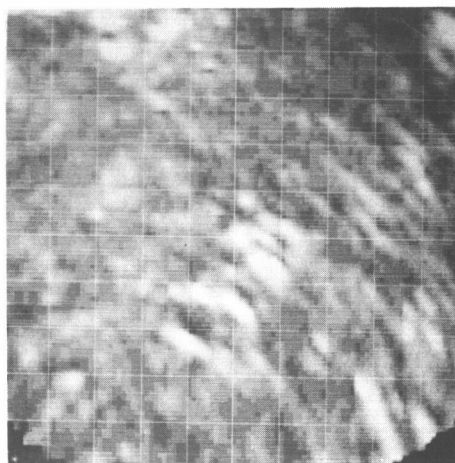
Longitude = -10° , $+10^{\circ}$ Latitude = 0° , 16°

The polarized map shows many specular highlights from ridges tilted toward the radar. The rough area in the northeast is the crater Manilius.

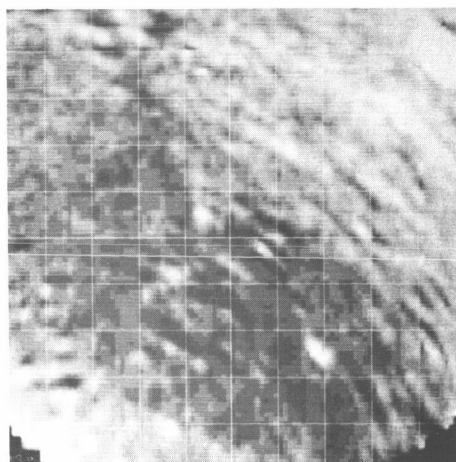
Depolarized



Polarized



Ratio



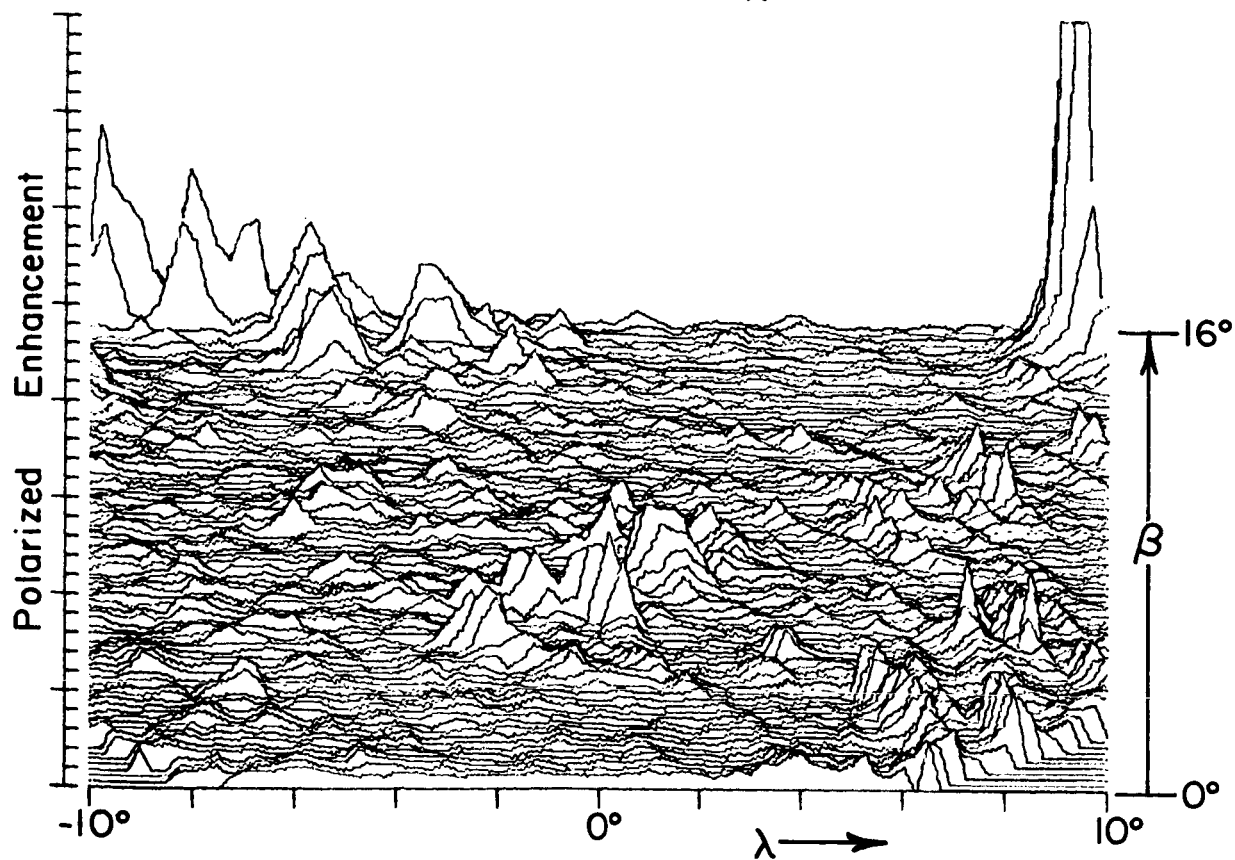
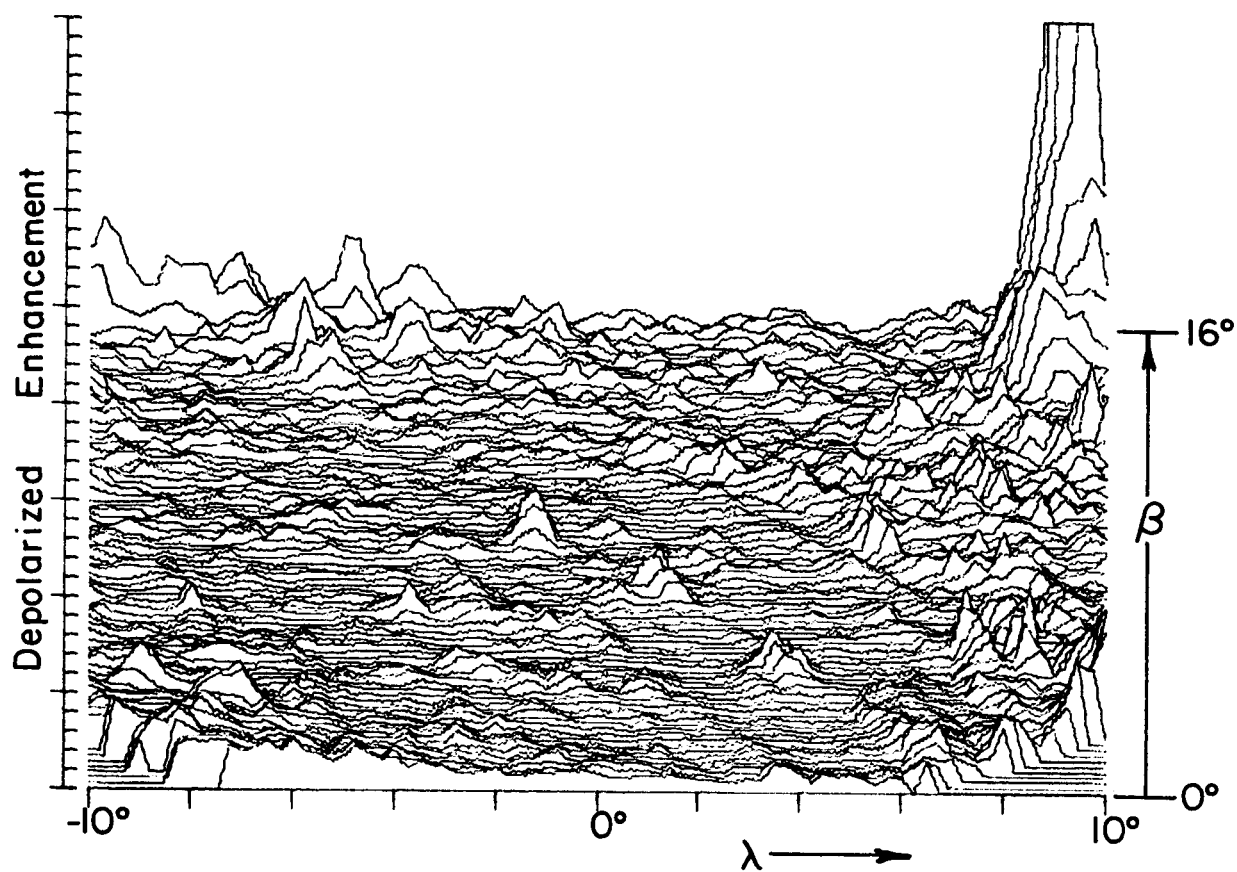


Plate x. Isometric Plot of Radar Map of Plate X,
LAC 59 Mare Vaporum.

Plate XI

LAC 60 JULIUS CAESAR

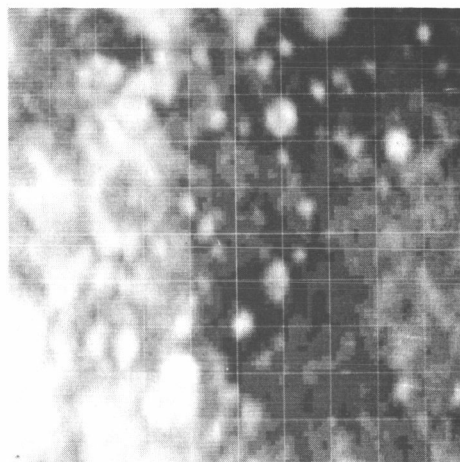
Longitude = 10° , 30°

Latitude = 0° , 16°

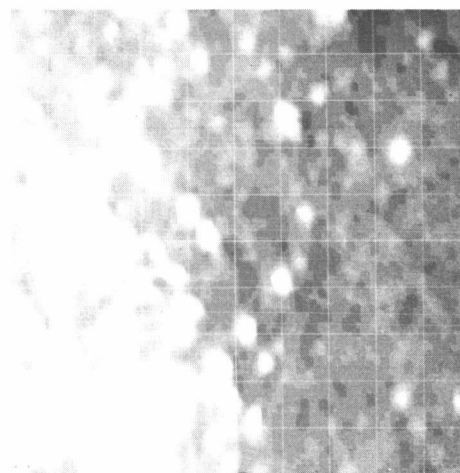
Many craters and ridges in the west showed specular highlights. The ridges in the northwest were particularly well aligned to give specular highlights. Plate XXIX shows the southwest portion of this map observed with a twofold improvement in resolution.

Depolarized

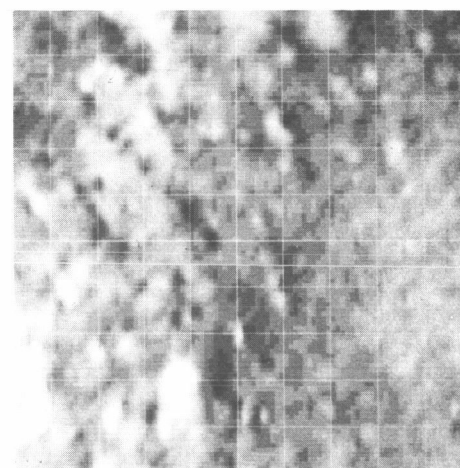
W ←
↓ S



Polarized



Ratio



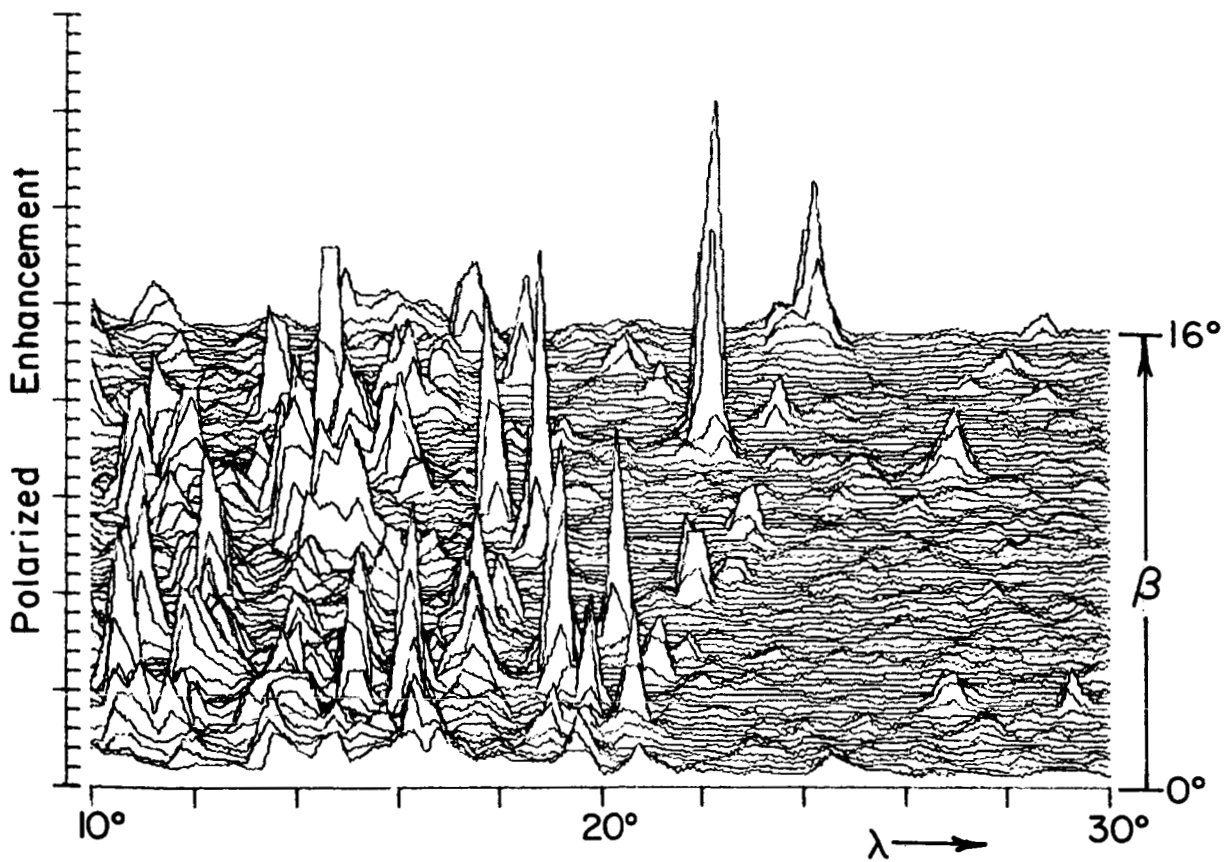
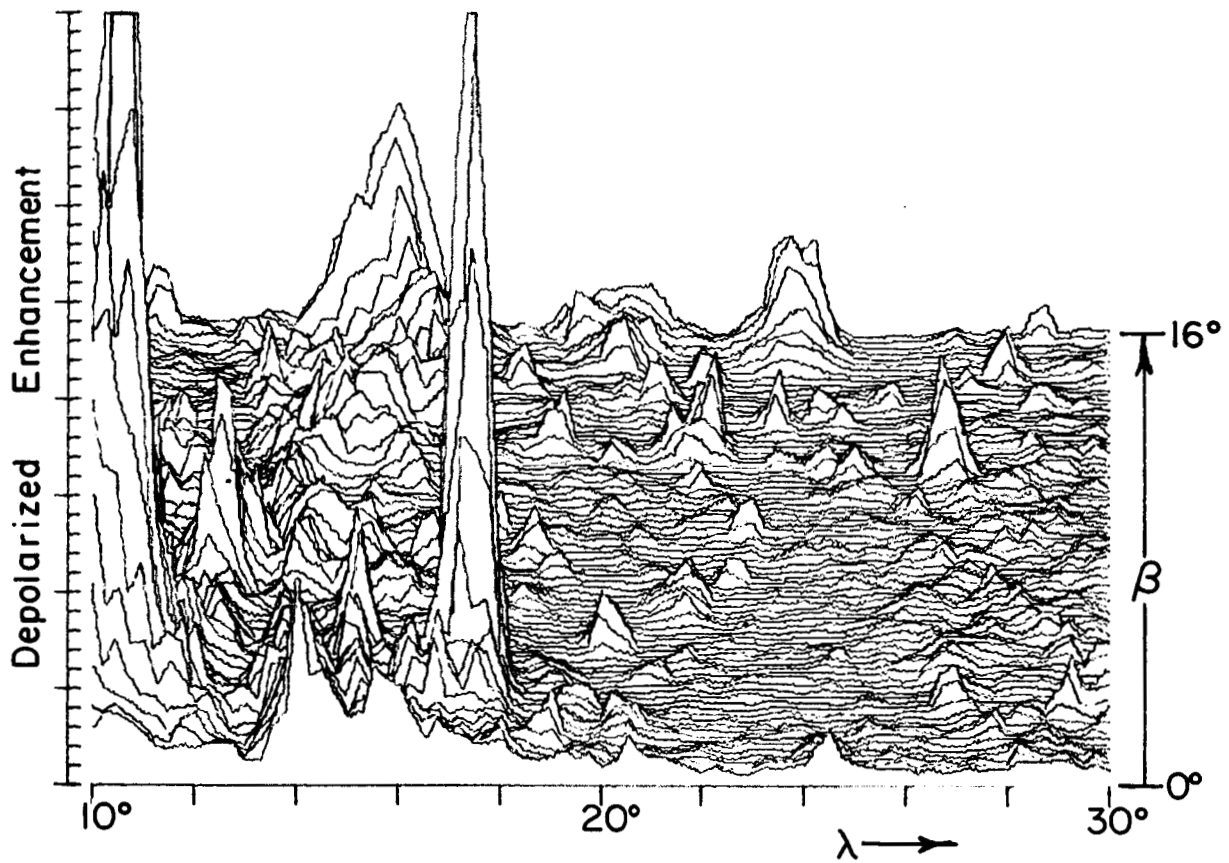


Plate xi. Isometric Plot of Radar Map of Plate XI,
LAC 60 Julius Caesar.

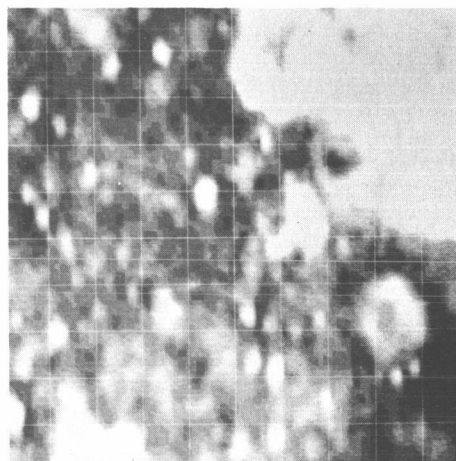
Plate XII

LAC 61 TARUNTIUS

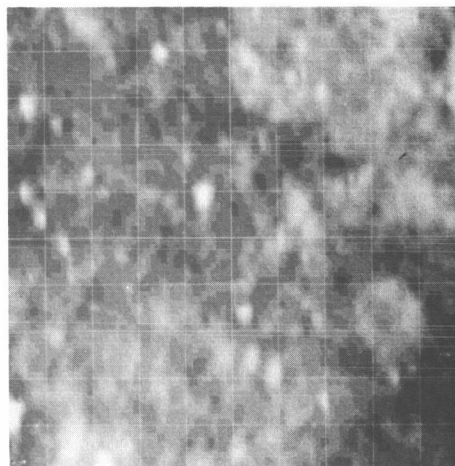
Longitude = 30° , 50° Latitude = 0° , 16°

Palus Somnii, in the northeast, and the Montes Pyrenaei, in the south, were rougher than the adjacent areas of Mare Tranquillitatis. The crater Taruntius, in the east, had a rough floor and an even rougher rim. Many small craters showed enhanced backscattering.

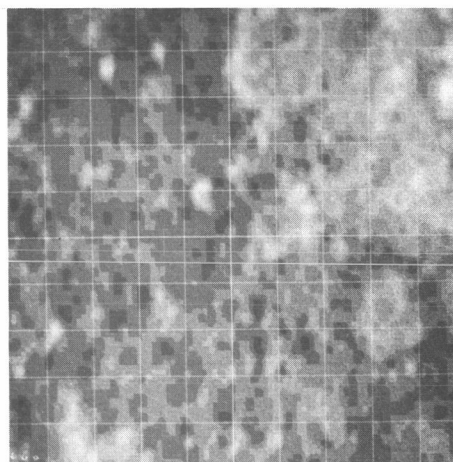
Depolarized



Polarized



Ratio



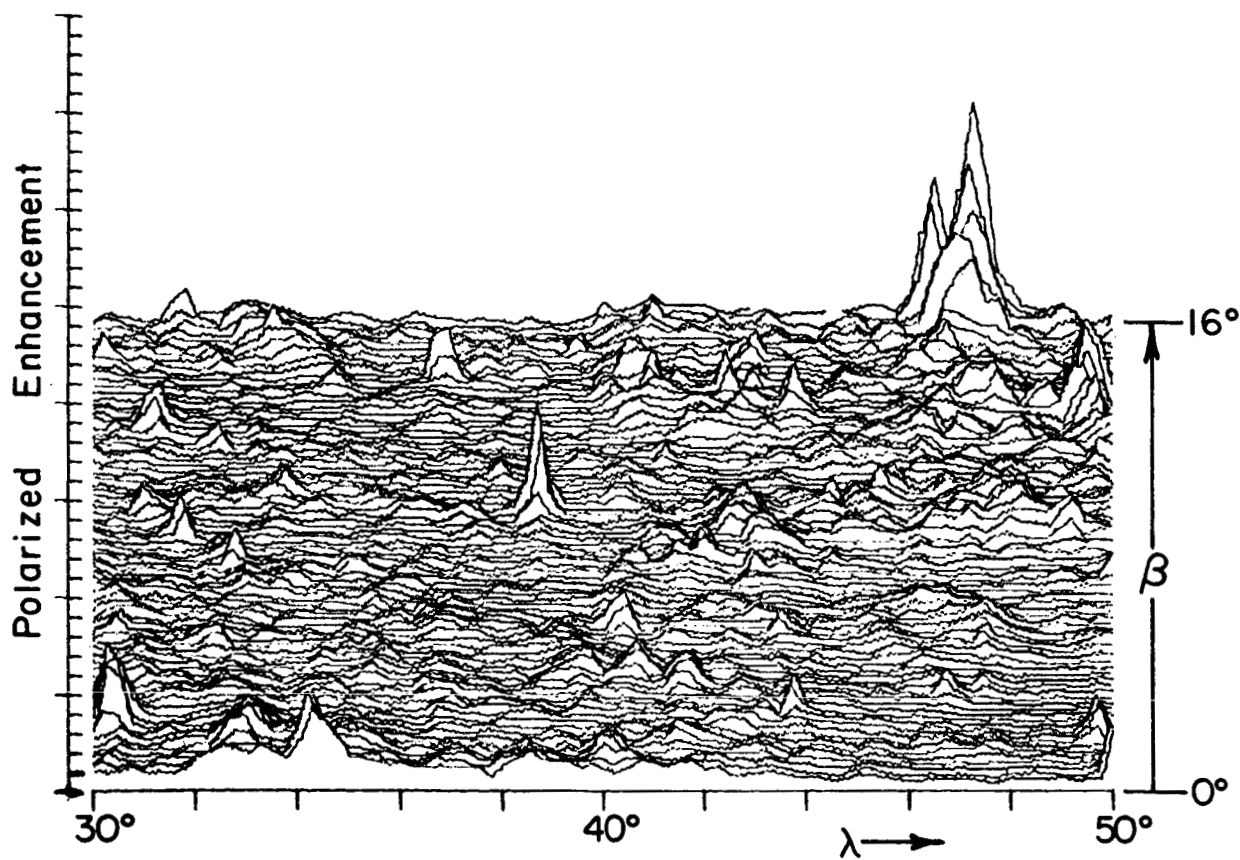
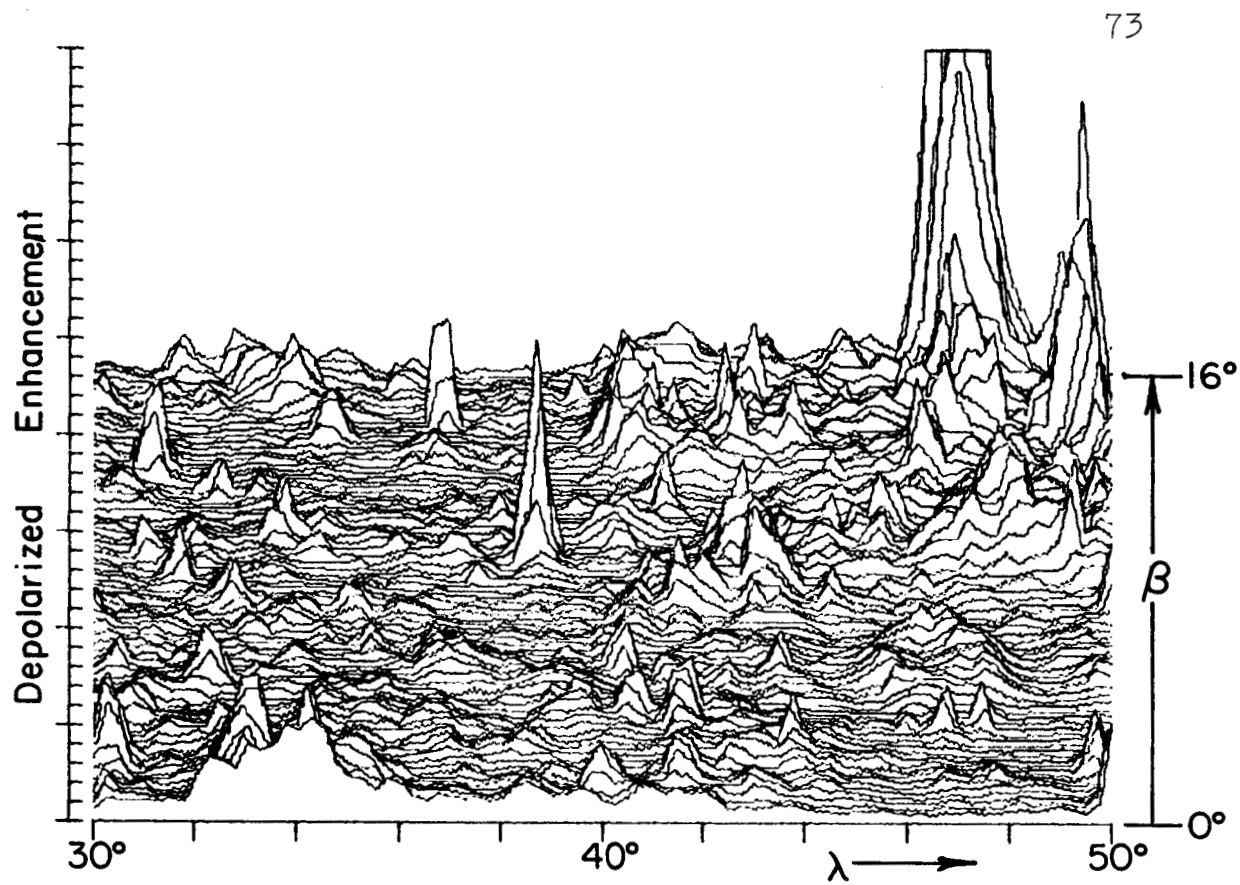


Plate xii. Isometric Plot of Radar Map of Plate XII,
LAC 61 Taruntius.

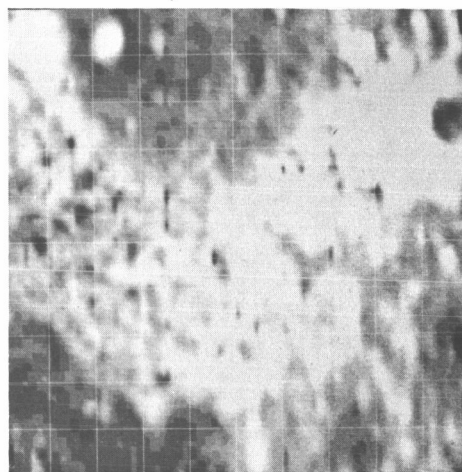
Plate XIII

LAC 62 MARE UNDARUM

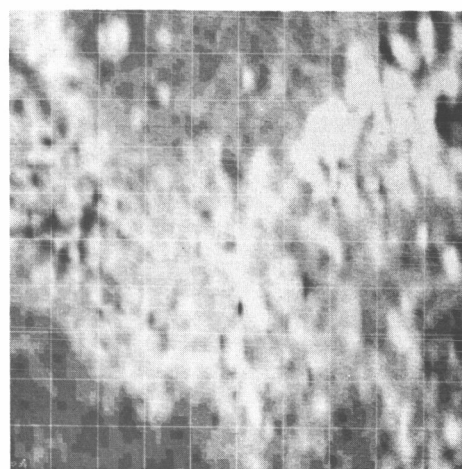
Longitude = 50° , 70° Latitude = 0° , 16°

The highlands between Mare Crisium, in the north, and Mare Fecunditatis, in the southwest, were rougher than the adjacent maria. Some of the slopes in the highlands had specular highlights and appear as the dark spots in the ratio map. The rough area in Mare Crisium is the crater Picard.

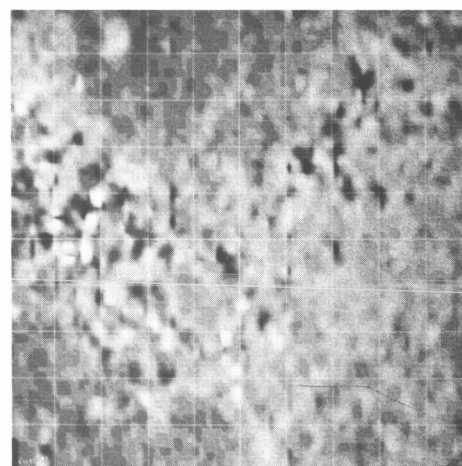
Depolarized



Polarized



Ratio



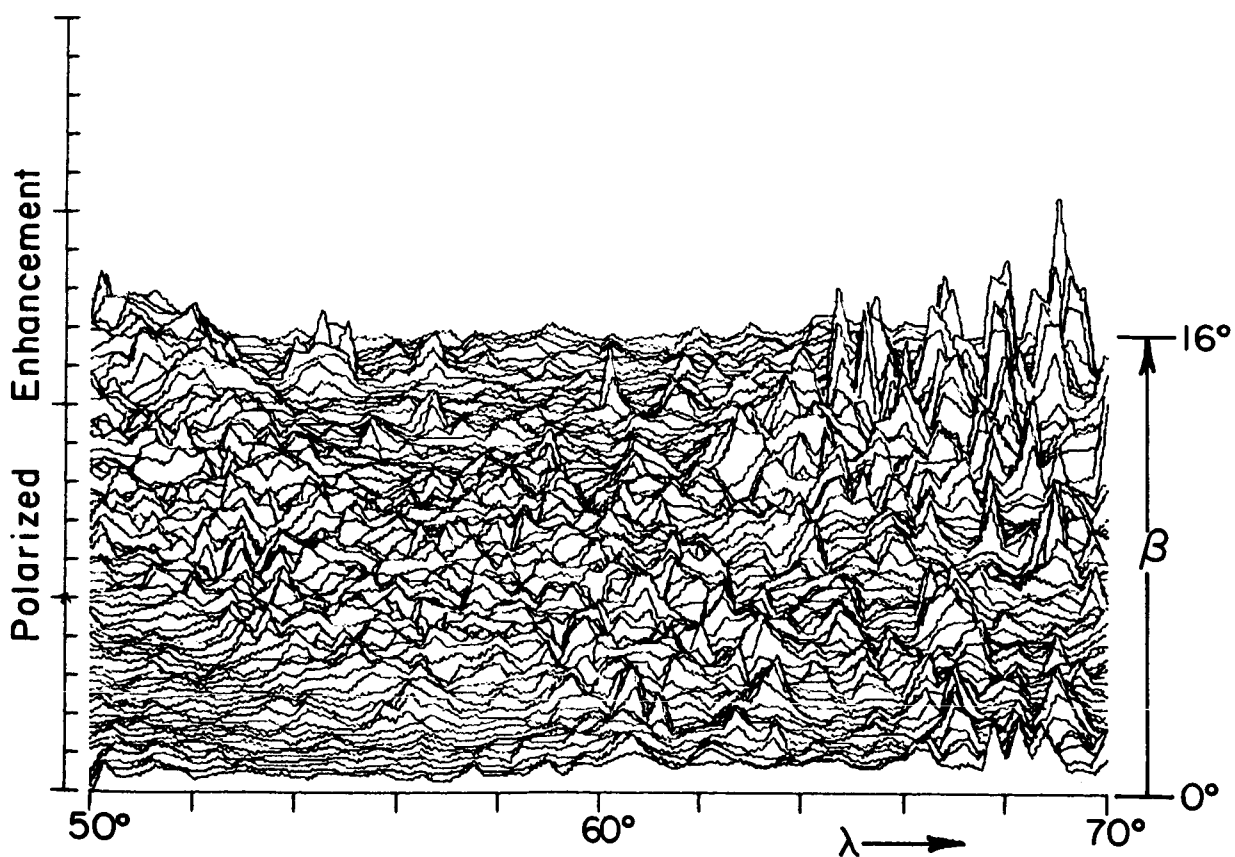
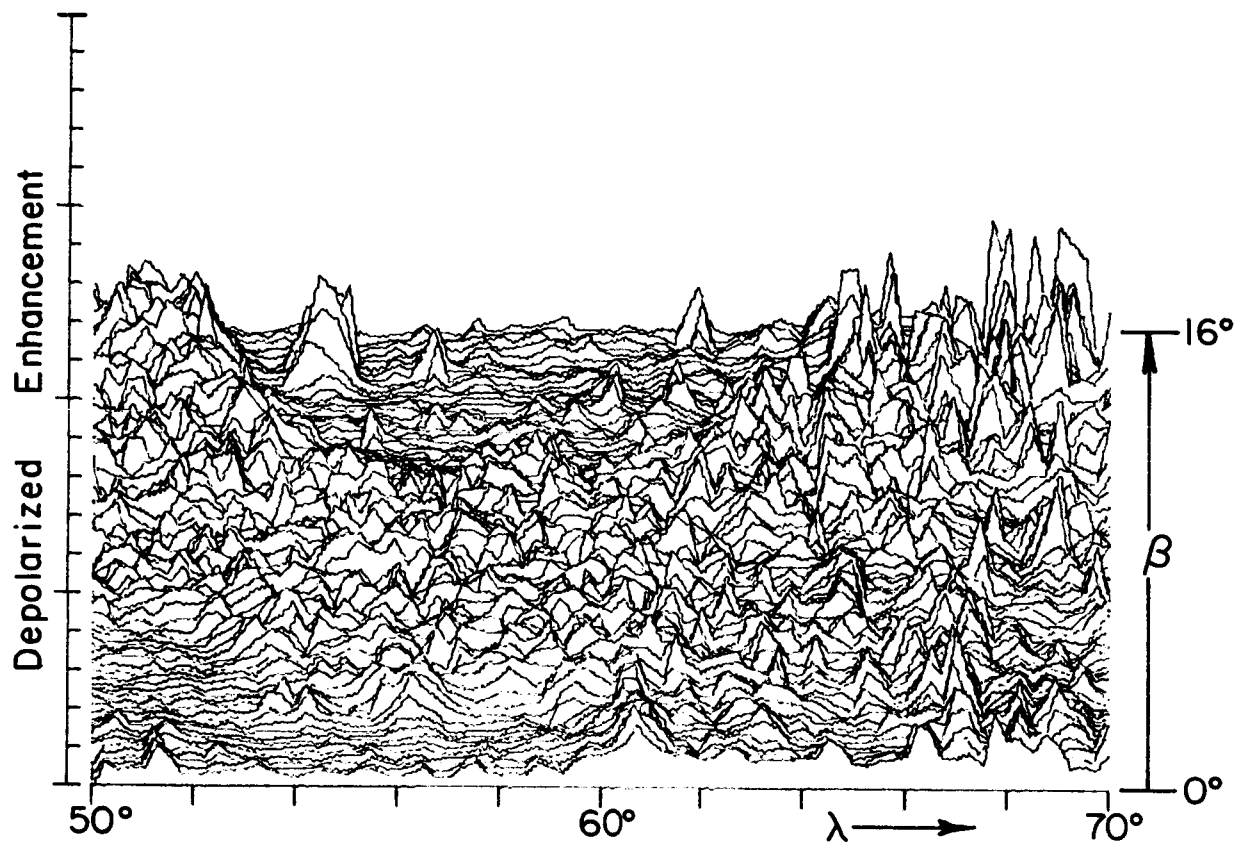


Plate xiii. Isometric Plot of Radar Map of Plate XIII,
LAC 62 Mare Undarum.

Plate XIV

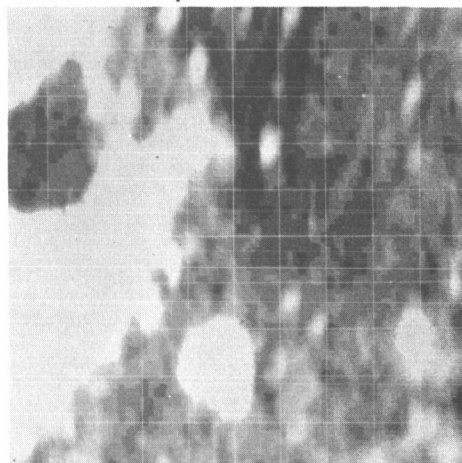
LAC 74 GRIMALDI

Longitude = -70° , -50°

Latitude = -16° , 0°

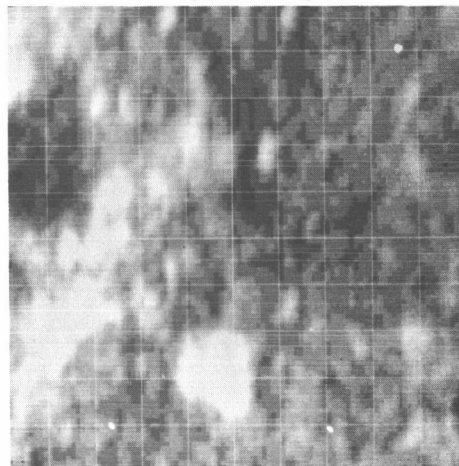
The highlands in the western portion of this map were rougher than the floor of crater Grimaldi and the adjacent areas of Oceanus Procellarum. The craters Sirsalis and Sirsalis A were the rough areas in the south. Several other craters showed enhanced backscattering.

Depolarized

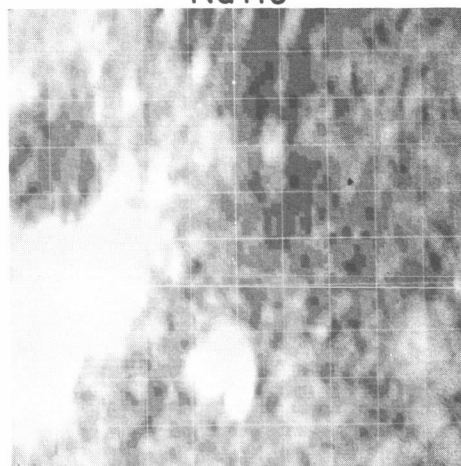


W ←
↓ S

Polarized



Ratio



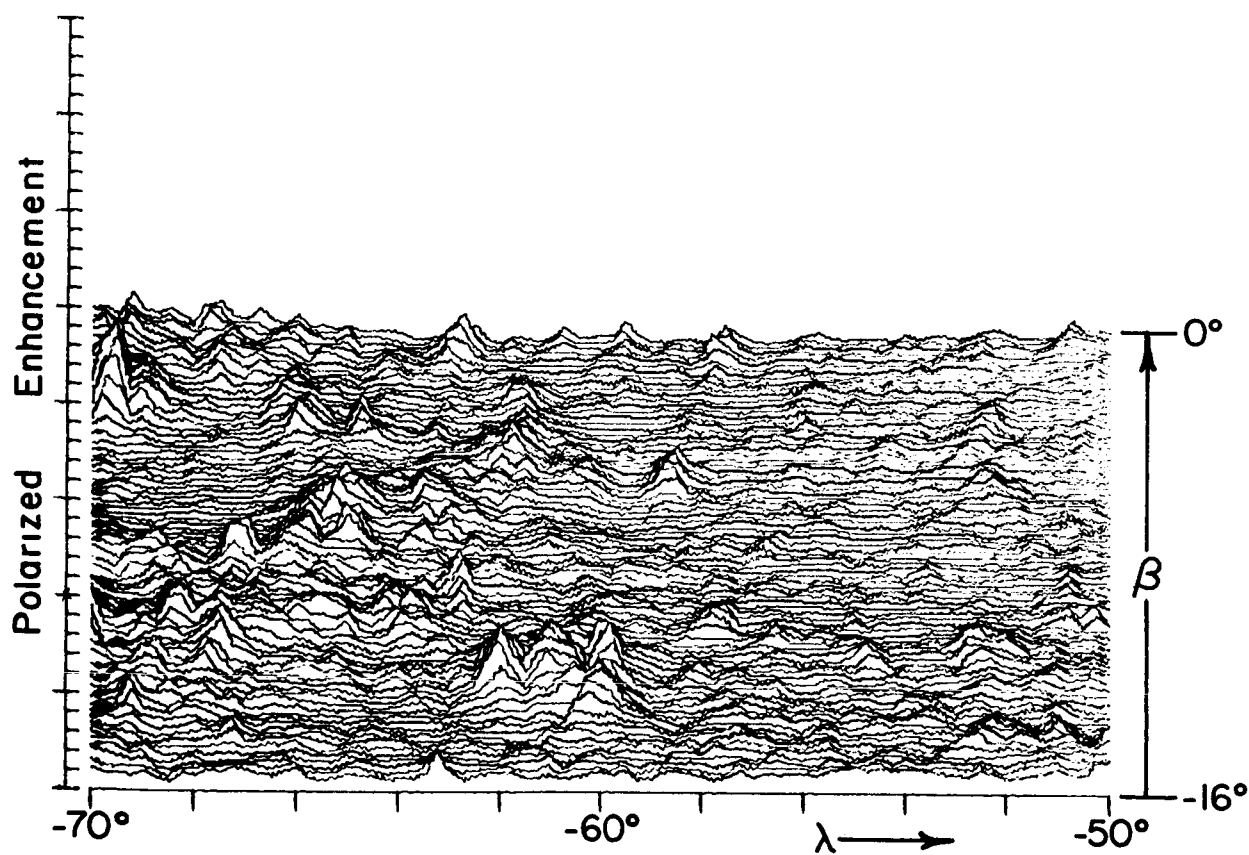
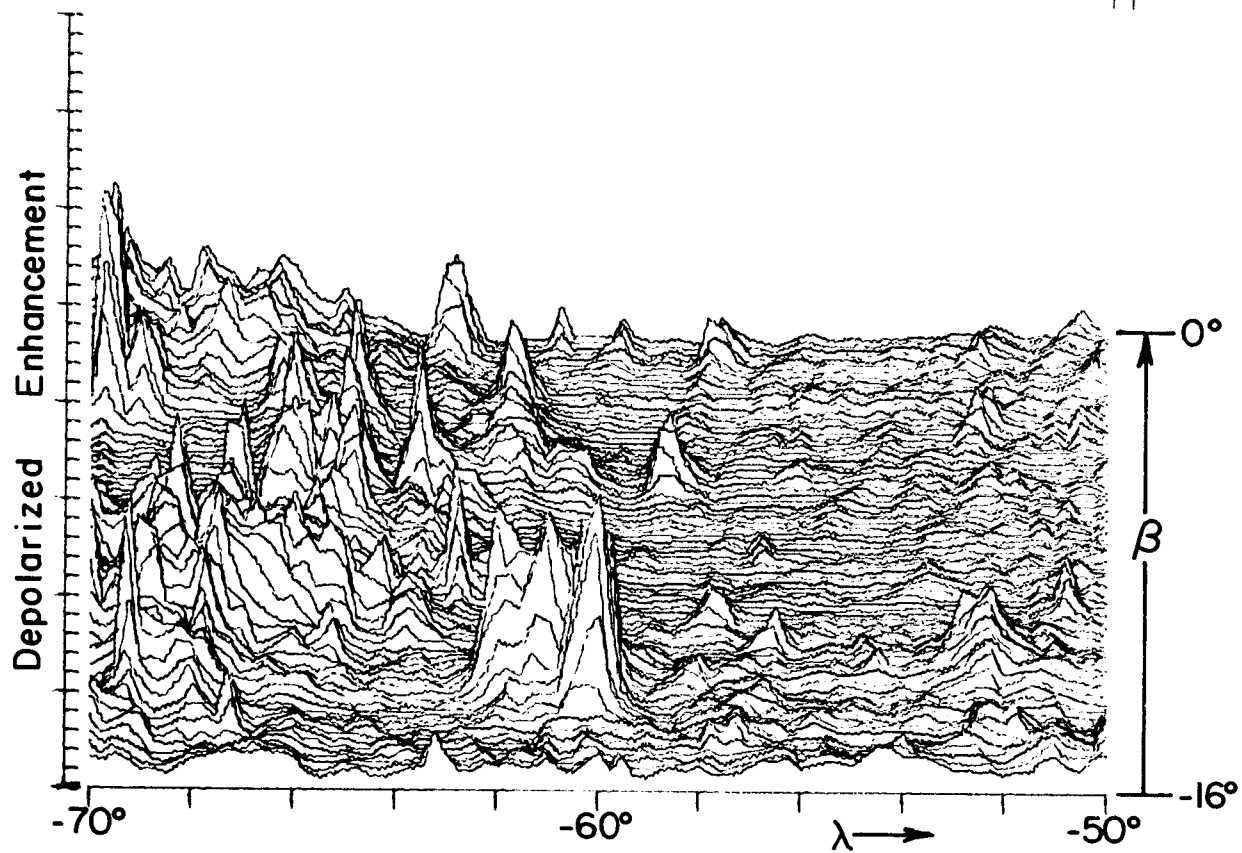


Plate xiv. Isometric Plot of Radar Map of Plate XIV,
LAC 74 Grimaldi.

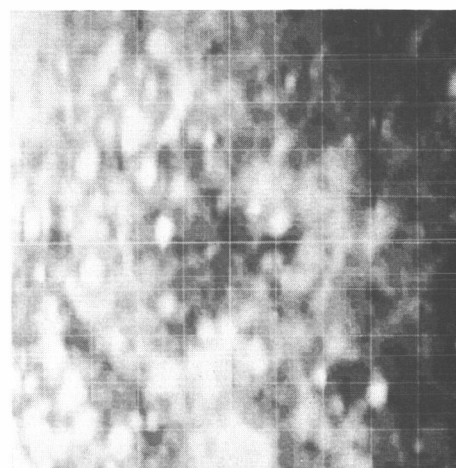
Plate XV

LAC 75 LETRONNE

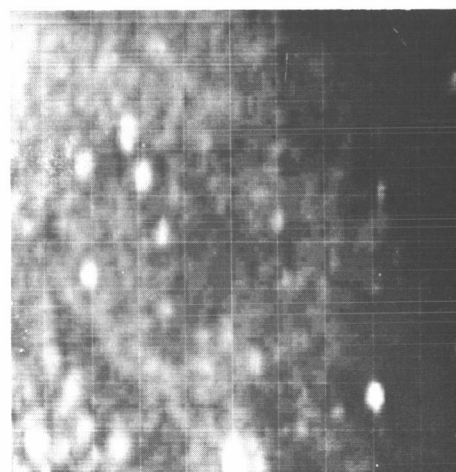
Longitude = -50° , -30° Latitude = -16° , 0°

The Flamsteed ring, in the northwest, the ridges that emerge from Oceanus Procellarum, were rough. Many craters showed enhanced back-scattering. The crater Gassendi A, in the south, was extremely rough. The gradation in reflected power that runs from west to east probably resulted from an antenna-pointing error, which positioned the antenna further west than was intended.

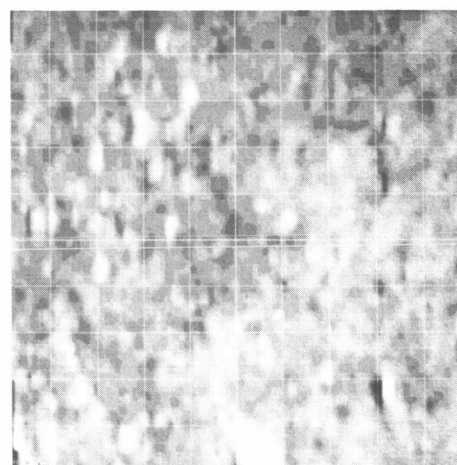
Depolarized



Polarized



Ratio



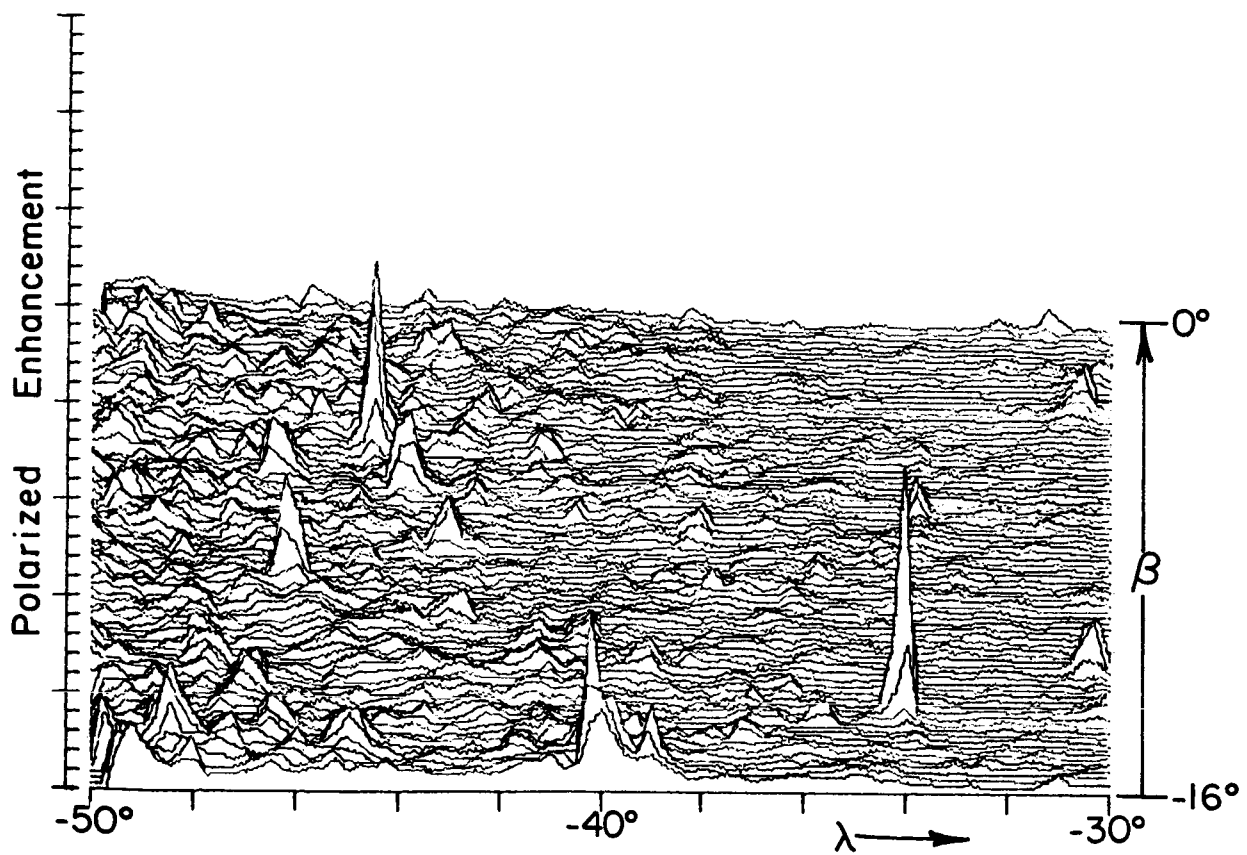
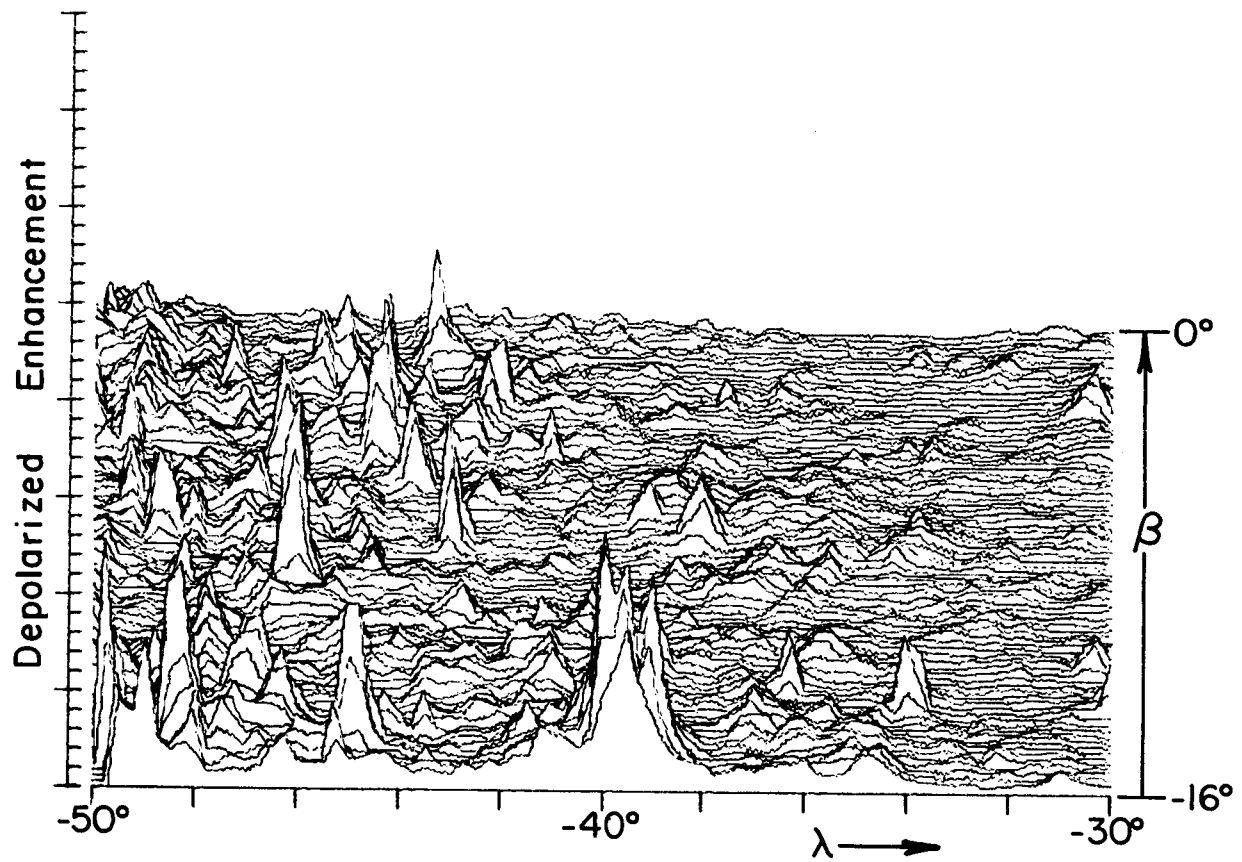


Plate xv. Isometric Plot of Radar Map of Plate XV,
LAC 75 Letronne.

Plate XVI

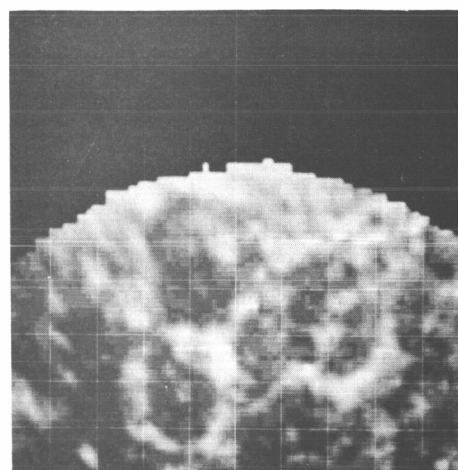
LAC 77 PTOLEMAEUS

Longitude = -10° , $+10^{\circ}$

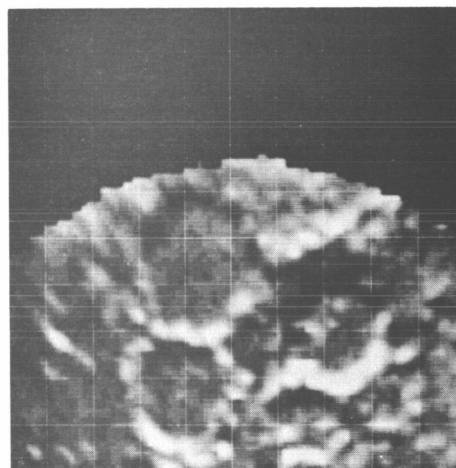
Latitude = -16° , 0°

The far (south) rims of the large craters Ptolemaeus, Alphonsus, and Albategnius showed specular highlights, which make the polarized map resemble an optical photograph; however, the rims of these craters were rougher than their floors. The northern portion of the map was deleted because the antenna beam was pointed to the south to discriminate against conjugate reflecting areas.

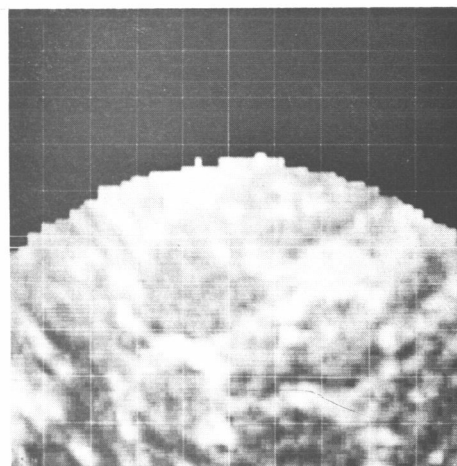
Depolarized



Polarized



Ratio



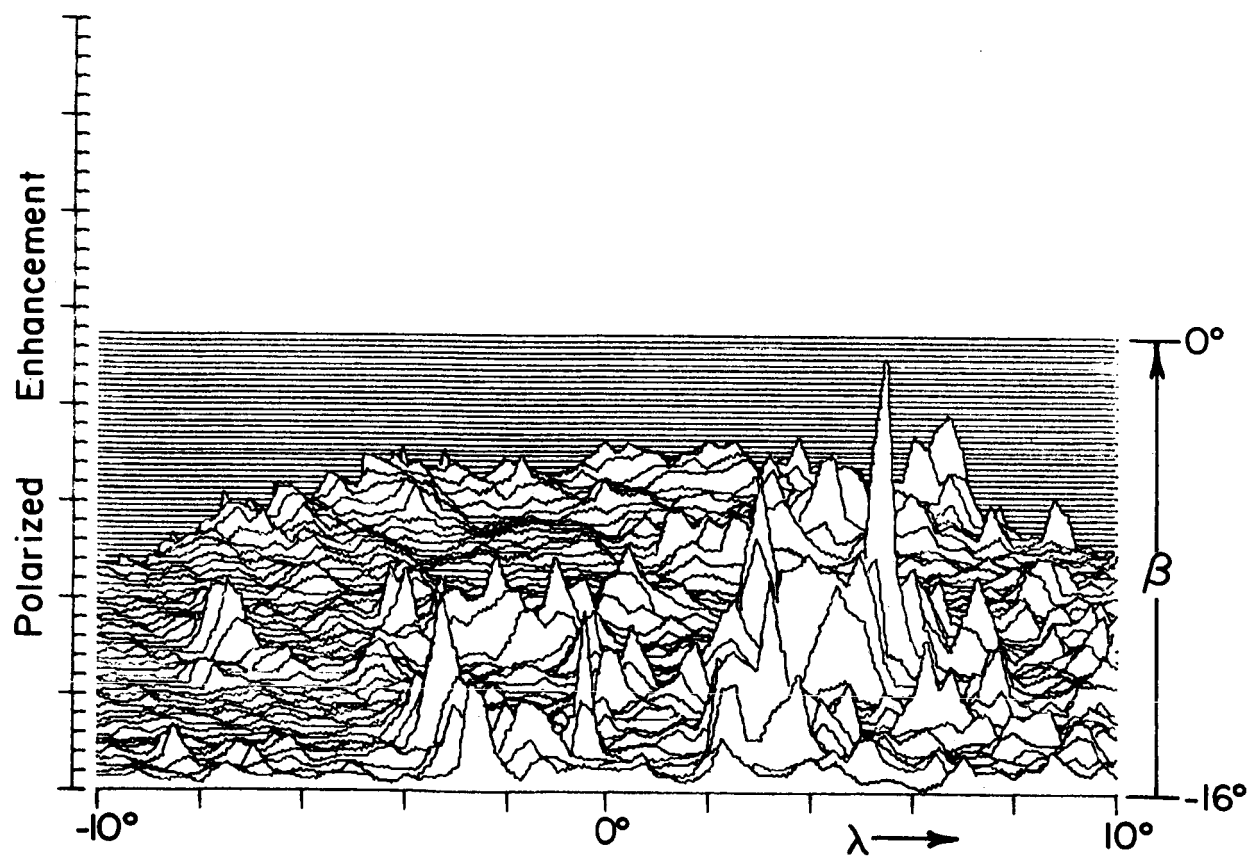
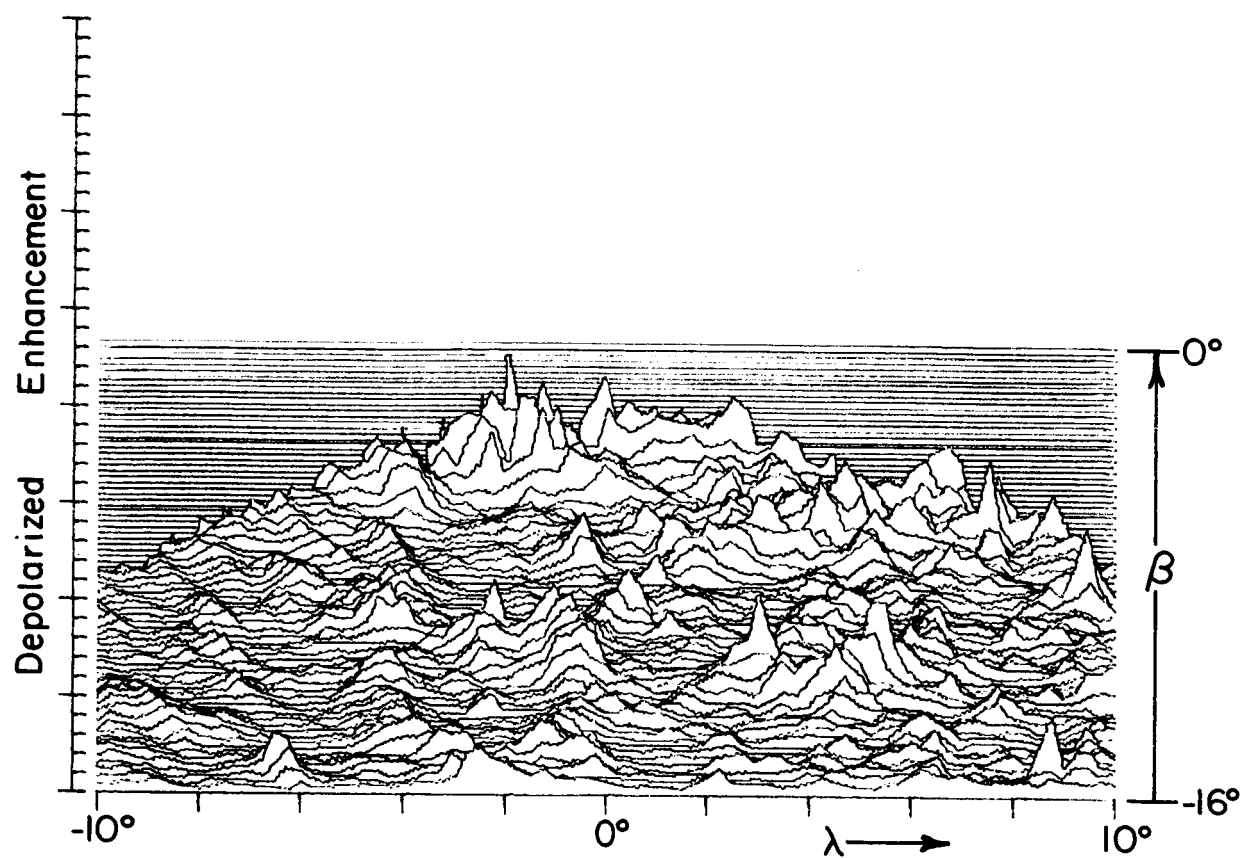


Plate xvi. Isometric Plot of Radar Map of Plate XVI,
LAC 77 Ptolemaeus.

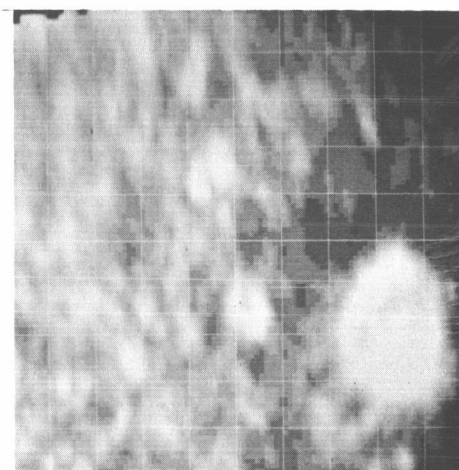
Plate XVII

LAC 78 THEOPHILUS

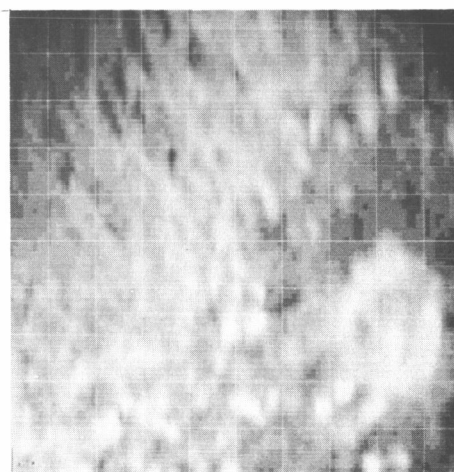
Longitude = 10° , 30° Latitude = -16° , 0°

The rough area in the southeast is the large rayed crater Theophilus. Some difference in roughness is apparent in the northeast between the highlands and the adjacent areas of Mare Tranquillitatis. The apparent roughness in the northwest corner of the map may be an error. This area was observed near the libration equator, where inadequate discrimination against reflections of the conjugate reflecting areas may have occurred. The eastern portion of this map was observed with a twofold improvement in resolution, and is shown in Plate XXIX.

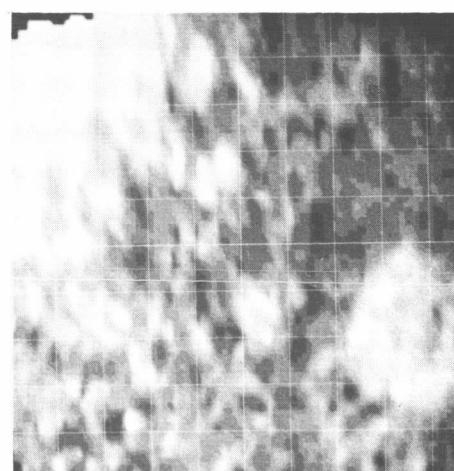
Depolarized



Polarized



Ratio



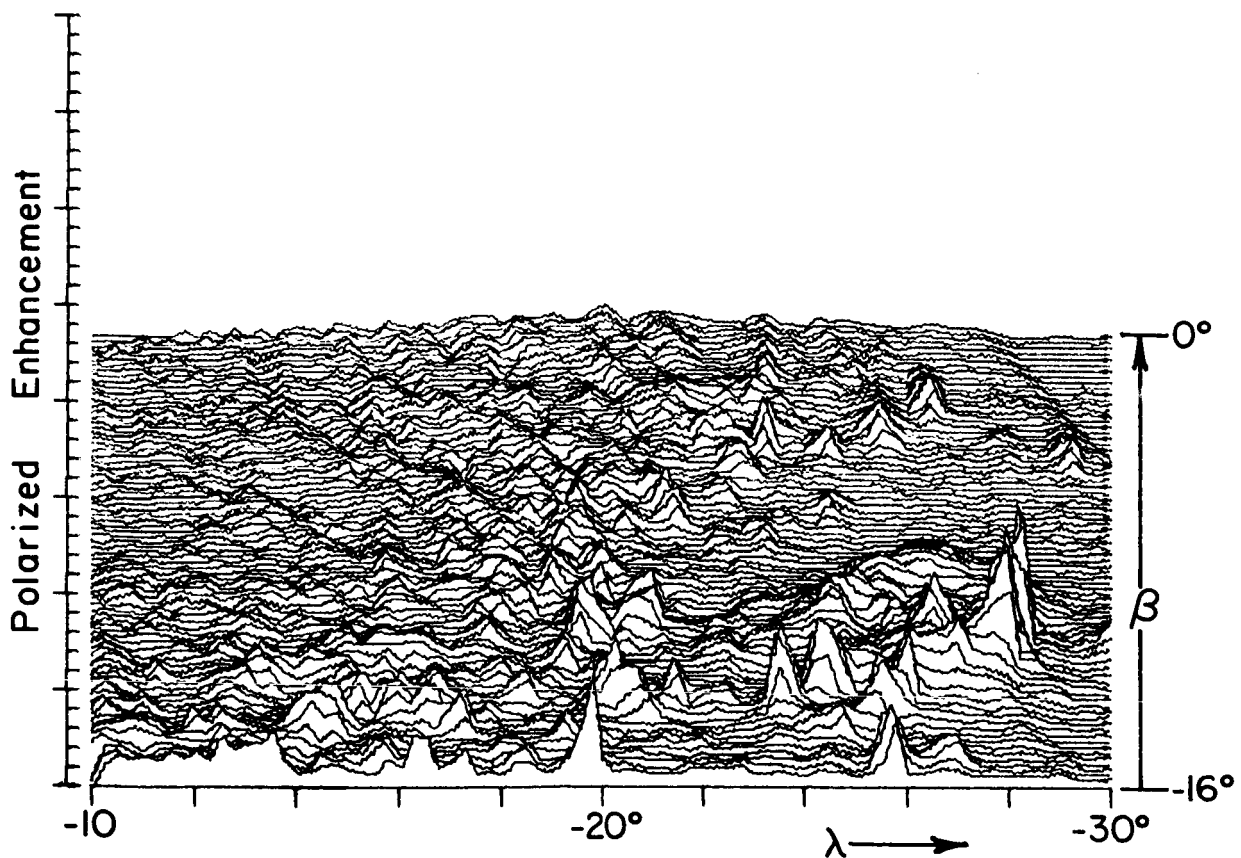
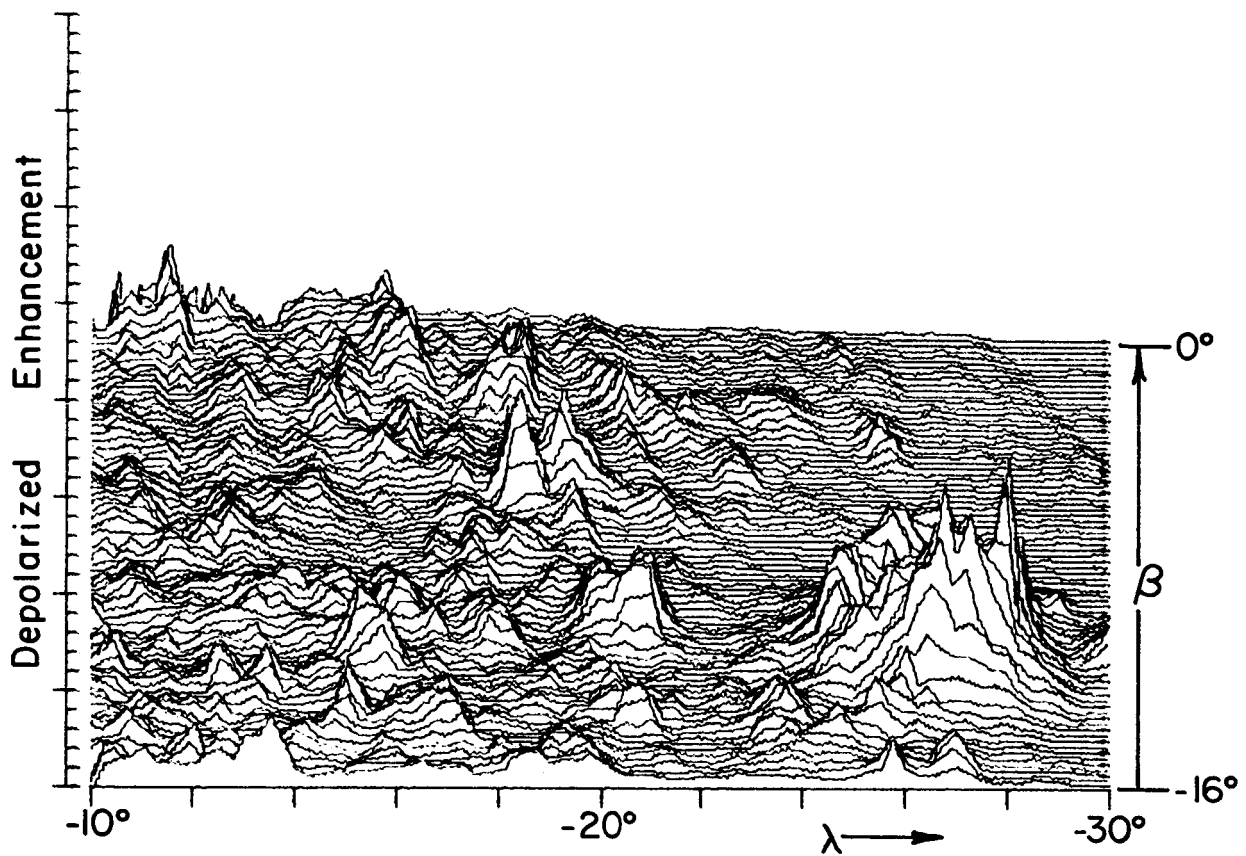


Plate xvii. Isometric Plot of Radar Map of Plate XVII,
LAC 78 Theophilus.

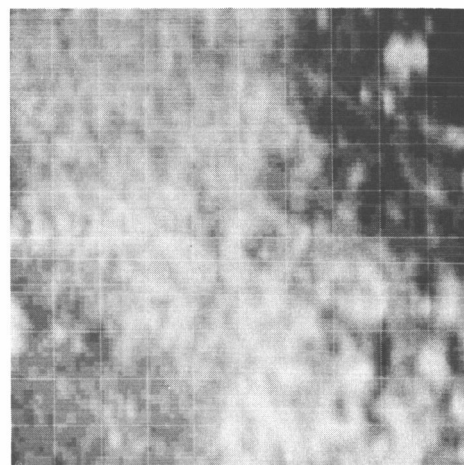
Plate XVIII

LAC 79 COLOMBO

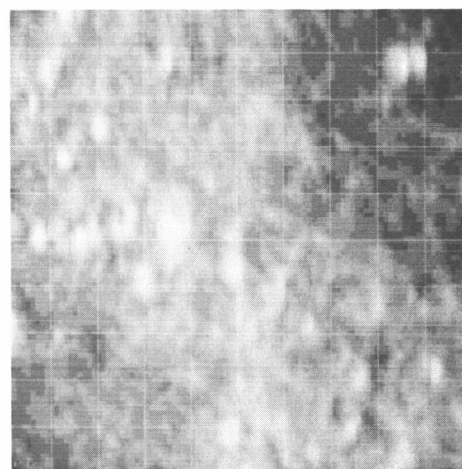
Longitude = 30° , 50° Latitude = -16° , 0°

The Montes Pyrenaei (center), were rougher than Mare Fecunditatis, in the northeast, and Mare Nectaris, in the southwest. Several craters showed specular highlights.

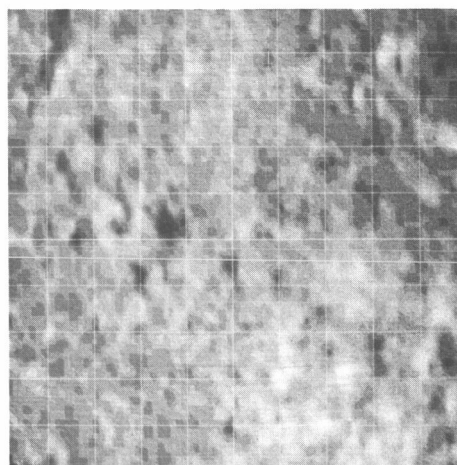
Depolarized



Polarized



Ratio



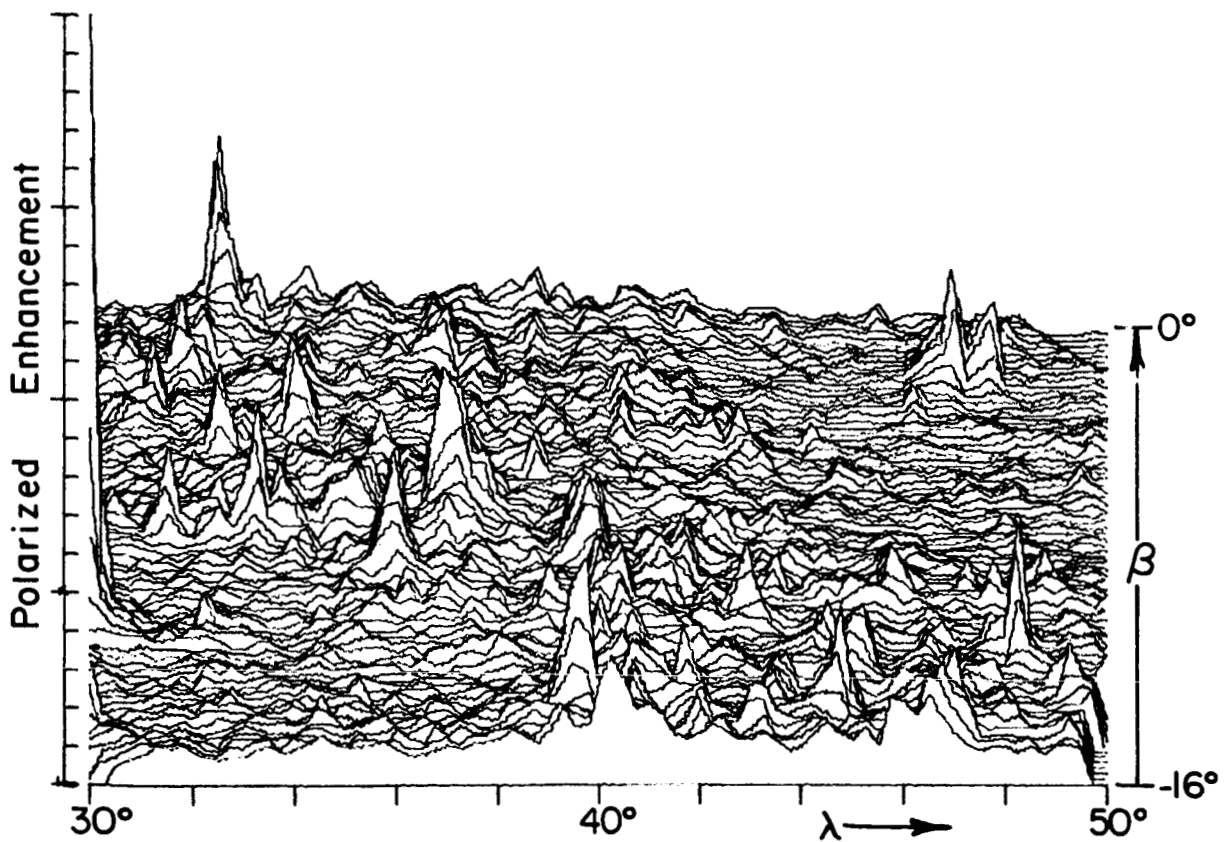
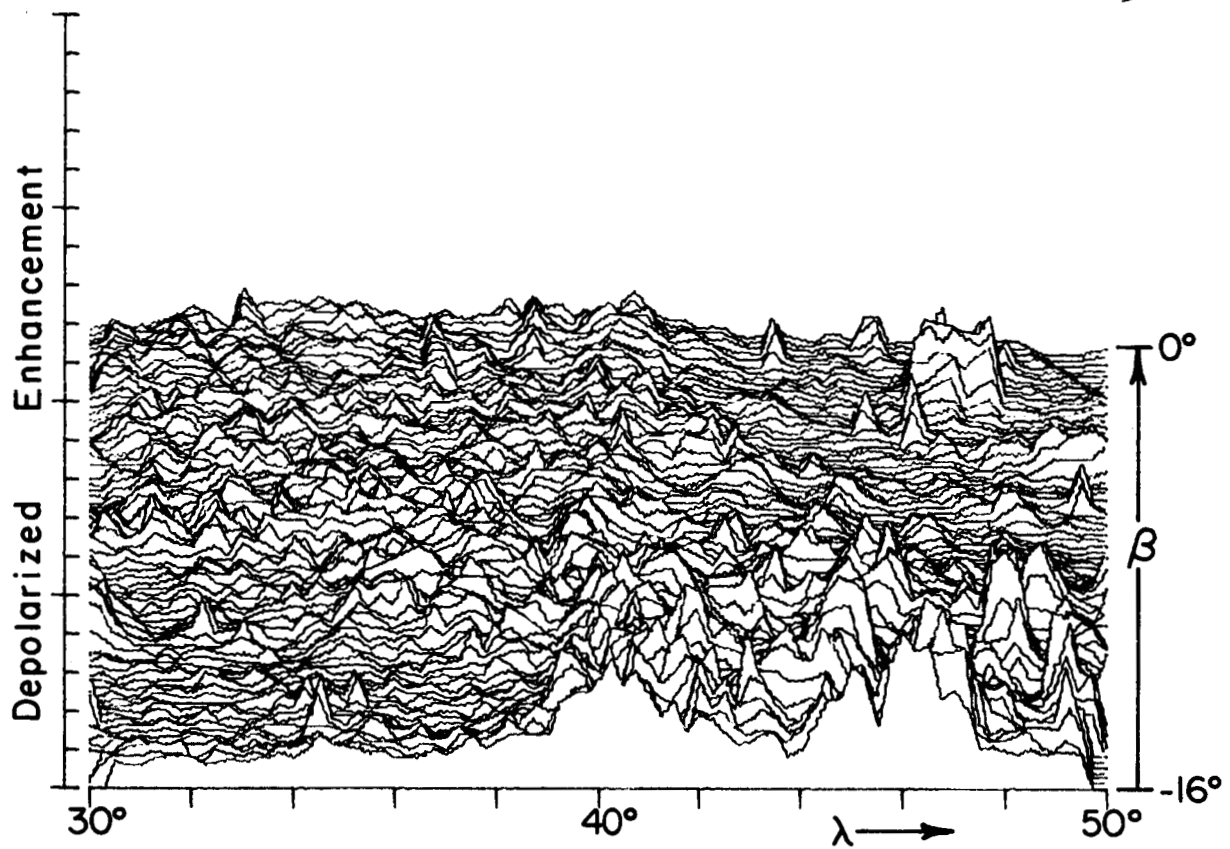


Plate xviii. Isometric Plot of Radar Map of Plate XVIII,
IAC 79 Colombo.

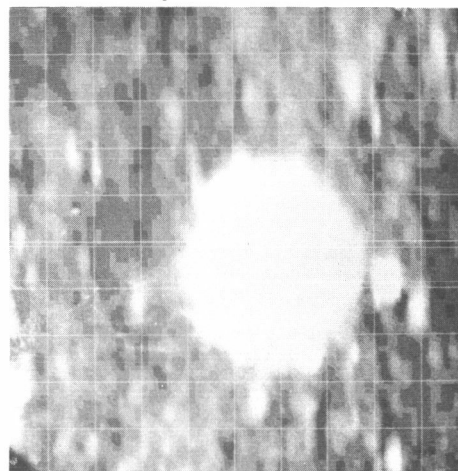
Plate XIX

LAC 80 LANGRENUS

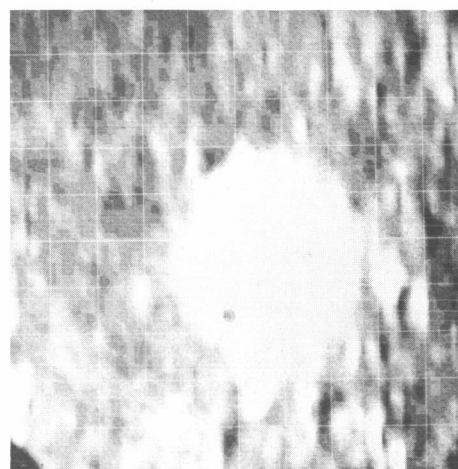
Longitude = 50° , 70° Latitude = -16° , 0°

The extremely rough area in the center of this map is the large rayed crater Langrenus. Several other craters showed backscattering enhancements, which were identified as rough surfaces. Another observation of this area is shown in Plate XXXIV.

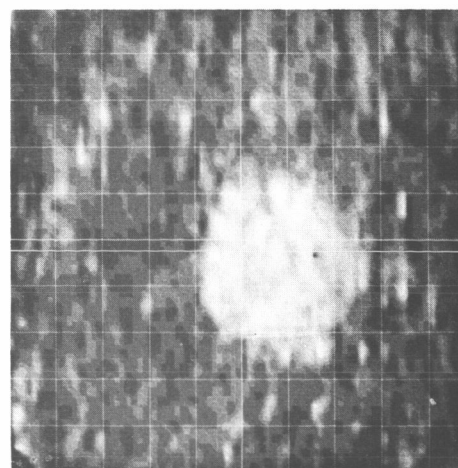
Depolarized



Polarized



Ratio



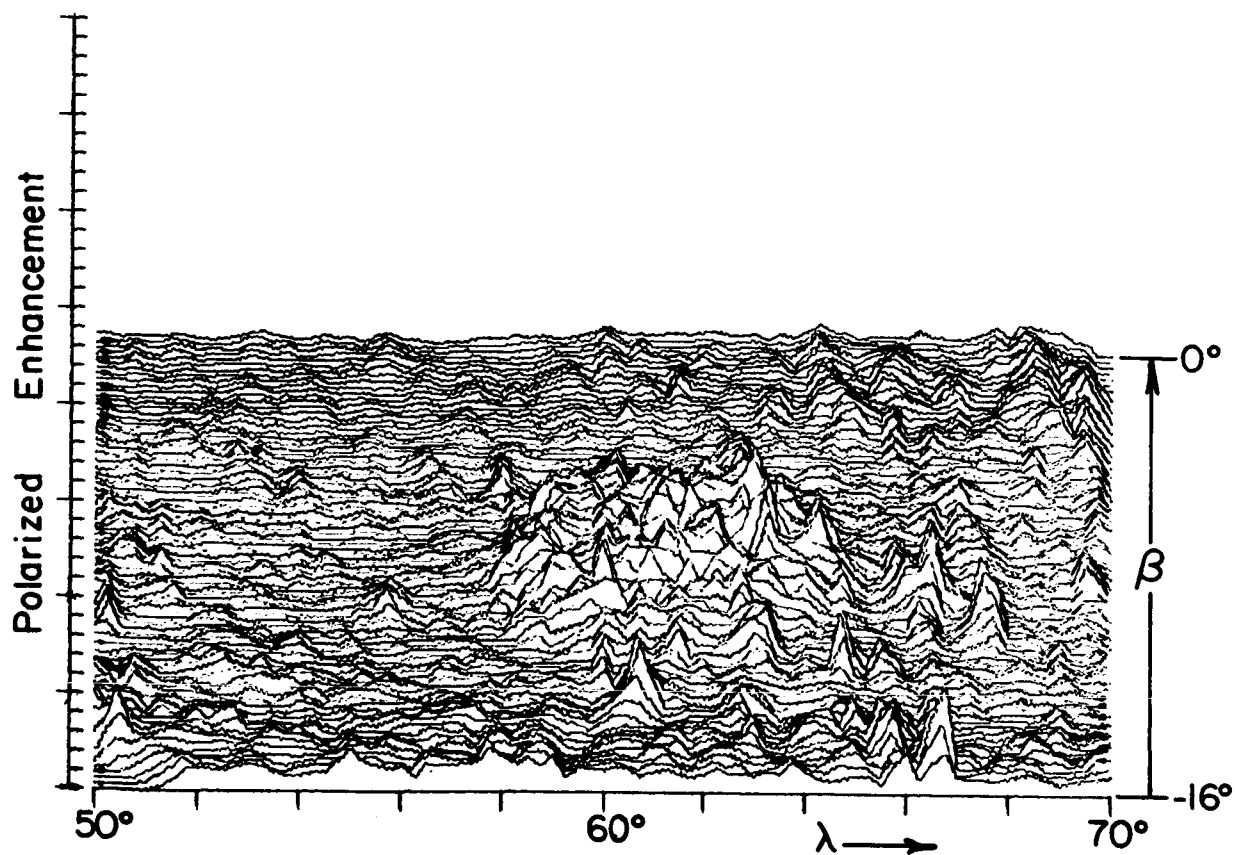
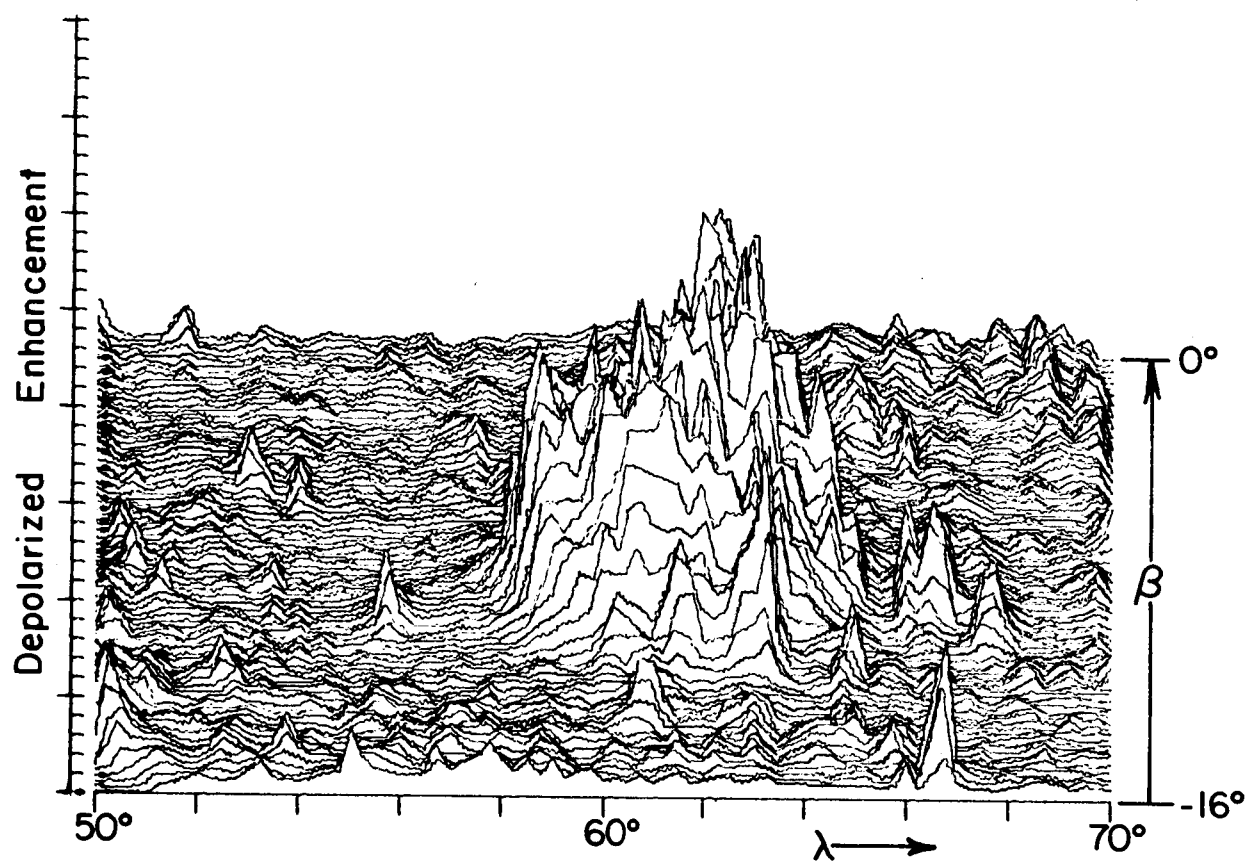


Plate xix. Isometric Plot of Radar Map of Plate XIX,
LAC 80 Langrenus.

Plate XX

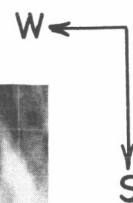
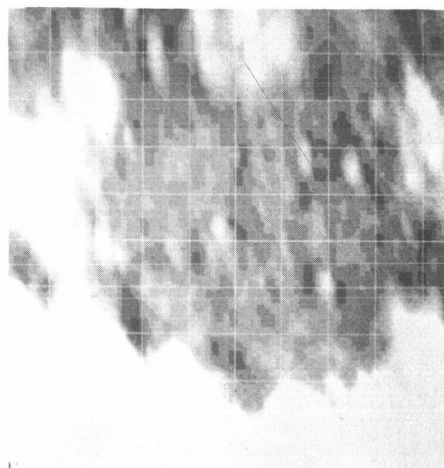
LAC 93 MARE HUMORUM

Longitude = -50° , -30° Latitude = -32° , -16°

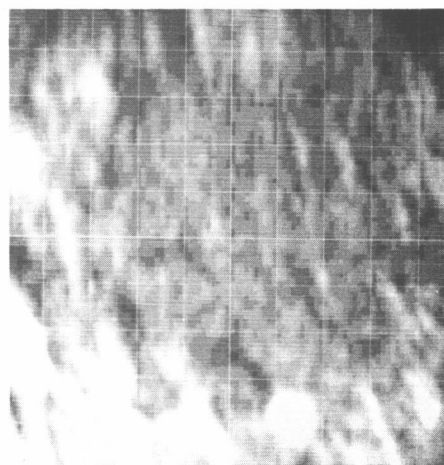
Mare Humorum

(center) was smoother than its environs. The craters Gassendi (north) and Vitello (south) were moderately rough. The smearing of echoes along contours of constant delay probably resulted from an error in the compensation for the Doppler frequency.

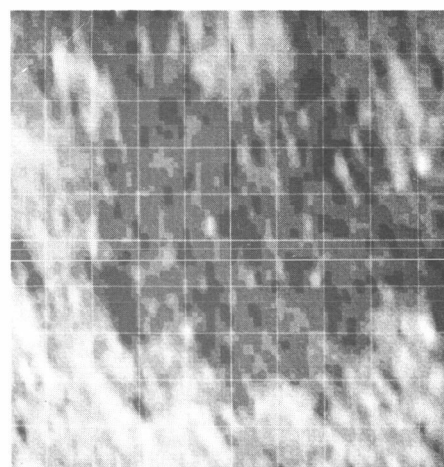
Depolarized



Polarized



Ratio



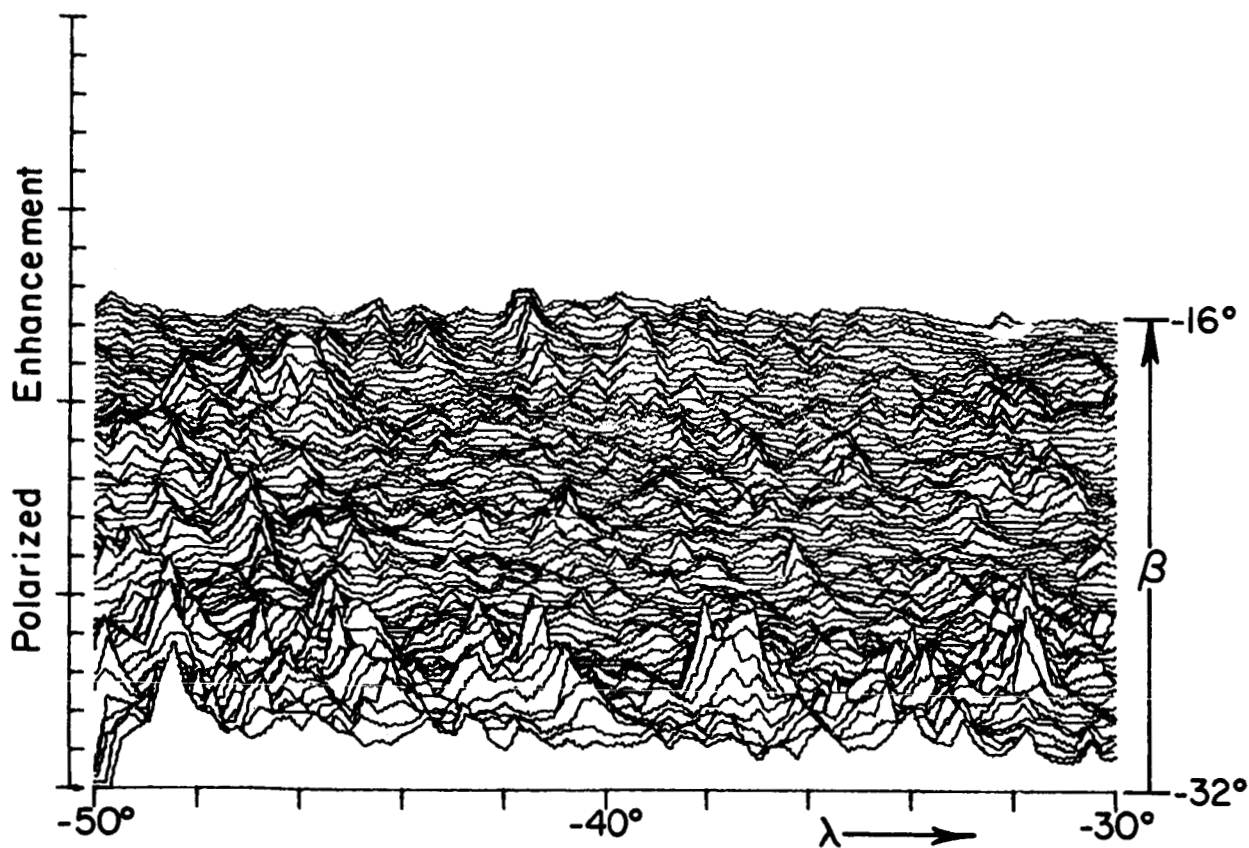
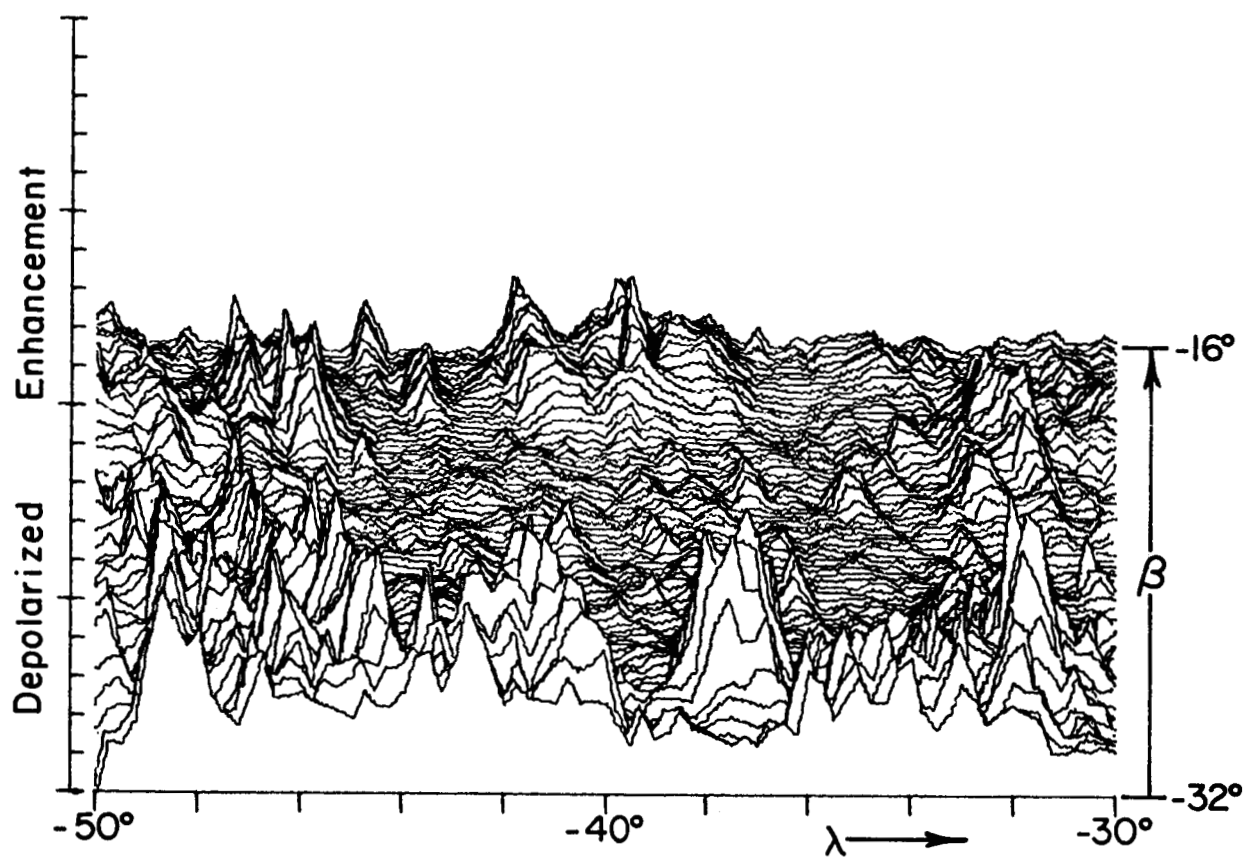


Plate xx. Isometric Plot of Radar Map of Plate XX,
LAC 93 Mare Humorum.

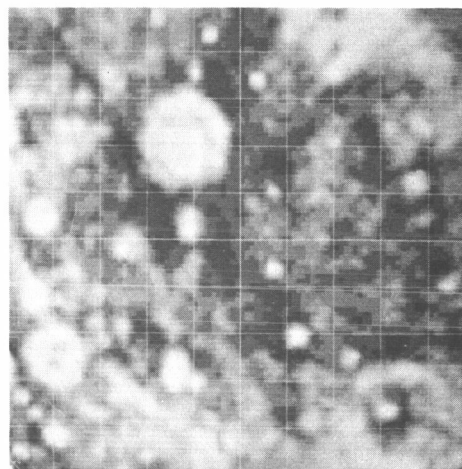
Plate XXI

LAC 94 PITATUS

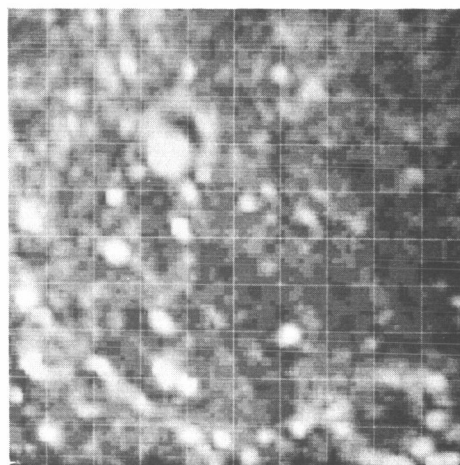
Longitude = -30° , -10° Latitude = -32° , -16°

The craters Campanus and Campanus A (south-west), Bullialdus (northwest), and Agatharchides A (west) appeared as rough areas. The crater Pitatus (south-east) showed only a rough rim. Many specular highlights from small craters are seen in the polarized map. The depolarized returns in the northeast were affected by leakage of strong polarized echoes from conjugate reflecting areas.

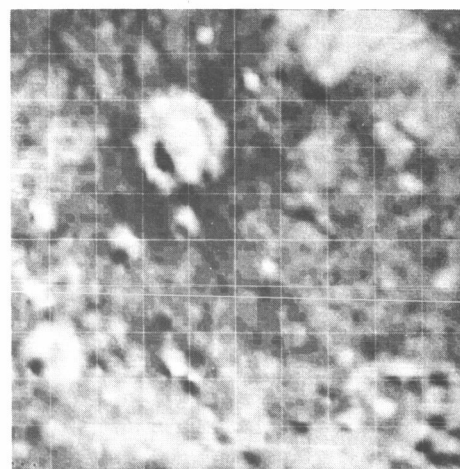
Depolarized



Polarized



Ratio



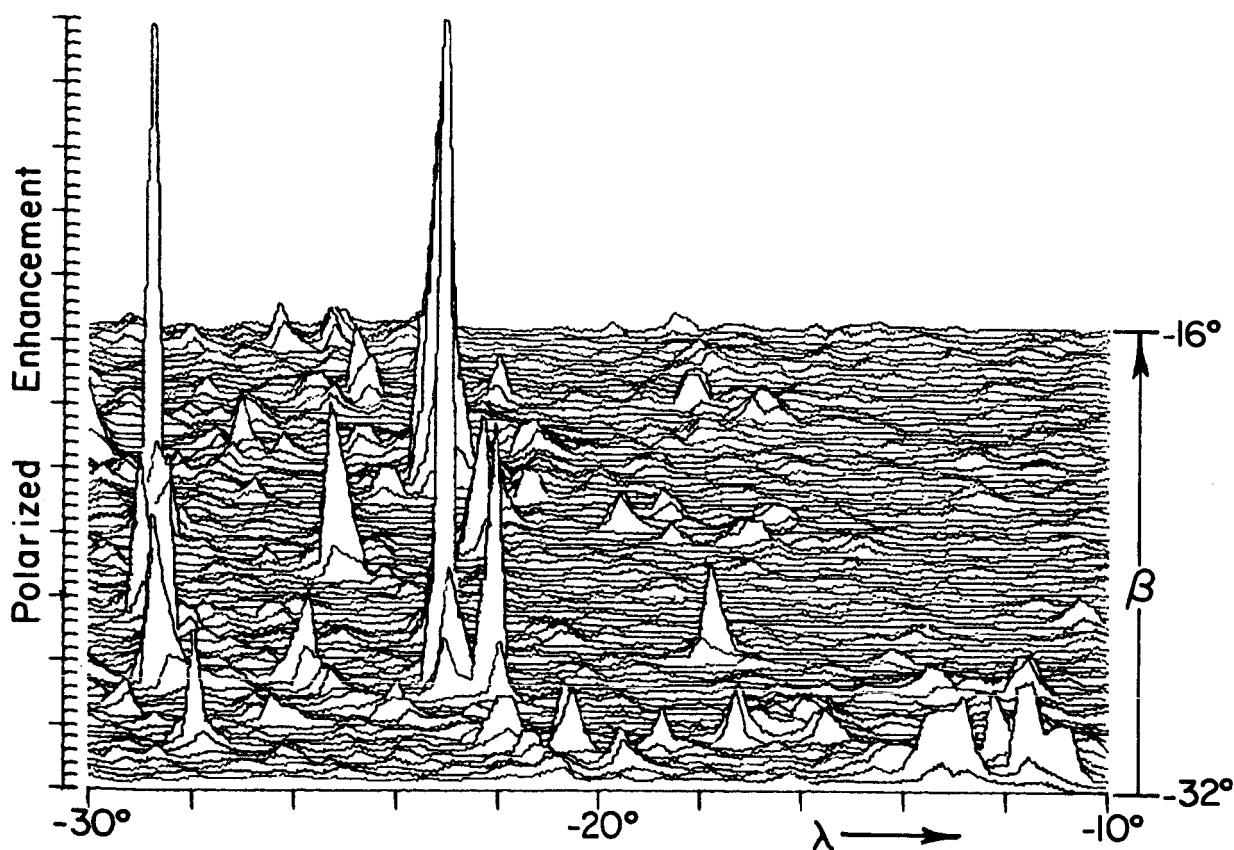
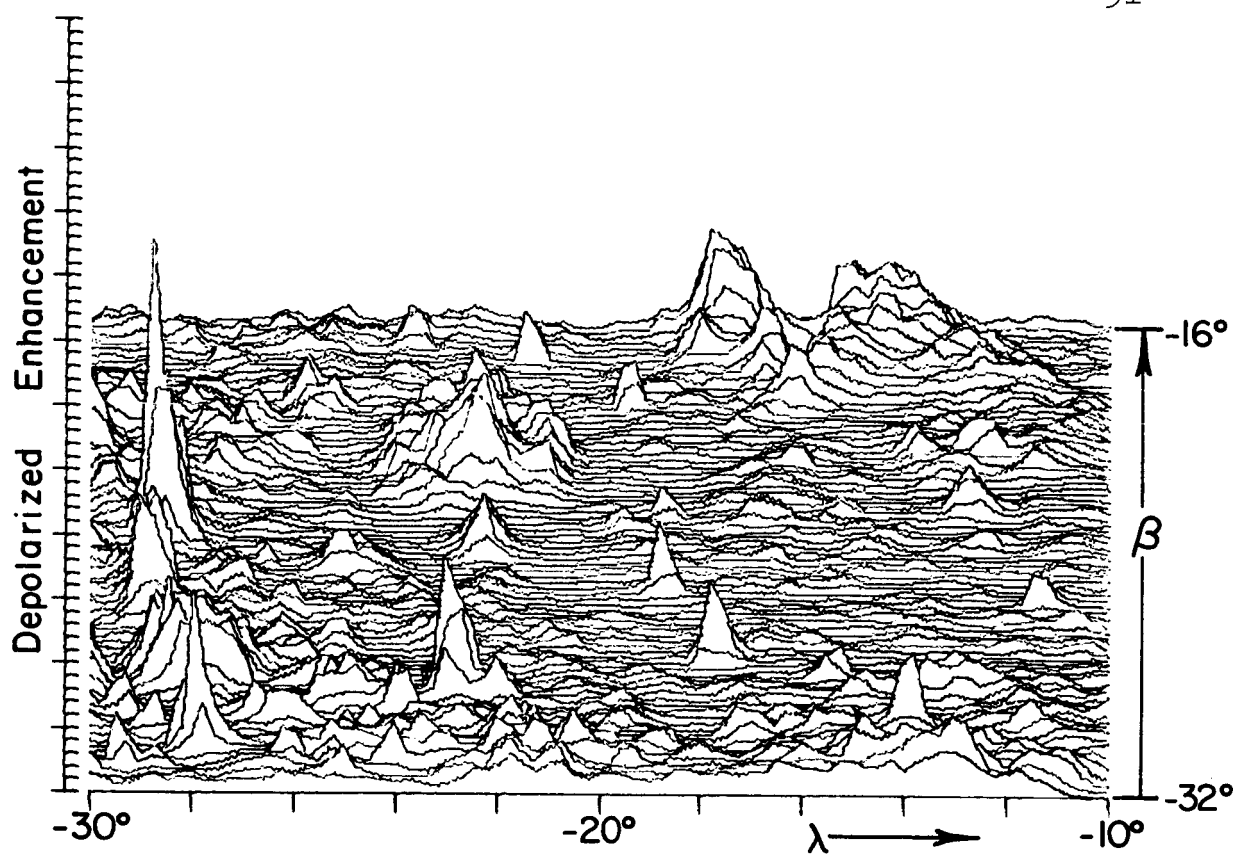


Plate xxi. Isometric Plot of Radar Map of Plate XXI,
LAC 94 Pitatus.

Plate XXII

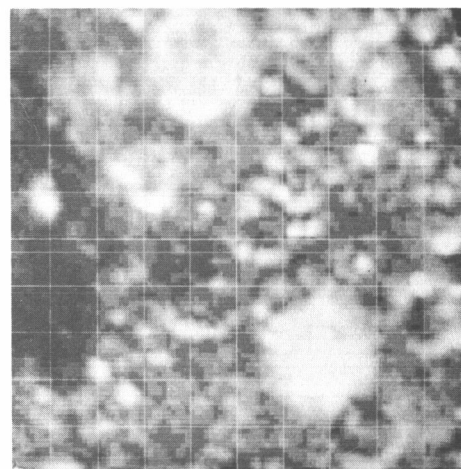
LAC 95 PURBACH

Longitude = -10° , $+10^{\circ}$

Latitude = -32° , -16°

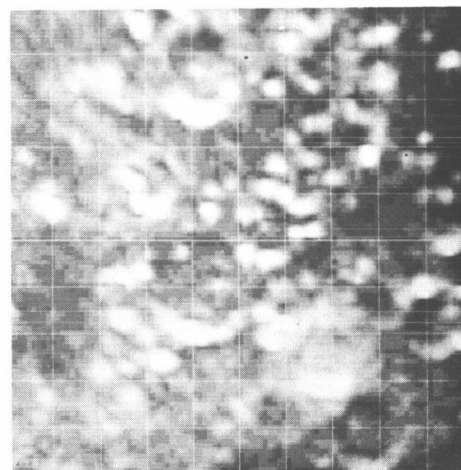
The craters
Arzachel, in the north,
and Werner, in the
southeast, were rough.
In the polarized map,
specular highlights
from the far (south)
rims are seen for many
craters.

Depolarized

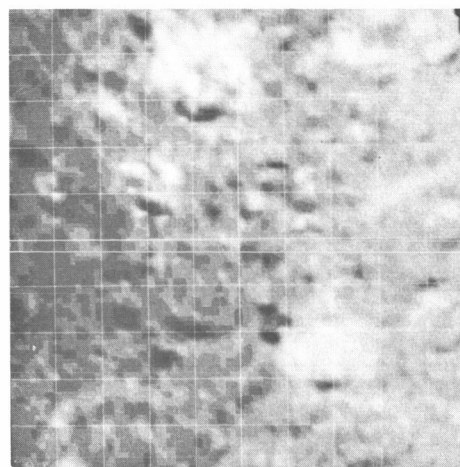


W ←
↓ S

Polarized



Ratio



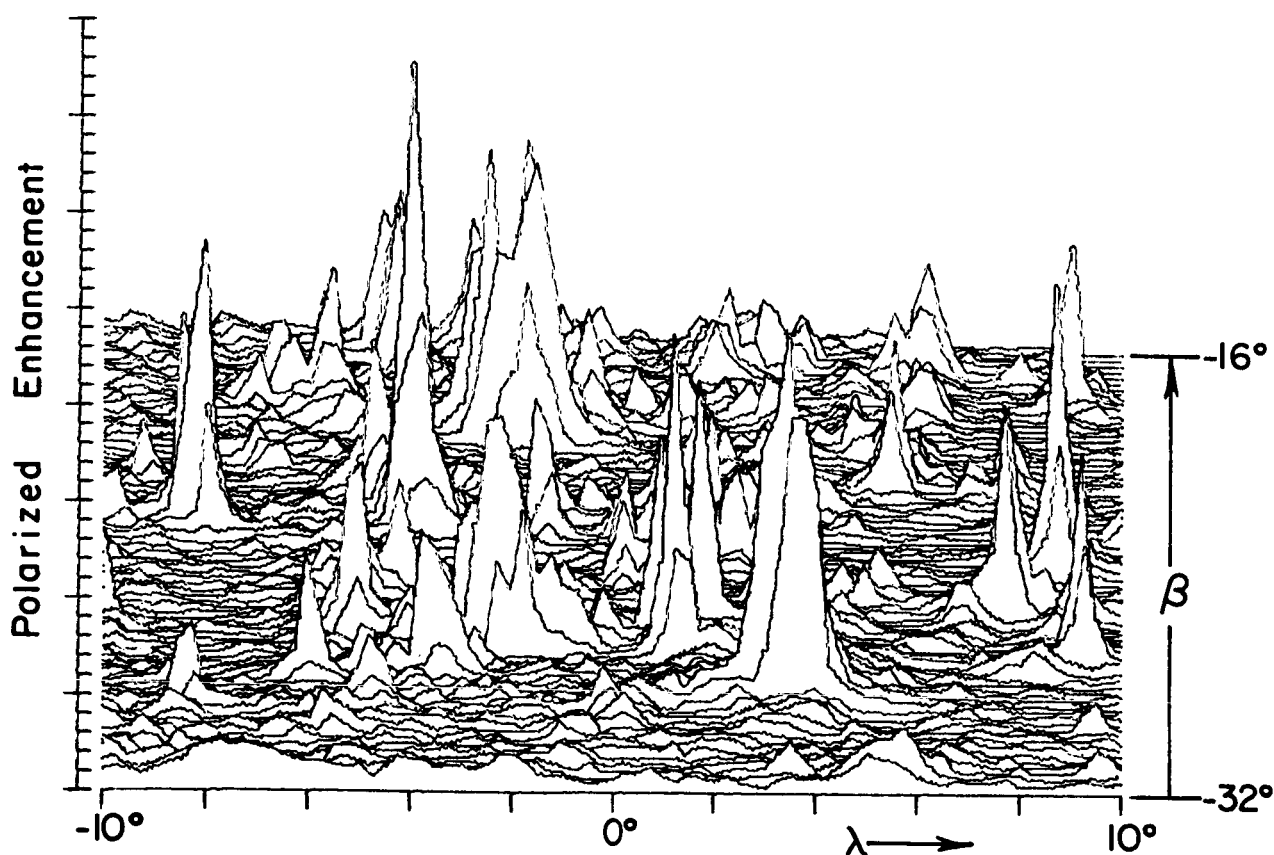
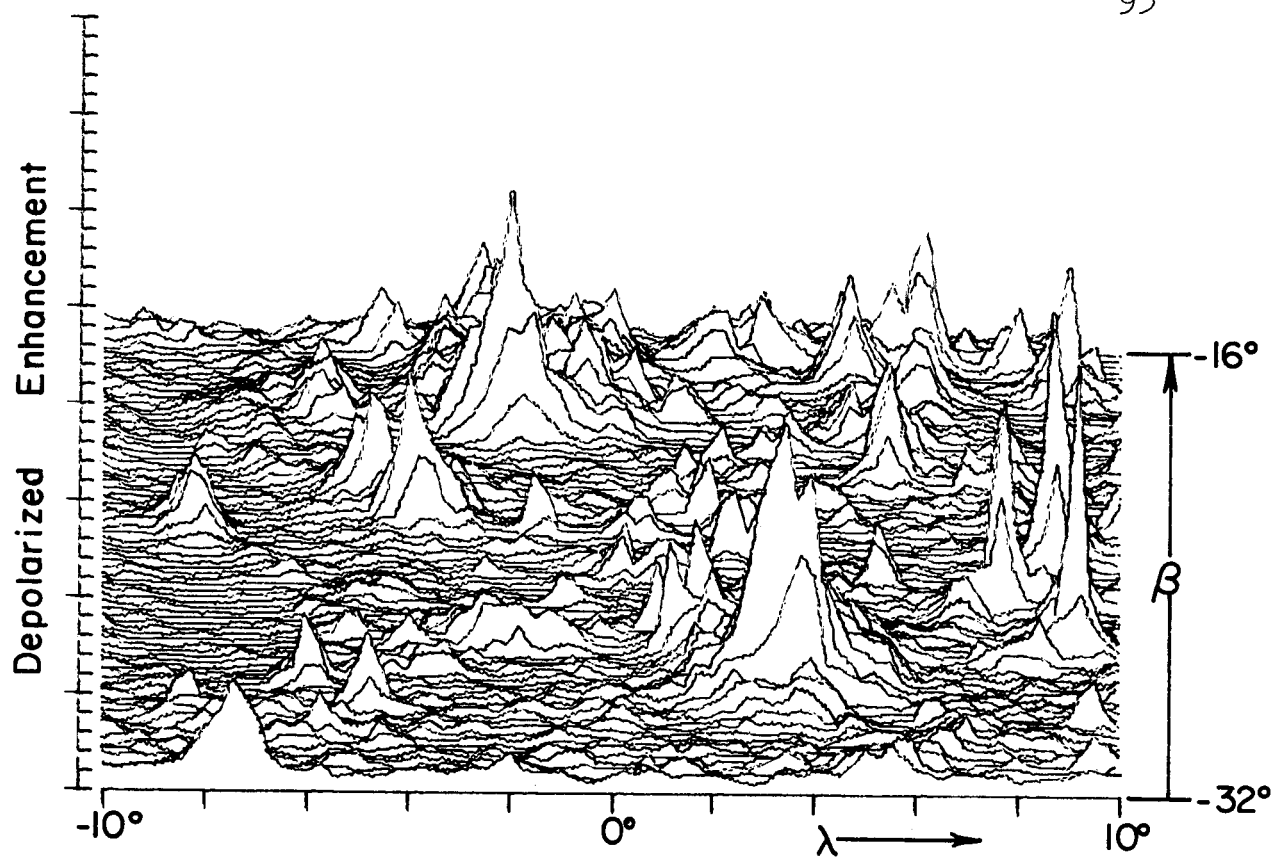


Plate xxii. Isometric Plot of Radar Map of Plate XXII,
LAC 95 Purbach.

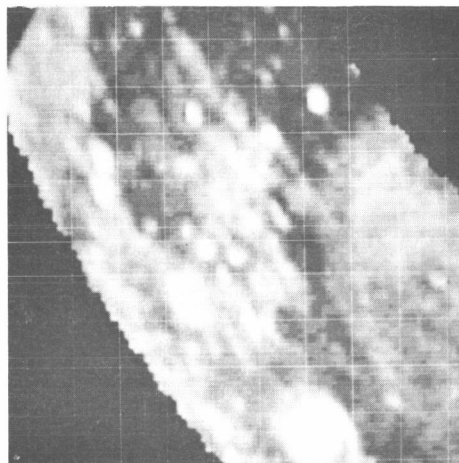
Plate XXIII

B3a TAURUS

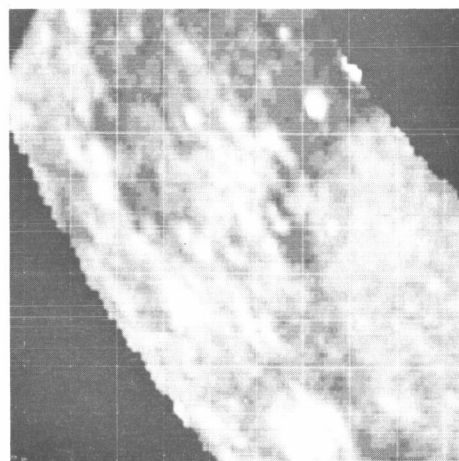
 $\xi = .700, .300$ $\eta = .550, .230$

The crater Posidonius (north) showed a rough rim. The rough area in the center of the map is the crater Römer. The Montes Taurus (center) are rougher than the adjacent areas of Mare Serenitatis to the west and Mare Tranquillitatis to the south. The eastern shore of Mare Serenitatis, which is dark in full-moon photographs, is smoother than the adjacent mare. Many small craters showed backscattering enhancements.

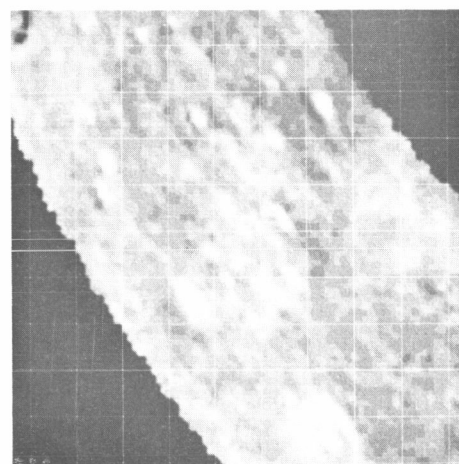
Depolarized



Polarized



Ratio



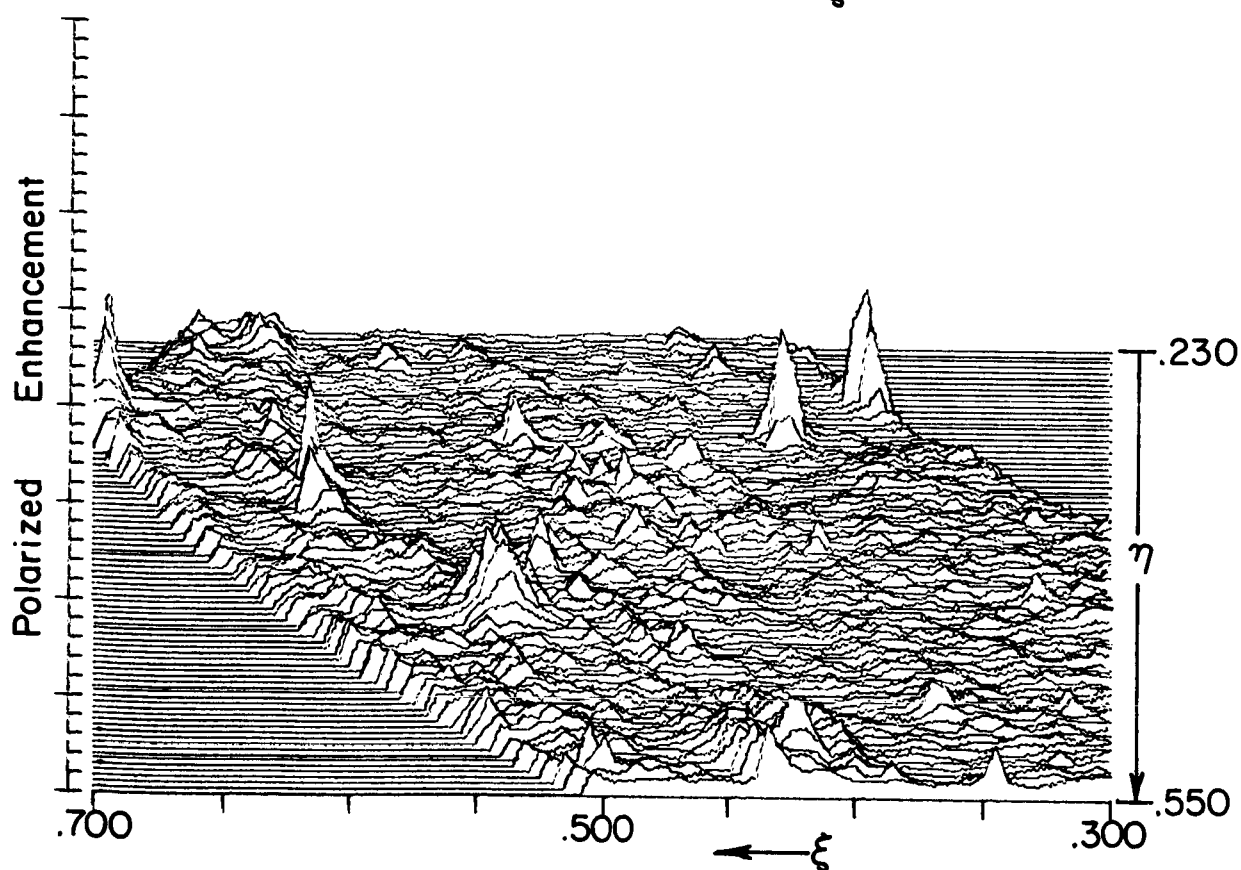
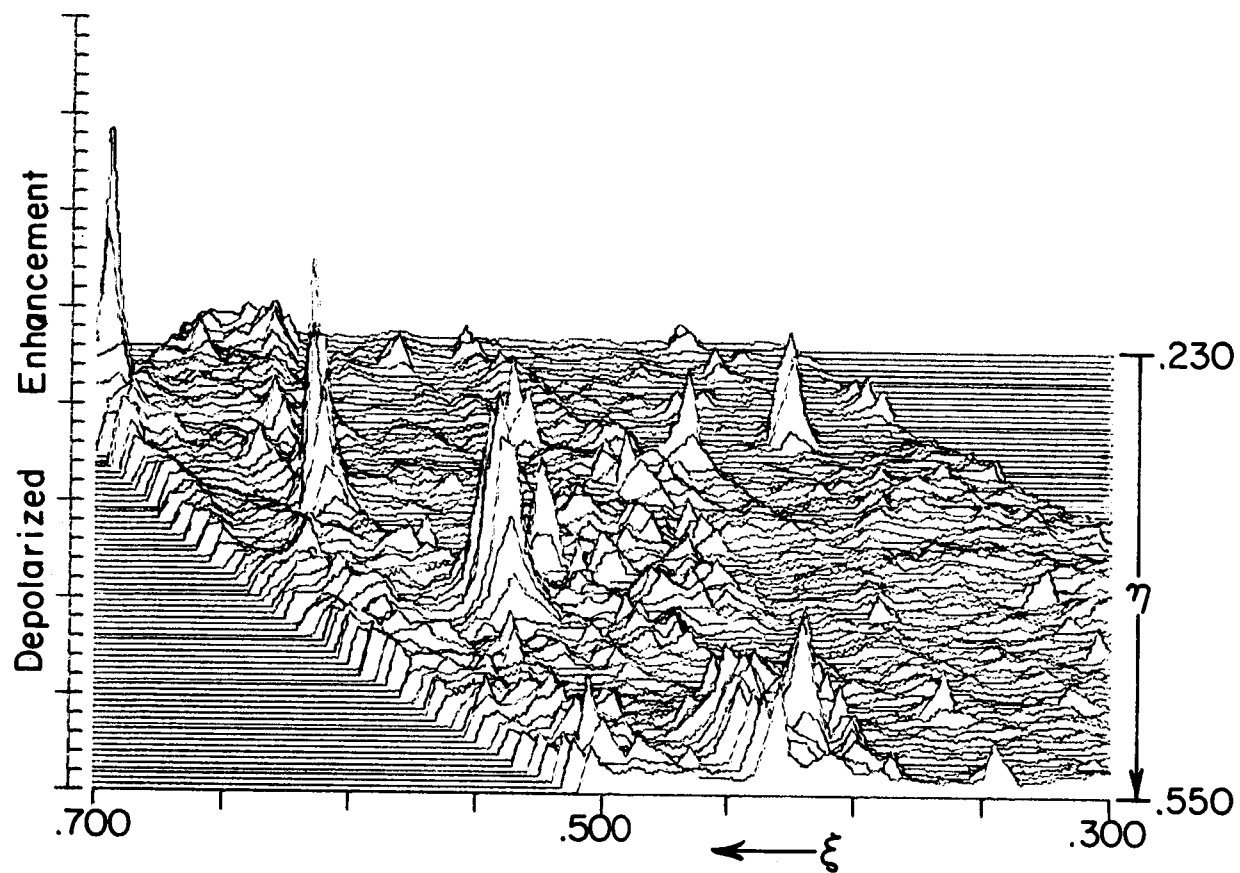


Plate xxiii. Isometric Plot of Radar Map of Plate XXIII,
B3a Taurus.

Plate XXIV

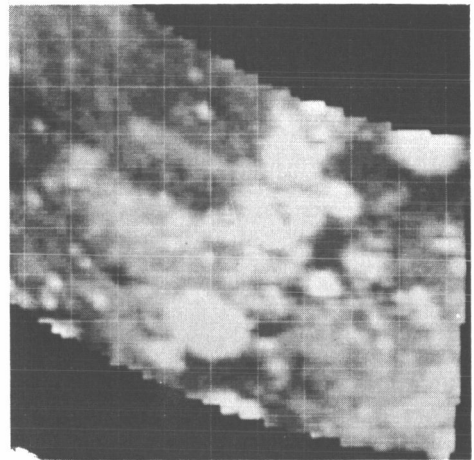
C2a CAUCASUS

$\xi = .380, -.020$

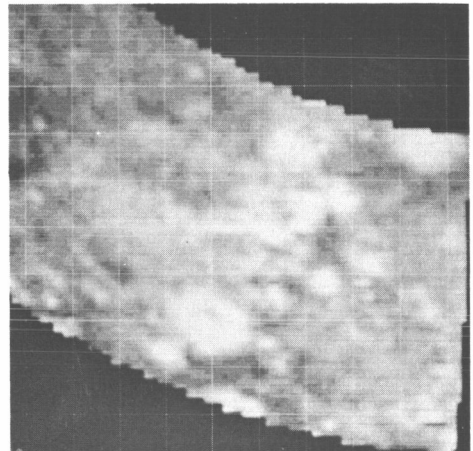
$\eta = .810, .460$

The craters Eudoxus (center) and Aristillus (southwest) were very rough. The Montes Caucasus (center) were rougher than the adjacent areas of Mare Serenitatis to the east and Mare Imbrium to the west. Many small craters showed enhanced radar returns.

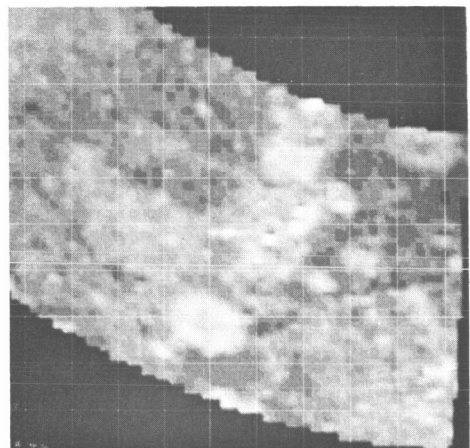
Depolarized



Polarized



Ratio



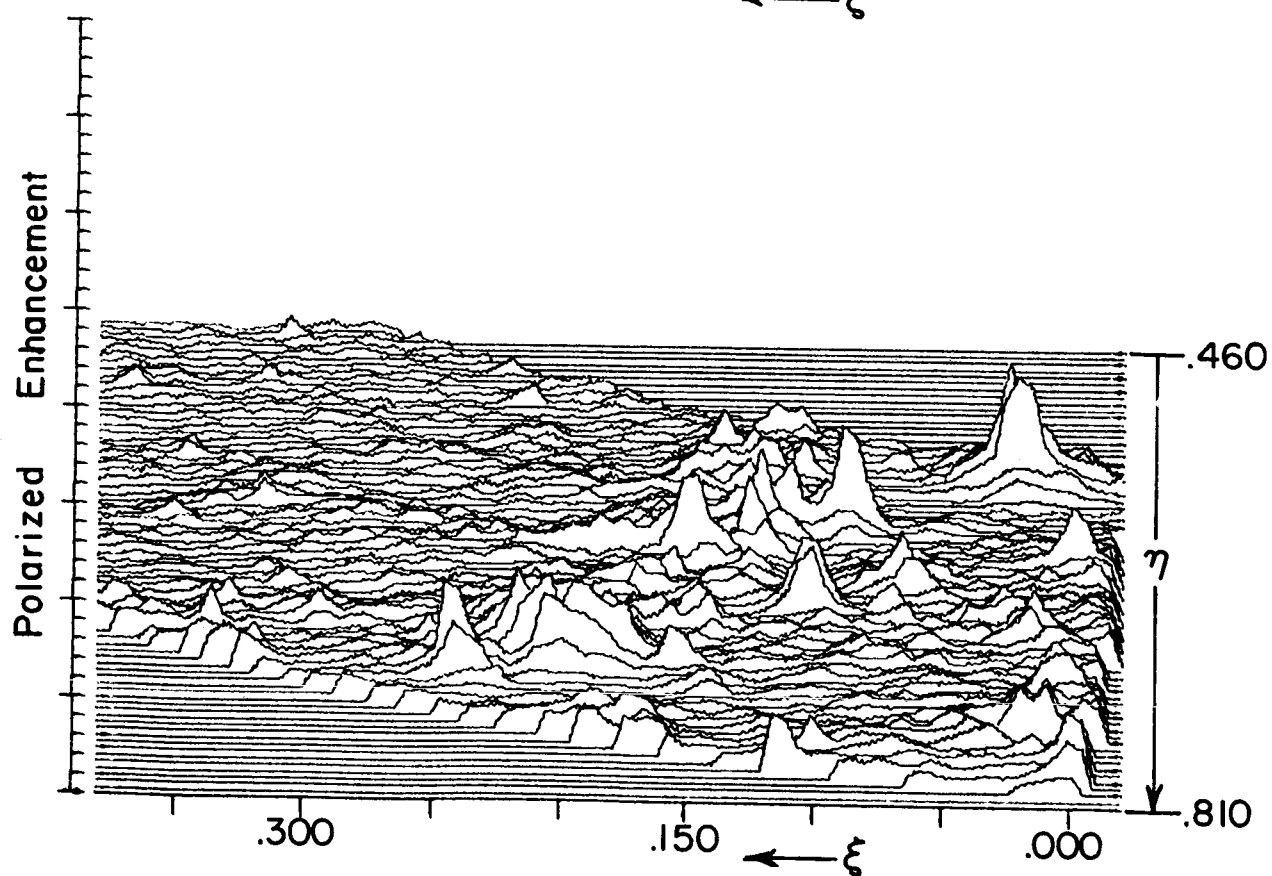
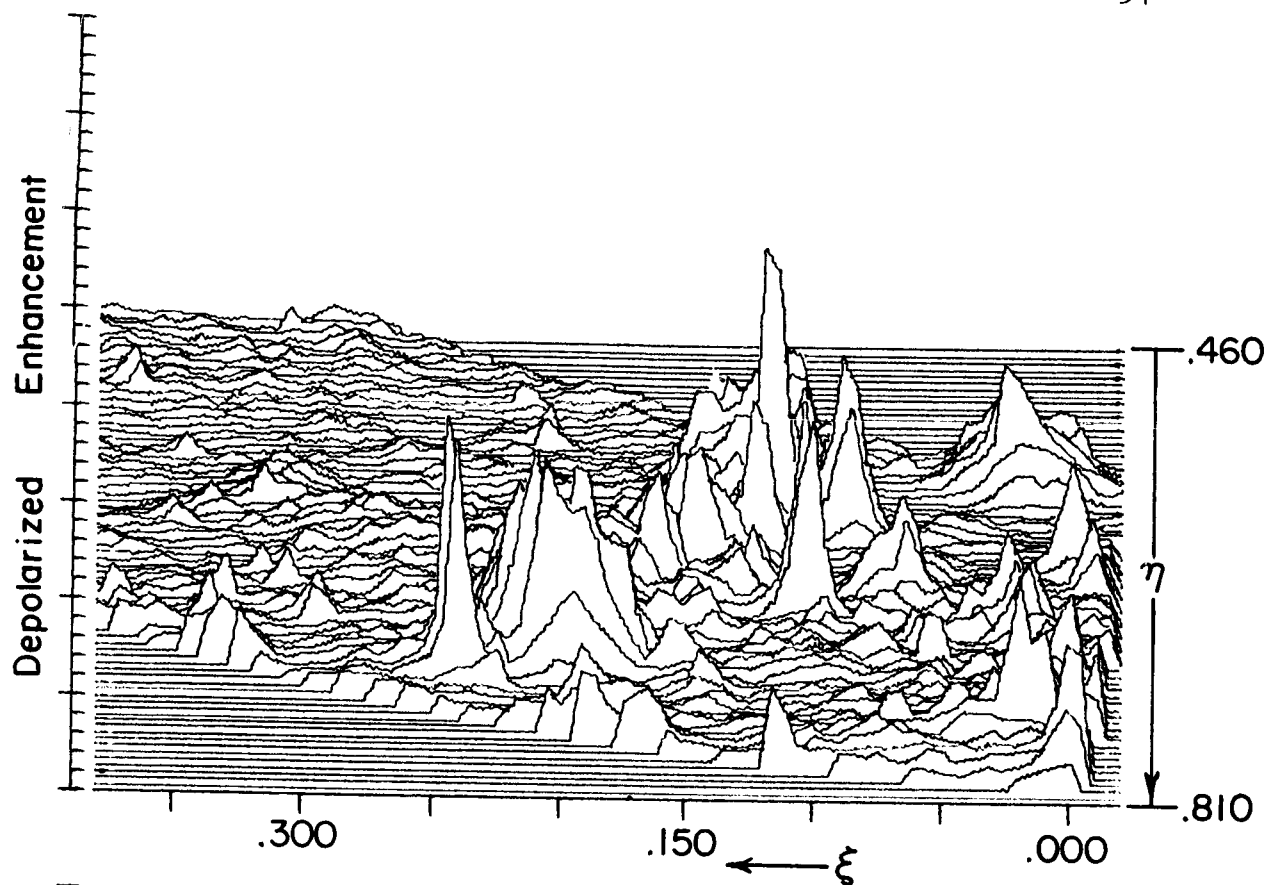


Plate xxiv. Isometric Plot of Radar Map of Plate XXIV,
C2a Caucasus.

Plate XXV

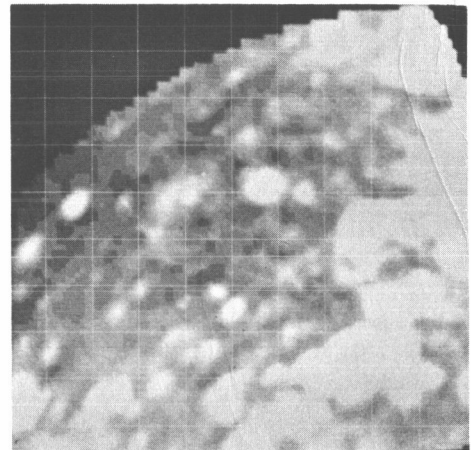
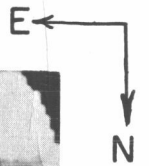
C7a MAUROLYCUS

$\xi = .380, -0.100$

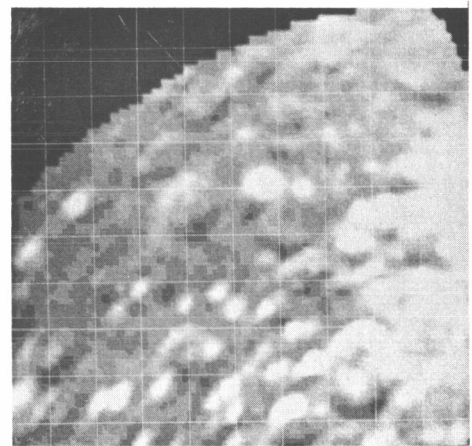
$\eta = -.490, -.830$

The slightly rough area in the center of this map is the crater Maurolycus. Many specular highlights can be seen at the far (south) rims of the craters. The bright areas in the west are near the crater Tycho. Specular highlights were shown by many small craters.

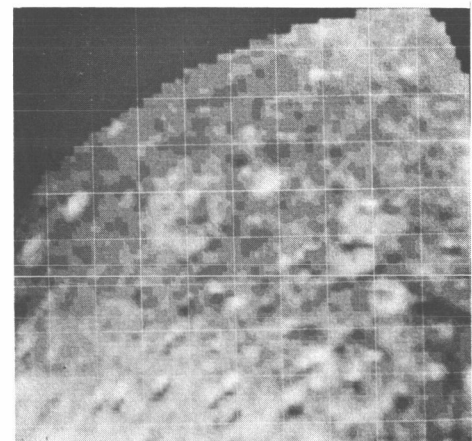
Depolarized



Polarized



Ratio



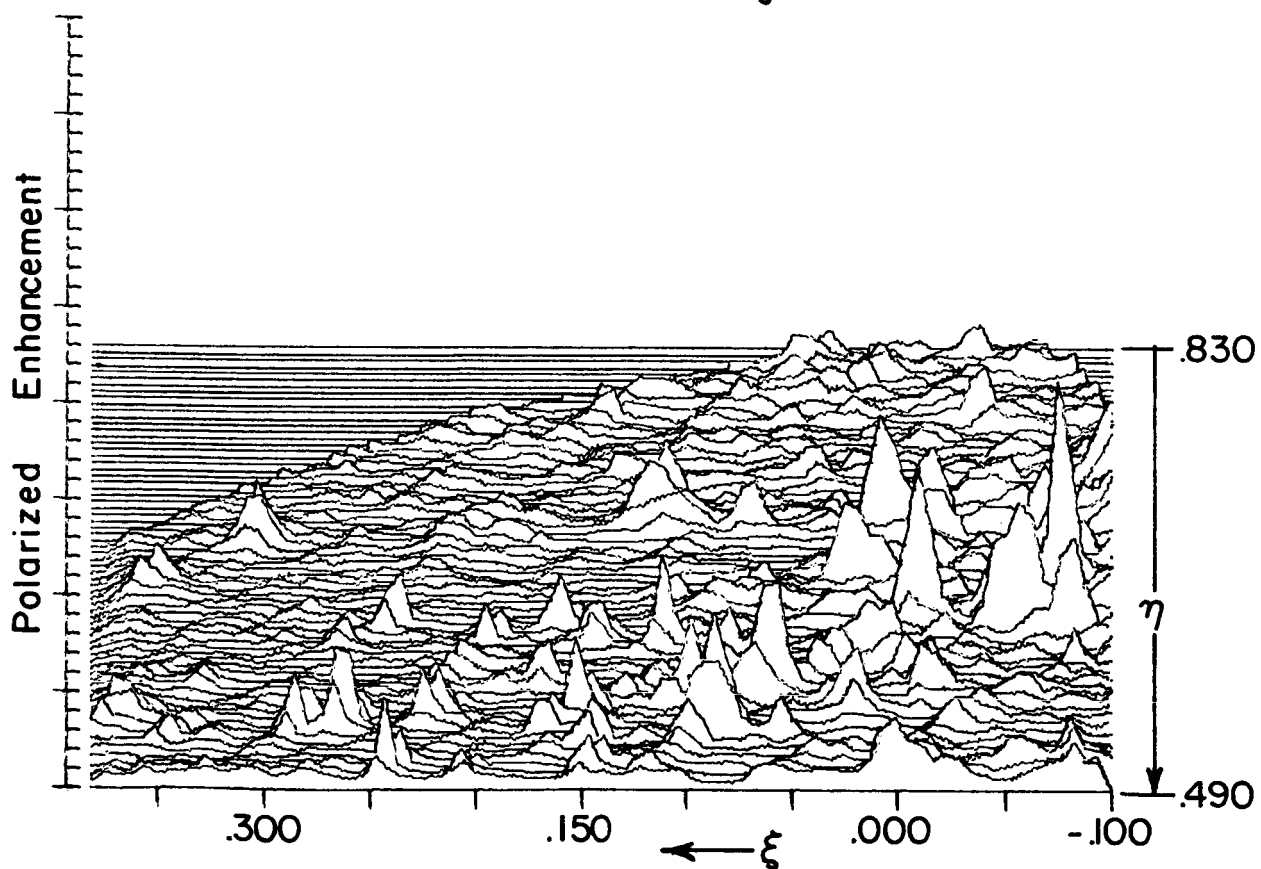
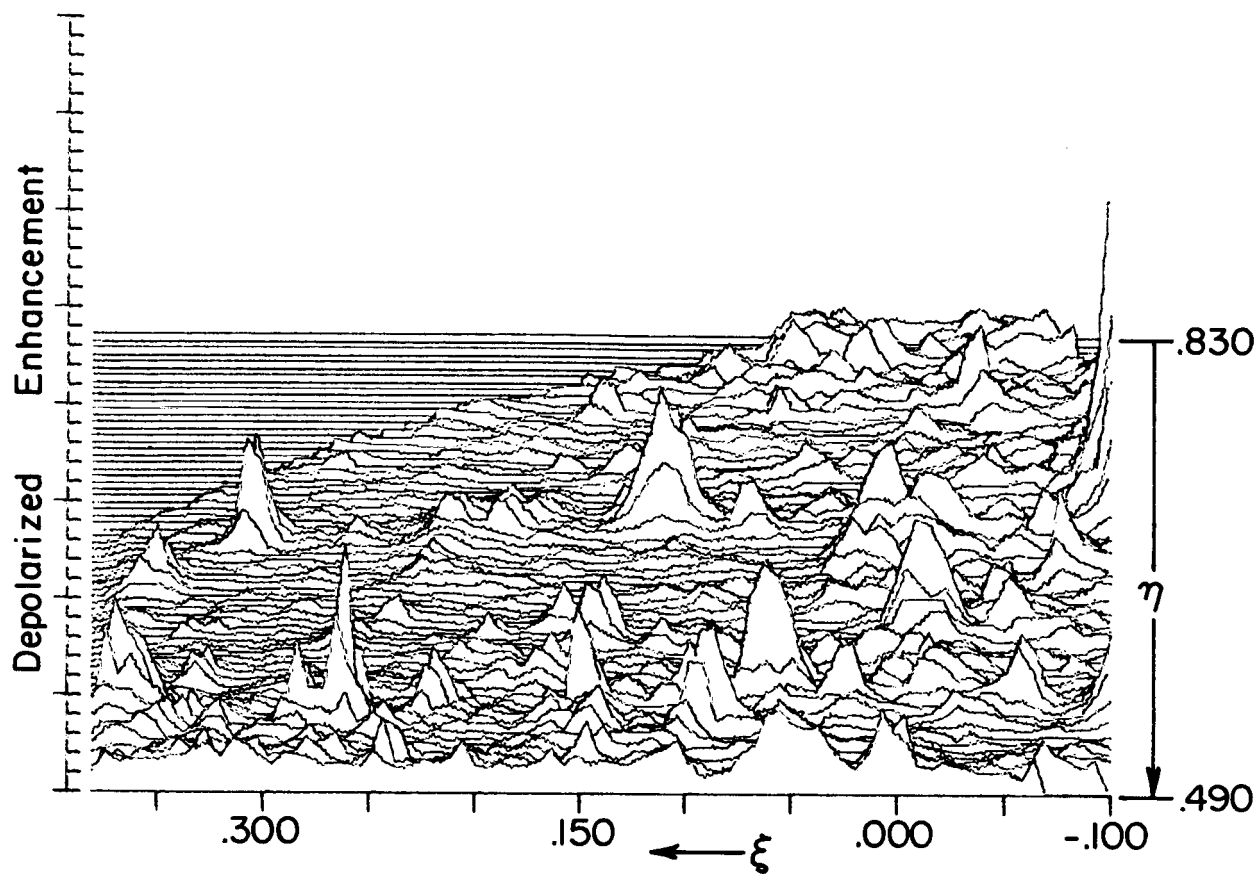


Plate xxv. Isometric Plot of Radar Map of Plate XXV,
C7a Maurolycus.

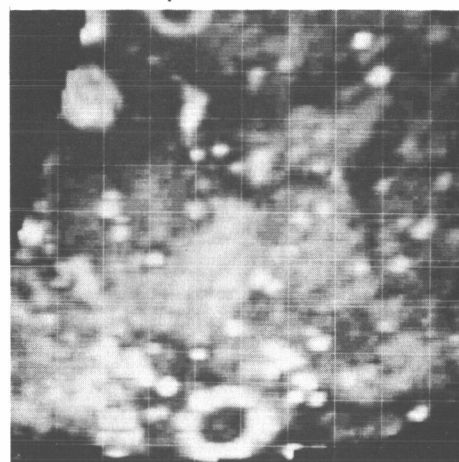
Plate XXVI

D2a PLATO

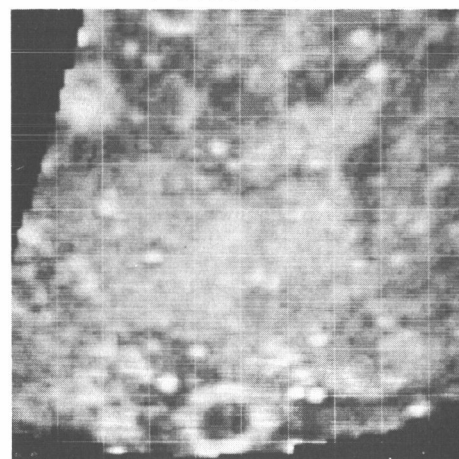
 $\xi = .085, -.315$ $\eta = .820, .500$

The crater Plato (north) and Archimedes (south) showed only rough rims. The crater Aristillus (southeast) was very rough. A portion of Mare Imbrium, (center), an area that is not distinguished optically, was observed to be rough. The Montes Spitzbergensis, Montes Teneriffe, and Montes Recti were rougher than the adjacent maria. The Montes Alpes (northeast) appeared to be slightly rougher than Mare Imbrium. Many small craters showed enhanced back-scattering. These data were also mapped onto longitude and latitude coordinates and are shown in Plate II.

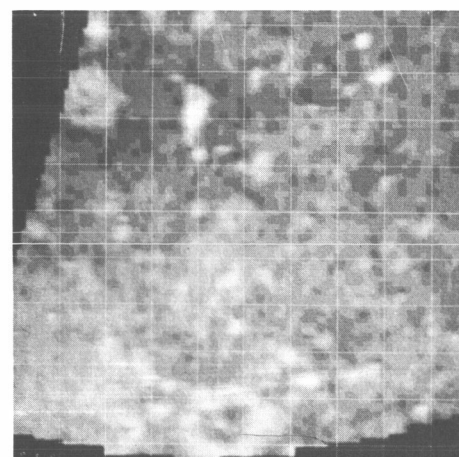
Depolarized



Polarized



Ratio



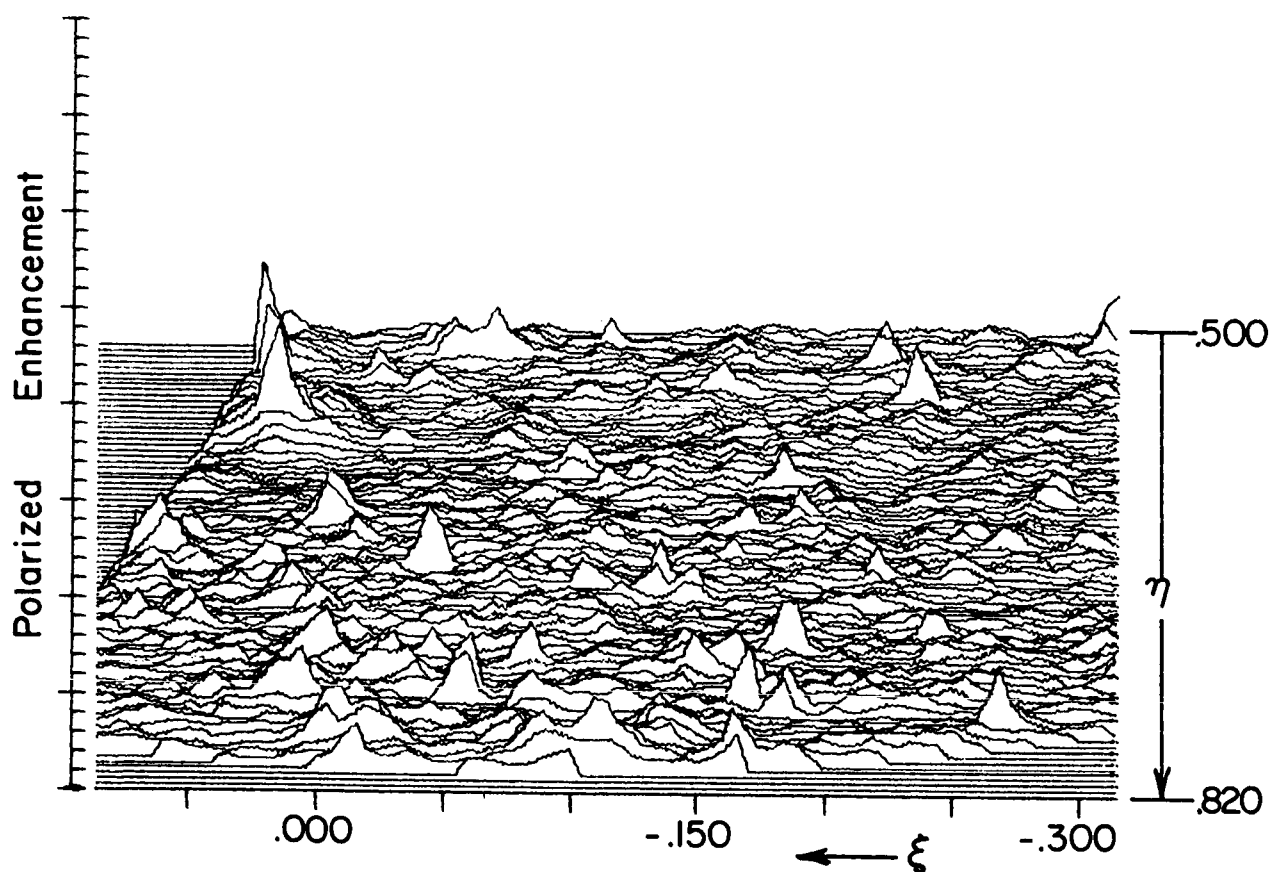
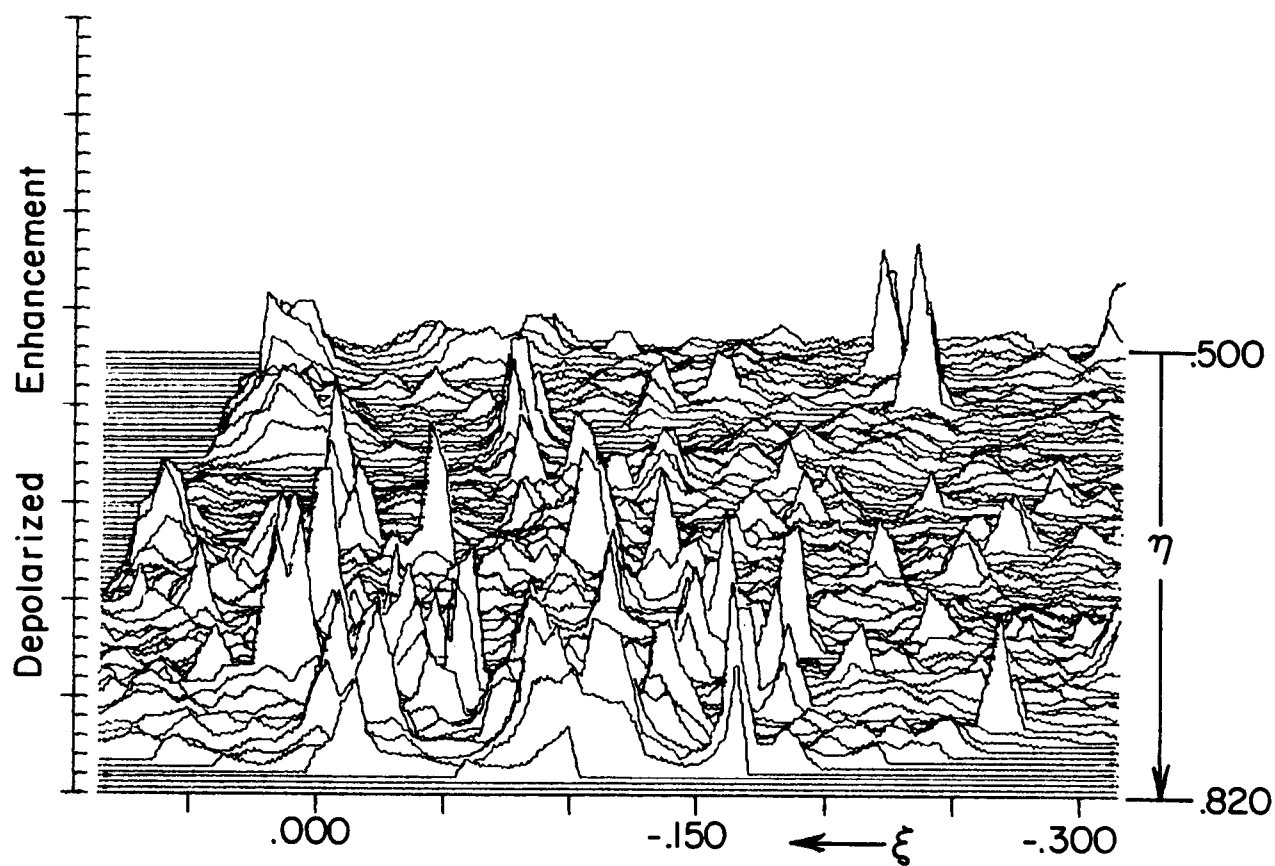


Plate xxvi. Isometric Plot of Radar Map of Plate XXVI,
D2a Plato.

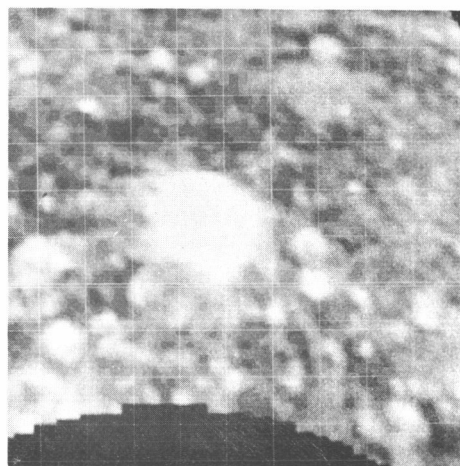
Plate XXVII

D7a TYCHO

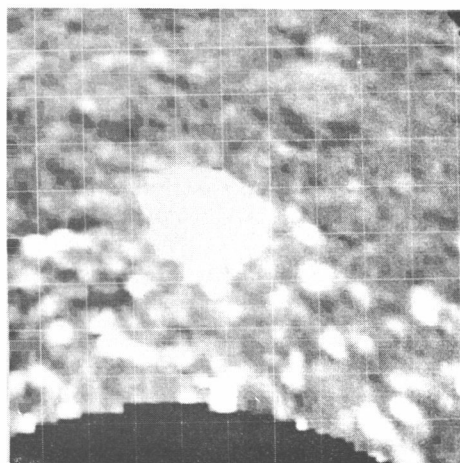
 $\xi = .030, -.370$ $\eta = -.510, -.830$

The very rough area in the center of the map is the rayed crater Tycho. Some modulation in echo intensity is aligned with the rays to the north of Tycho. The large crater Longomontanus (southwest) was slightly rough. Many craters to the north of Tycho showed specular highlights from their far (southern) rims. Several of these were rougher than their environs, as shown in the ratio map. The crater Tycho was mapped with a twofold improvement in resolution, and is shown in Plate XXXI.

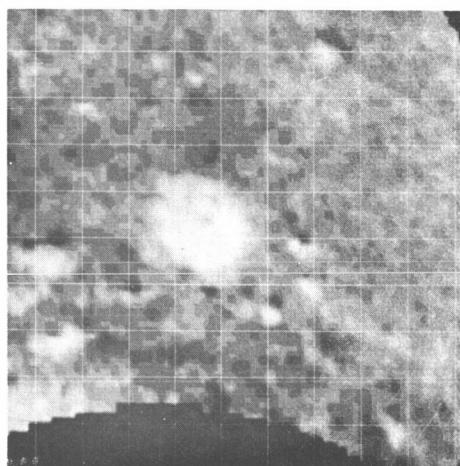
Depolarized



Polarized



Ratio



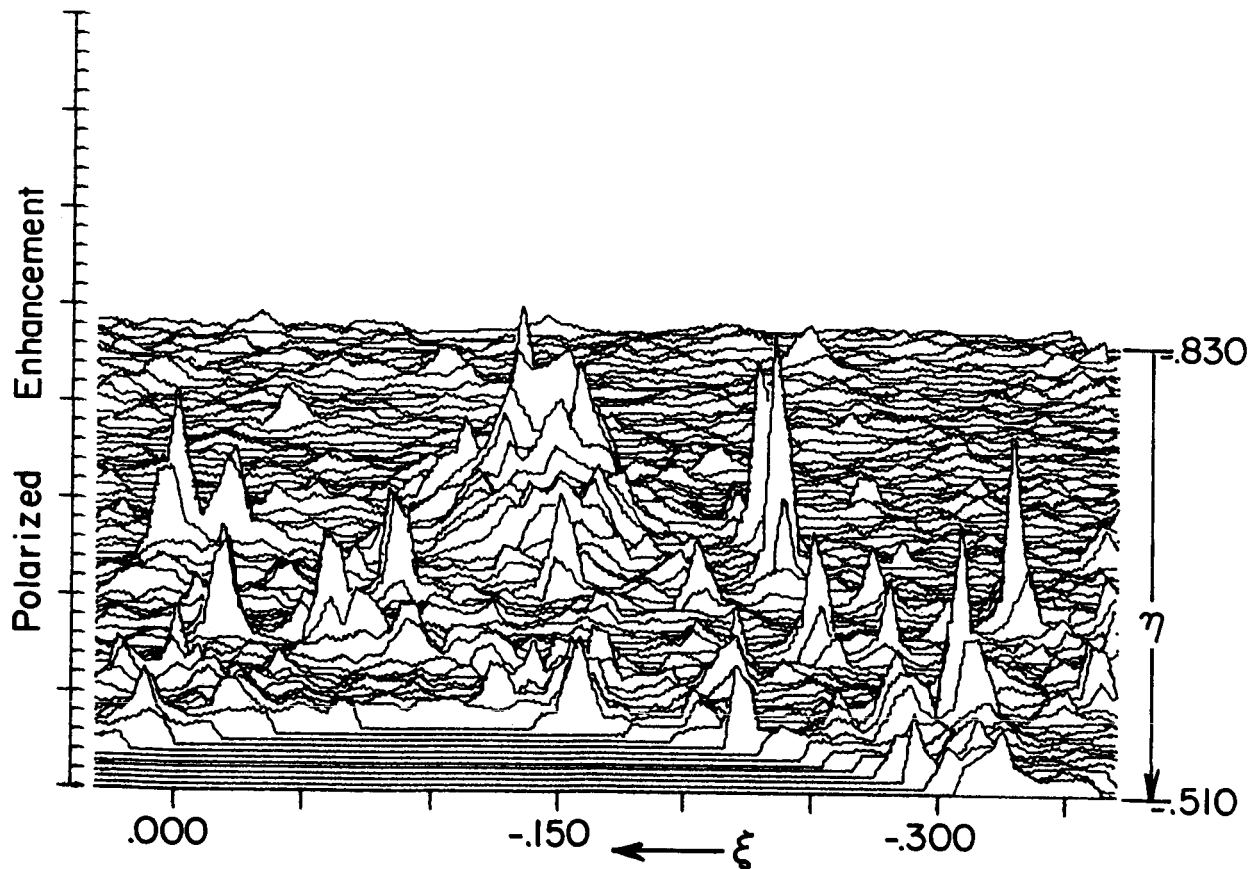
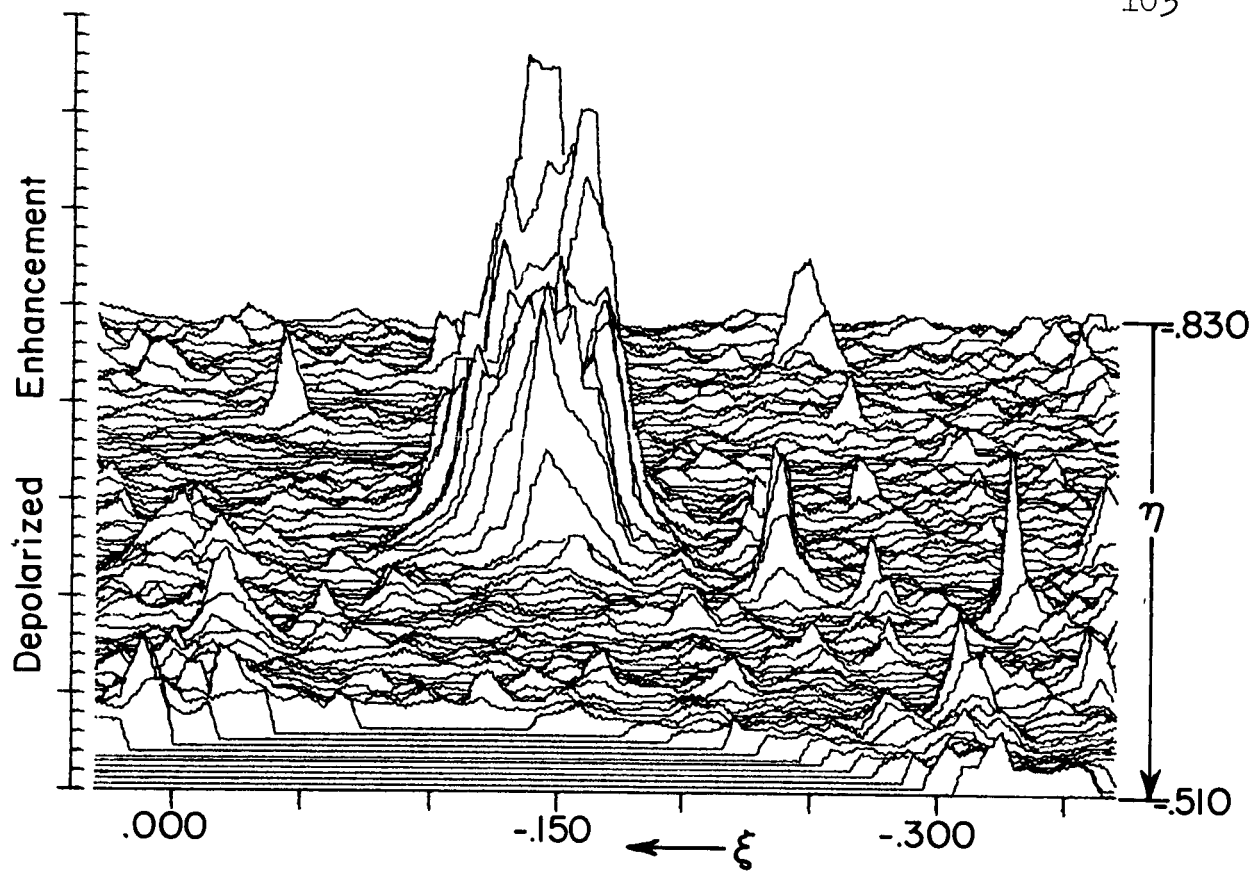


Plate xxvii. Isometric Plot of Radar Map of Plate XXVII,
D7a Tycho.

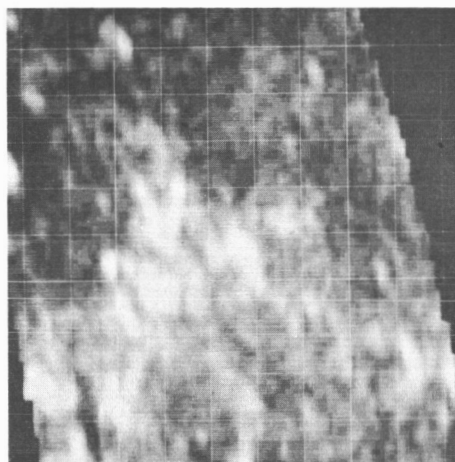
Plate XXVIII

LUNAR ORBITER SITE II-P-2

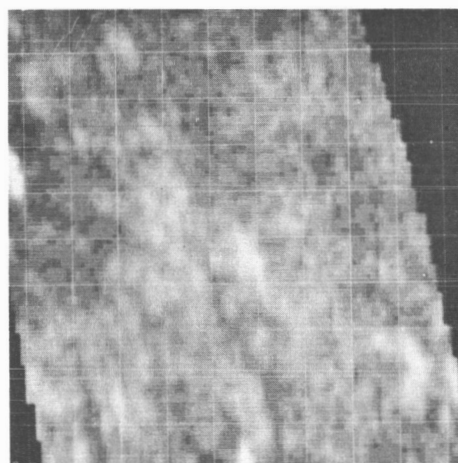
Longitude = 30° , 38° Latitude = -4° , $+6^{\circ}$

The Lunar Orbiter Site II-P-2 is centered on a longitude of $34^{\circ}00'$ east and a latitude of $2^{\circ}40'$ north. The rough area in the center of the map is the Montes Pyrenaei. The Lunar Orbiter Site, which was not markedly different from the adjacent areas of Mare Tranquillitatis, was smoother than the highland areas of the Montes Pyrenaei.

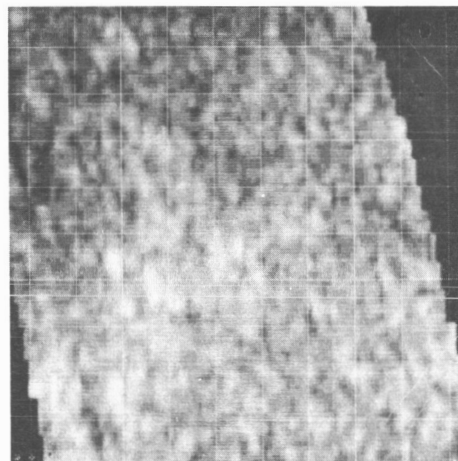
Depolarized



Polarized



Ratio



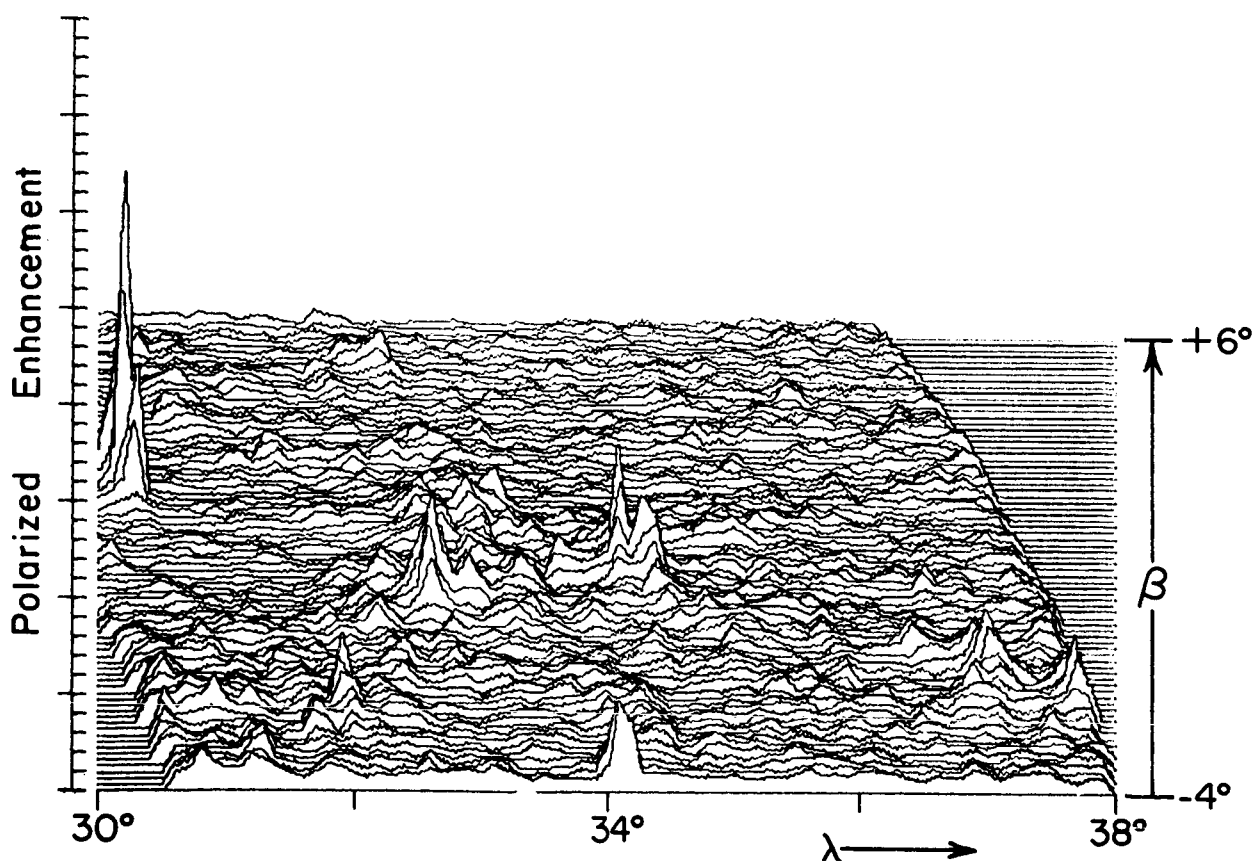
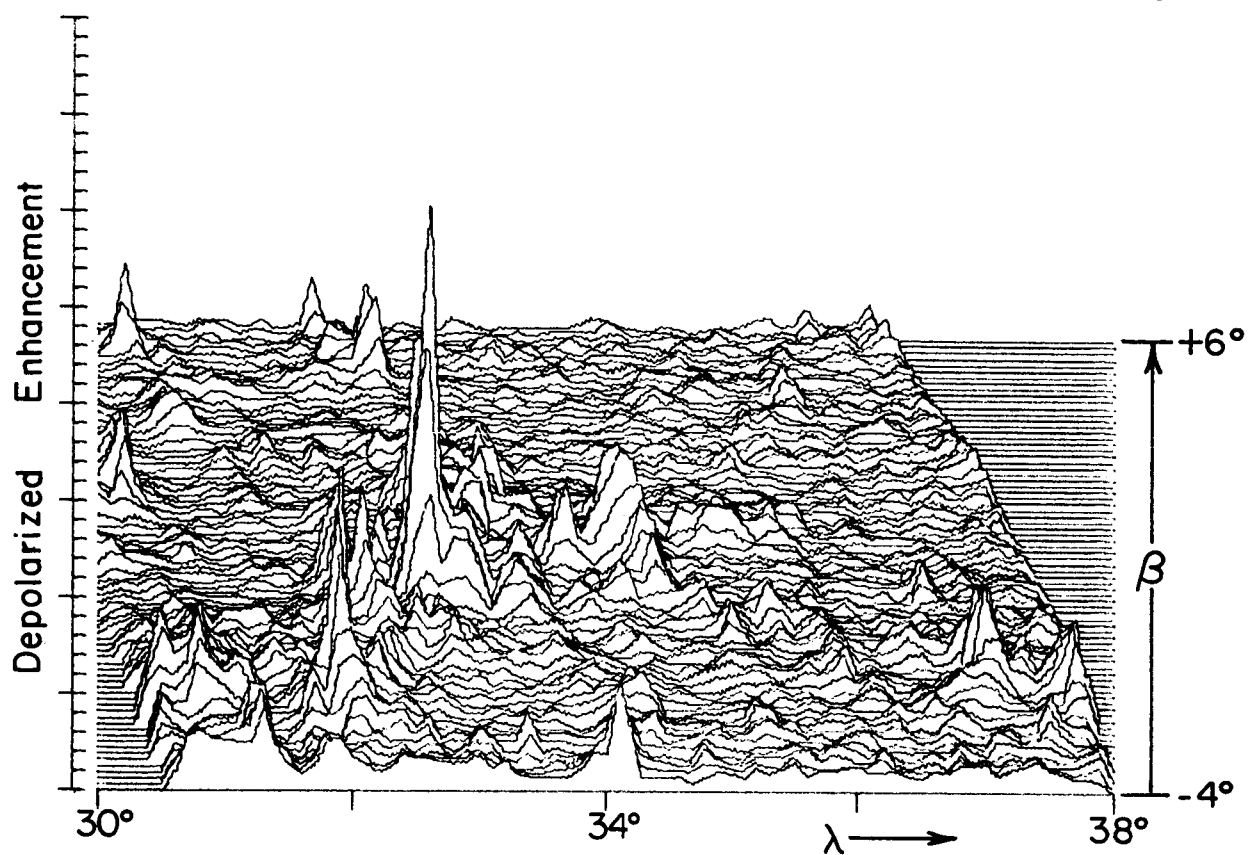


Plate xxviii. Isometric Plot. of Radar Map of Plate XXVIII,
Lunar Orbiter Site II-P-2.

Plate XXIX

LUNAR ORBITER SITE
II-P-6 and

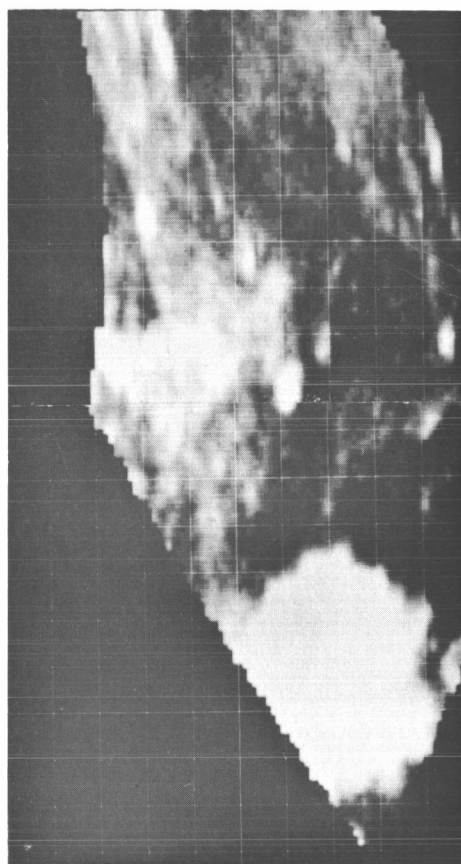
CRATER THEOPHILUS

Longitude = 18° , 30°

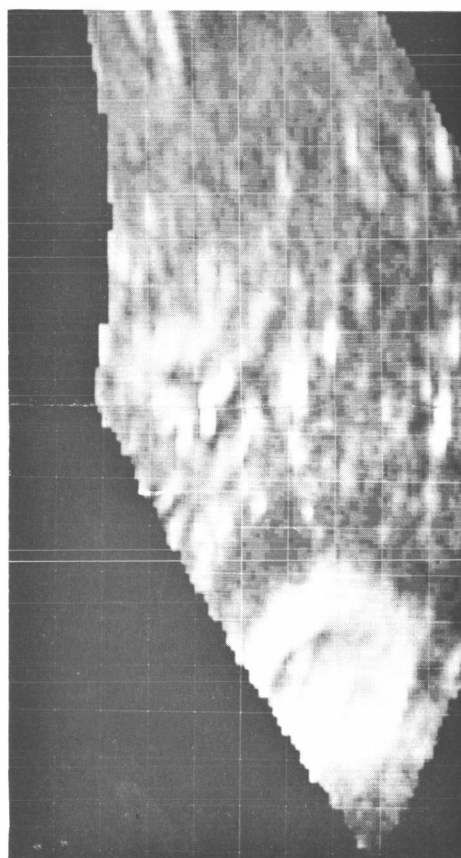
Latitude = -16° , 6°

The Lunar Orbiter Site II-P-6 is located at a longitude of $23^{\circ} 37'$ east and a latitude of $0^{\circ} 45'$ north; the landing site of the Ranger VIII Spacecraft is at a longitude of 24.61° east and a latitude of 2.72° north; and the landing site of the Surveyor V Spacecraft is at a longitude of 23.29° east and a latitude of 1.49° north. The very rough area in the south is the rayed crater Theophilus.

Depolarized



Polarized



LUNAR ORBITER SITE II-P-6
and CRATER THEOPHILUS

(There are no isometric plots for this map.)

Plate XXX

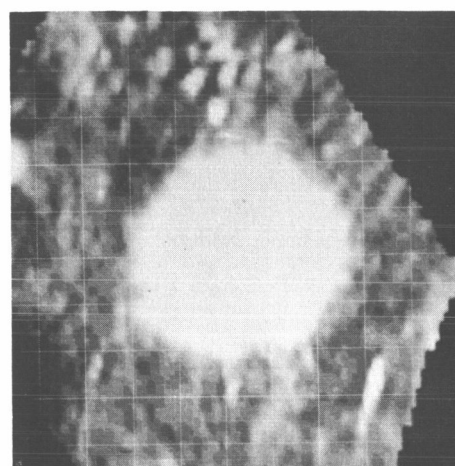
CRATER COPERNICUS

Longitude = -26° , -14°

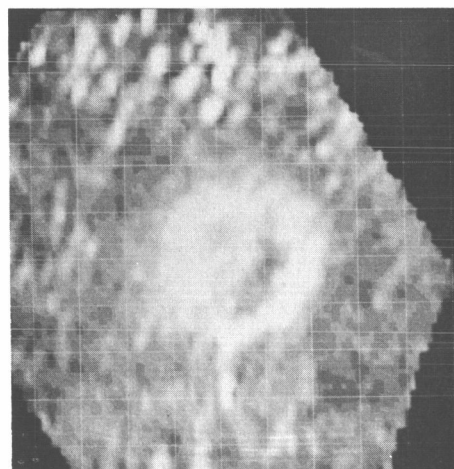
Latitude = 4° , 16°

The extremely rough area in the center of the map is the large rayed crater Copernicus. The Montes Carpatum, (north) had specular highlights.

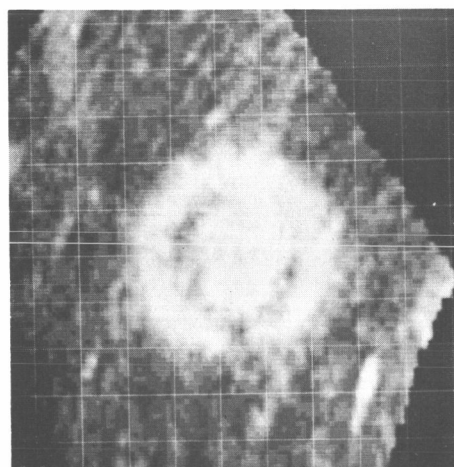
Depolarized



Polarized



Ratio



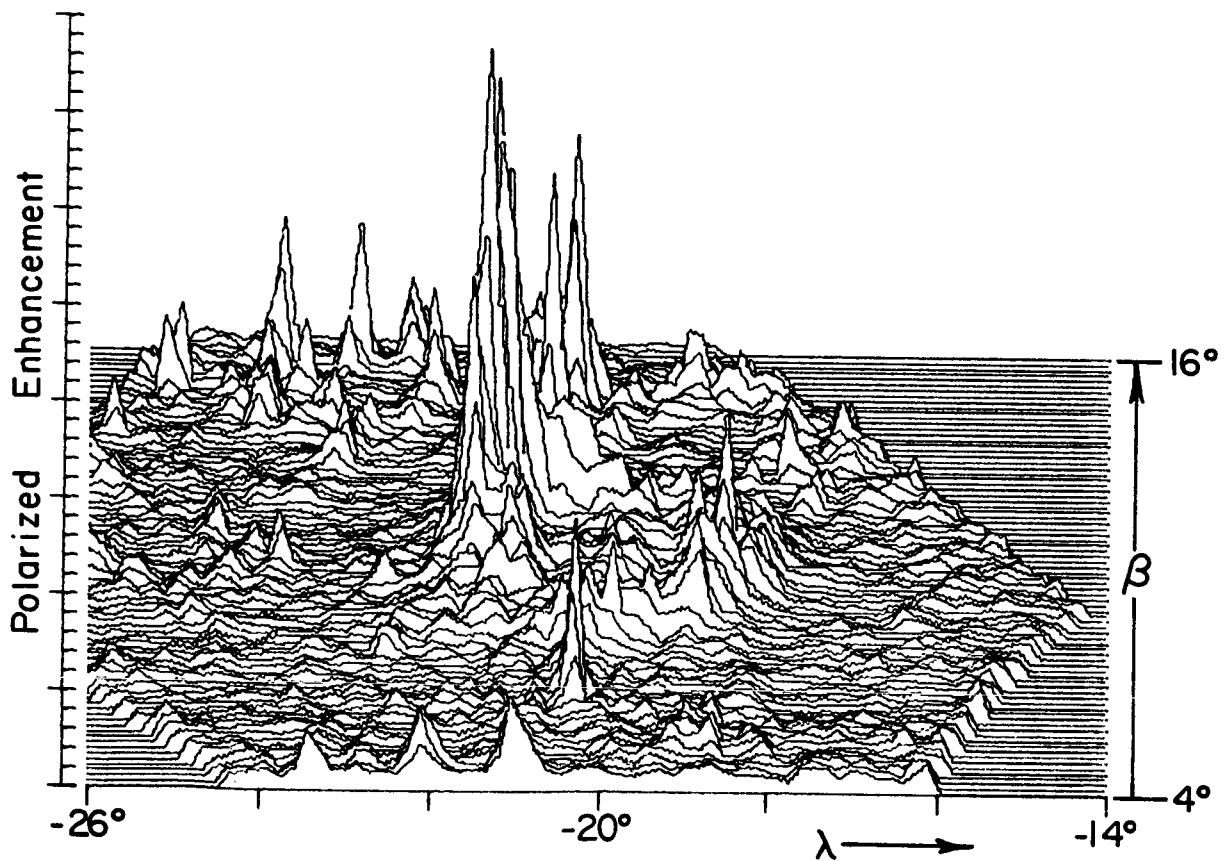
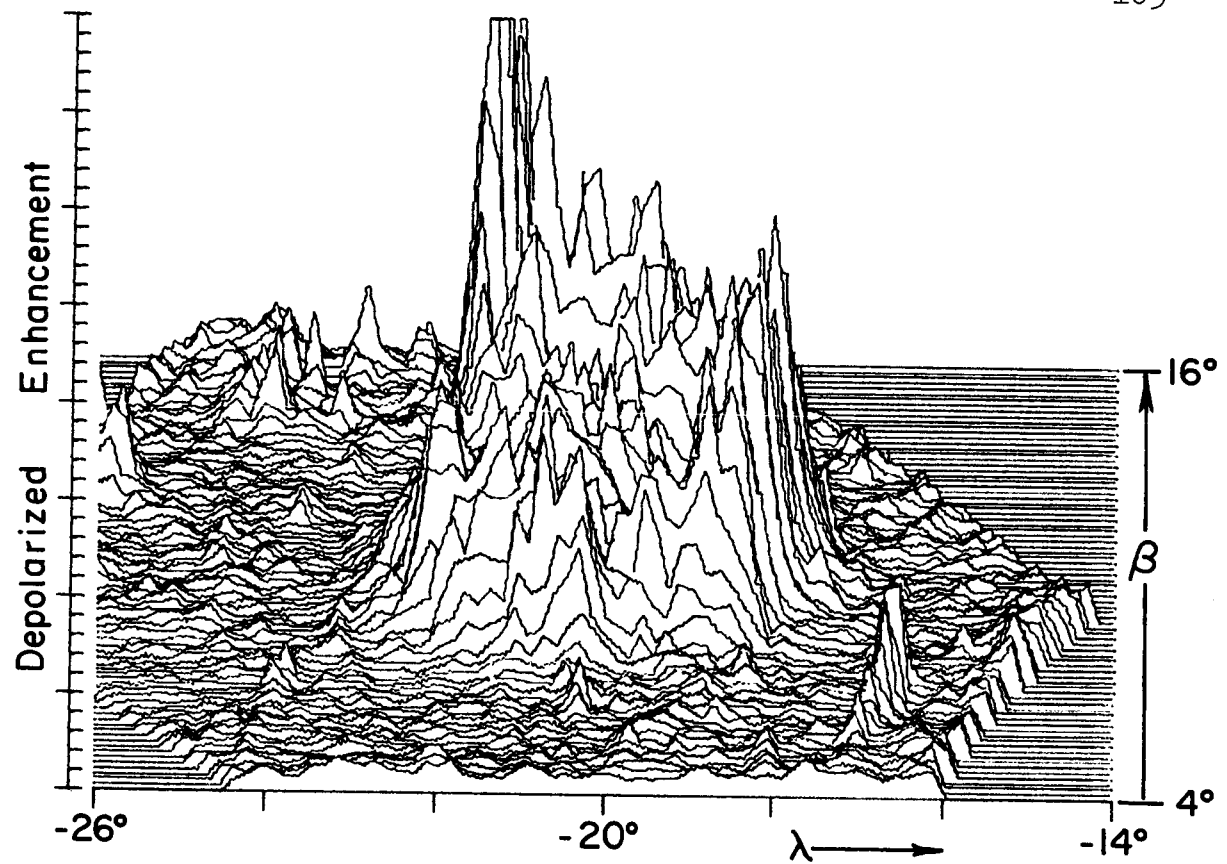


Plate xxx. Isometric Plot of Radar Map of Plate XXX,
Crater Copernicus.

Plate XXXI

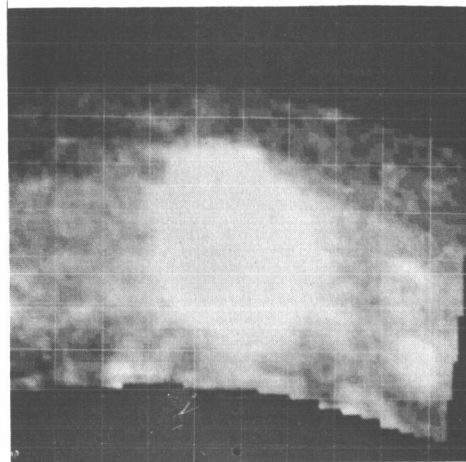
CRATER TYCHO

$\xi = -.020, -.260$

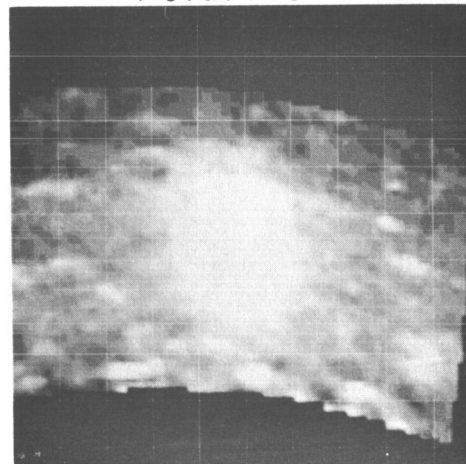
$\eta = -.760, -.600$

The extremely
rough area in the center
of the map is the rayed
crater Tycho.

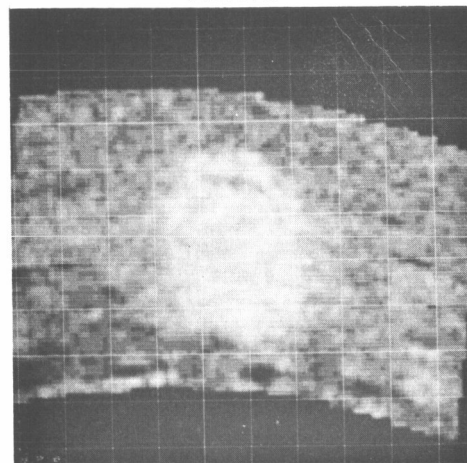
Depolarized



Polarized



Ratio



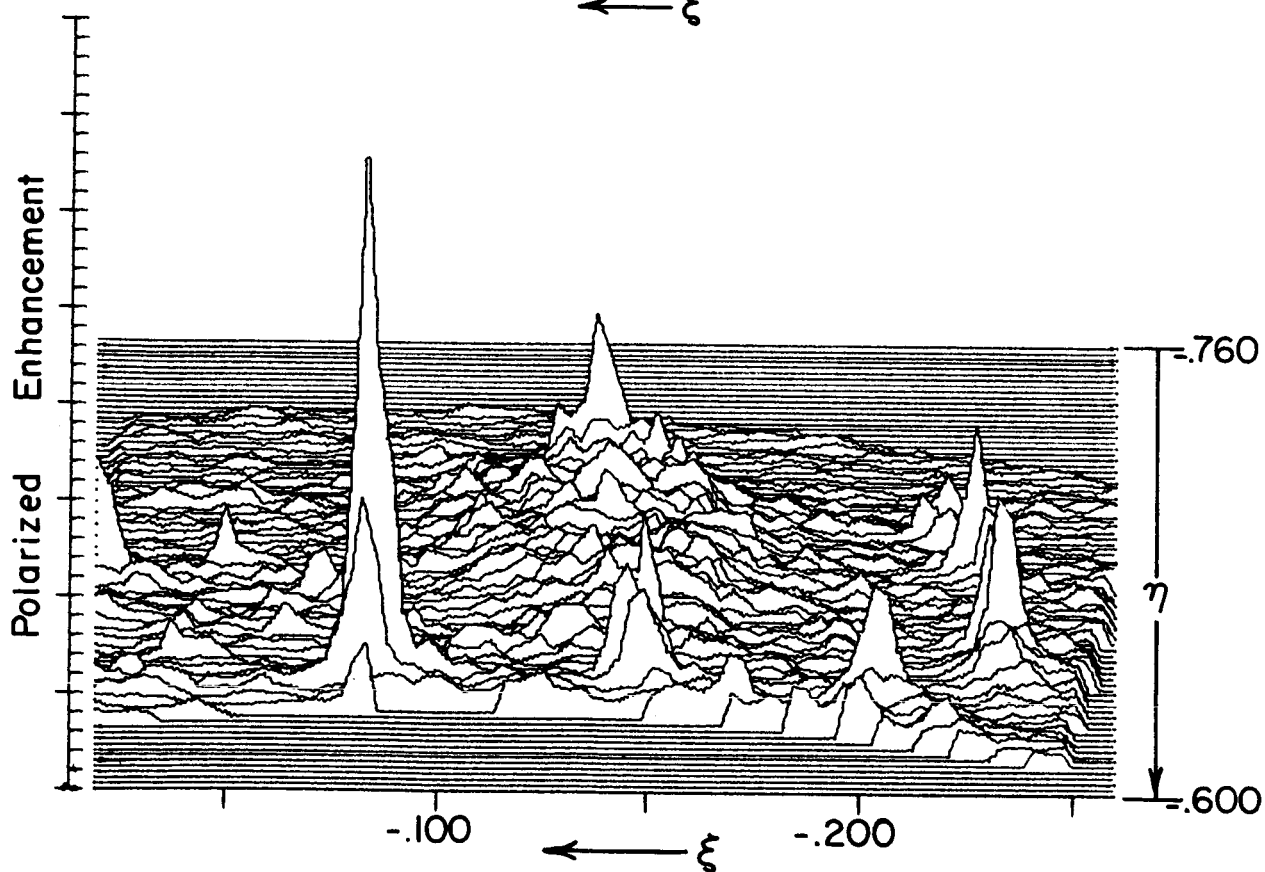
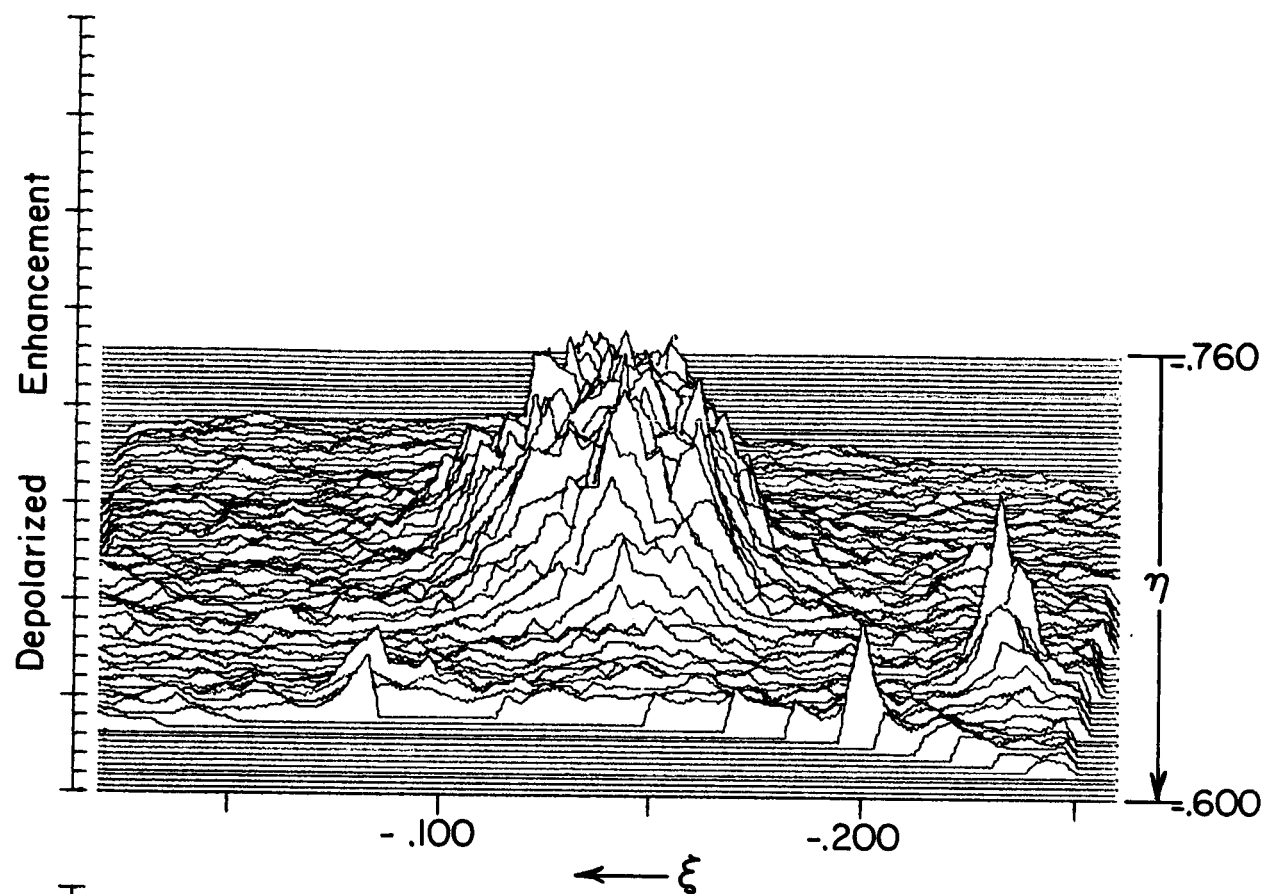
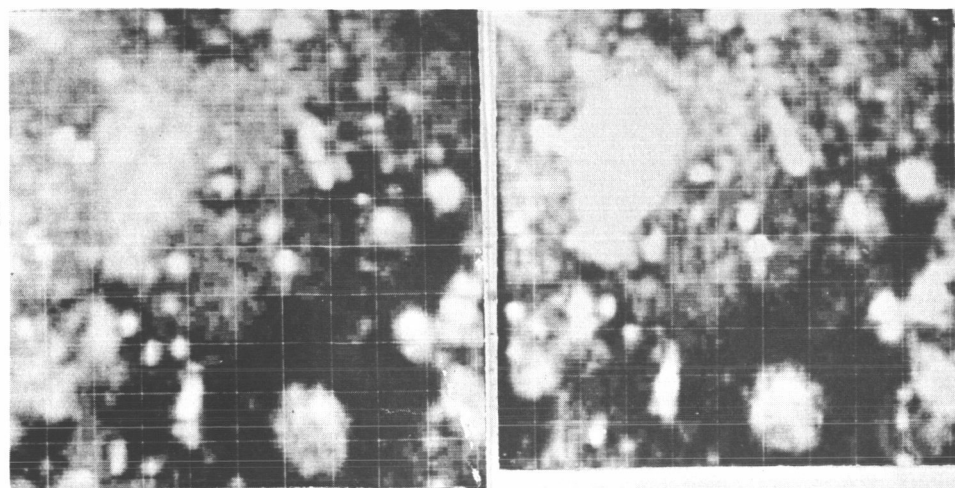


Plate xxxi. Isometric Plot of Radar Map of Plate XXXI,
Crater Tycho.

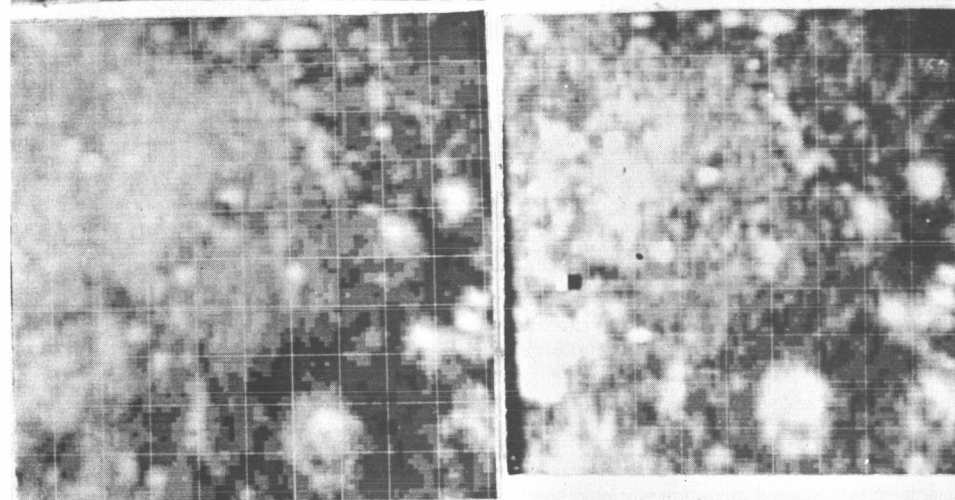


Plate XXXII

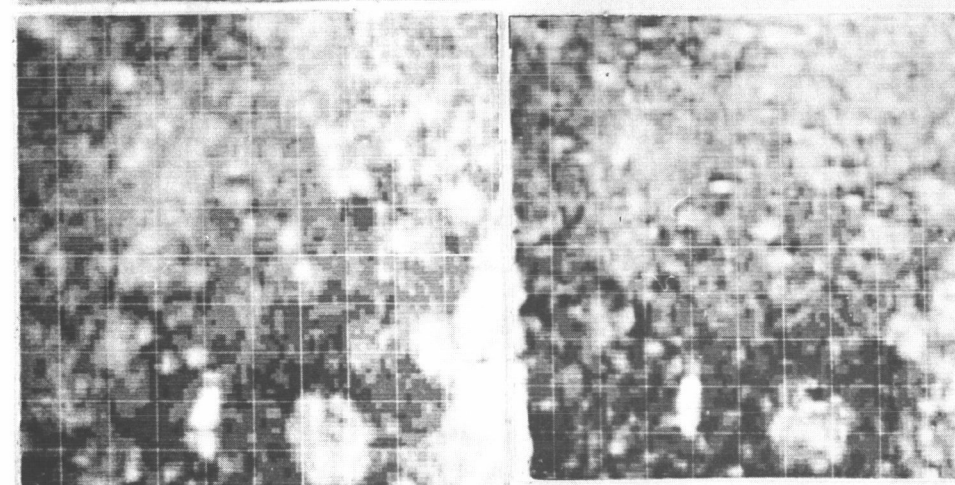
Depolarized



Polarized



Ratio



INDEPENDENT MAPS OF LAC 25 CASSINI

Longitude = -14° , 10° Latitude = 32° , 48°

Observations (a) 17 April 1967, (b) 24 January 1967

The isometric plots of the depolarized maps are shown in Plate xxxii. The bright and dark squares in the western portion of (b) resulted from parity errors in the computer processing.

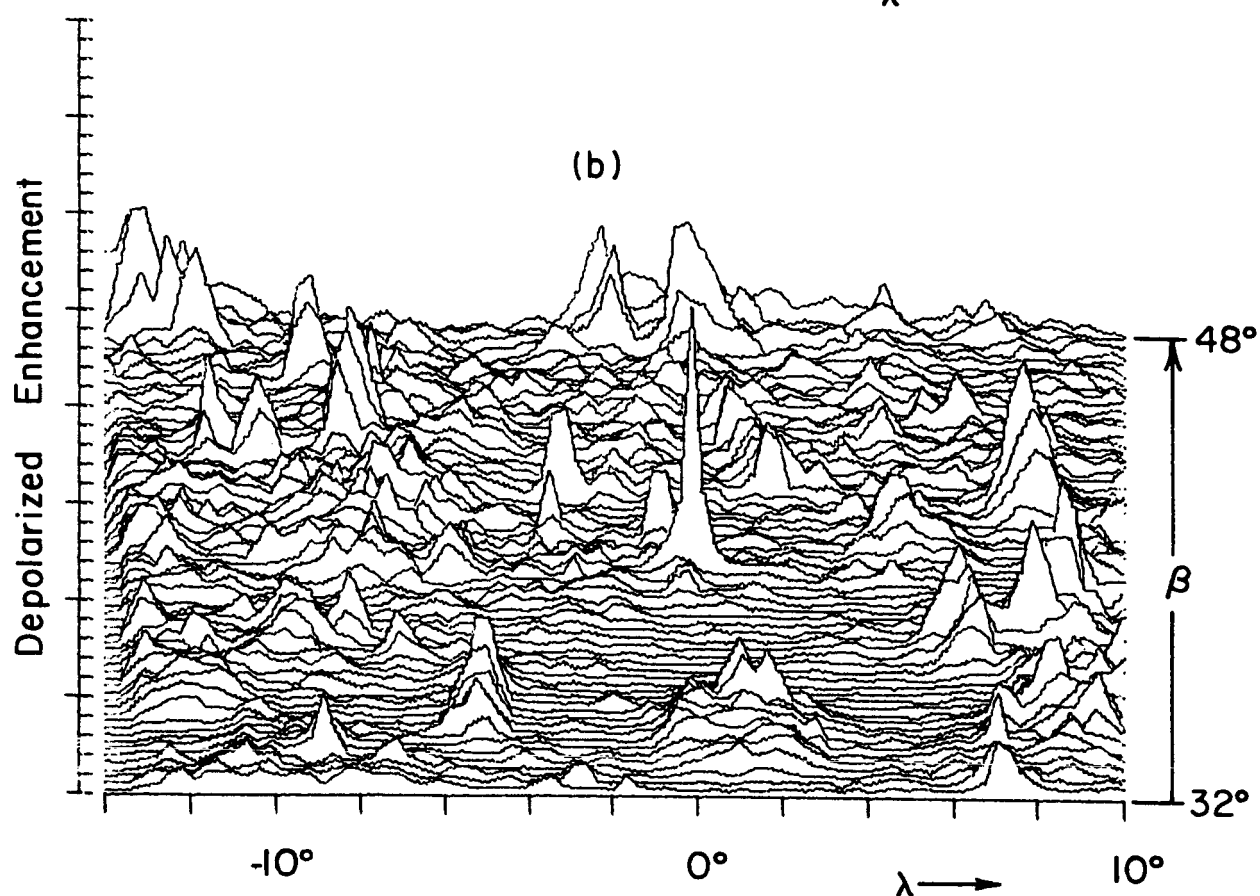
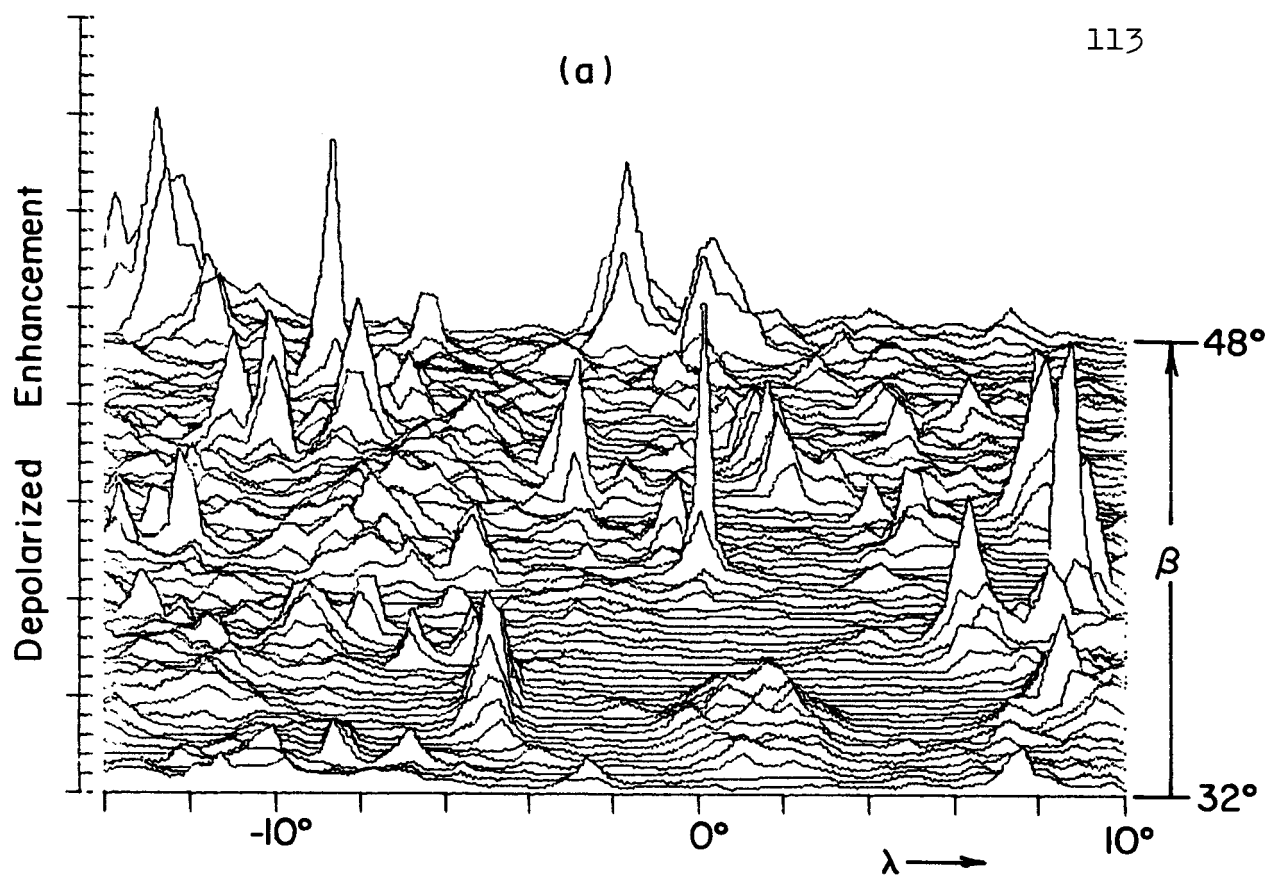


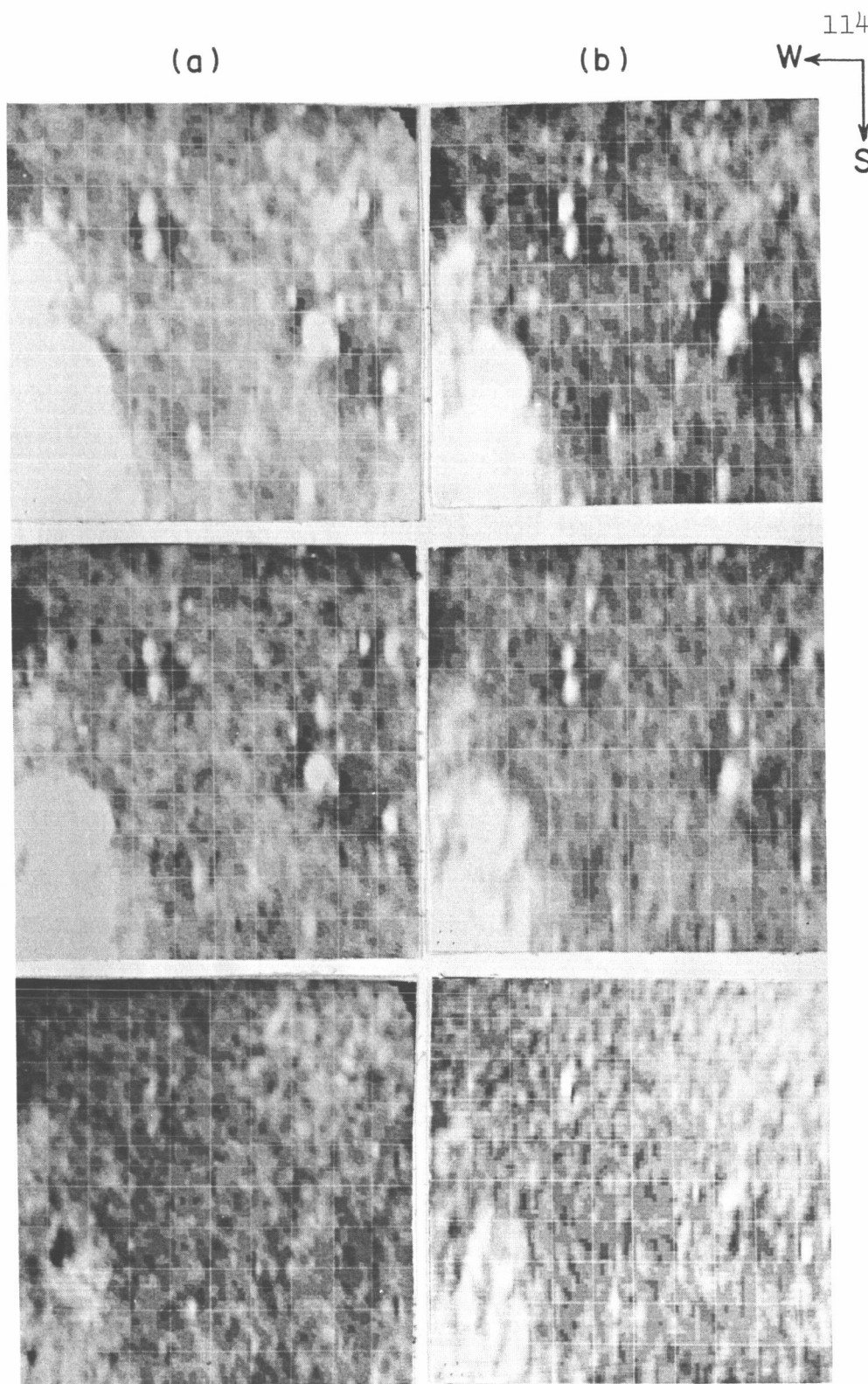
Plate xxxii. Isometric Plots of Depolarized Echoes from Area of Map LAC 25 Cassini: (a) 17 April 1967; (b) 27 January 1967.

Plate XXXIII

Depolarized

Polarized

Ratio



INDEPENDENT OBSERVATIONS OF LAC 56 HEVELIUS

Longitude = -70° , -50°

Latitude = 0° , 16°

Observations (a) 18 February 1967, (b) 3 July 1967

The isometric plots of the polarized maps are shown in Plate xxxiii.

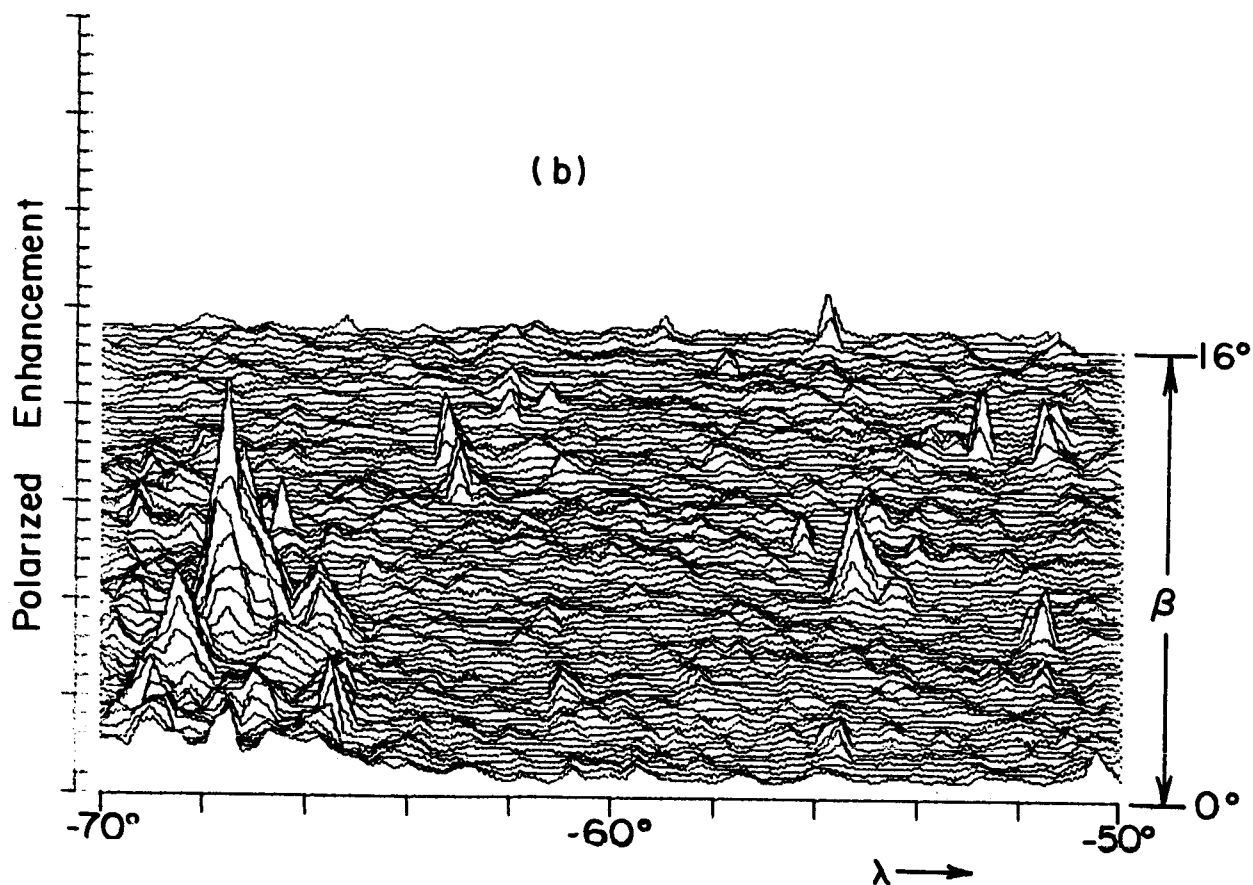
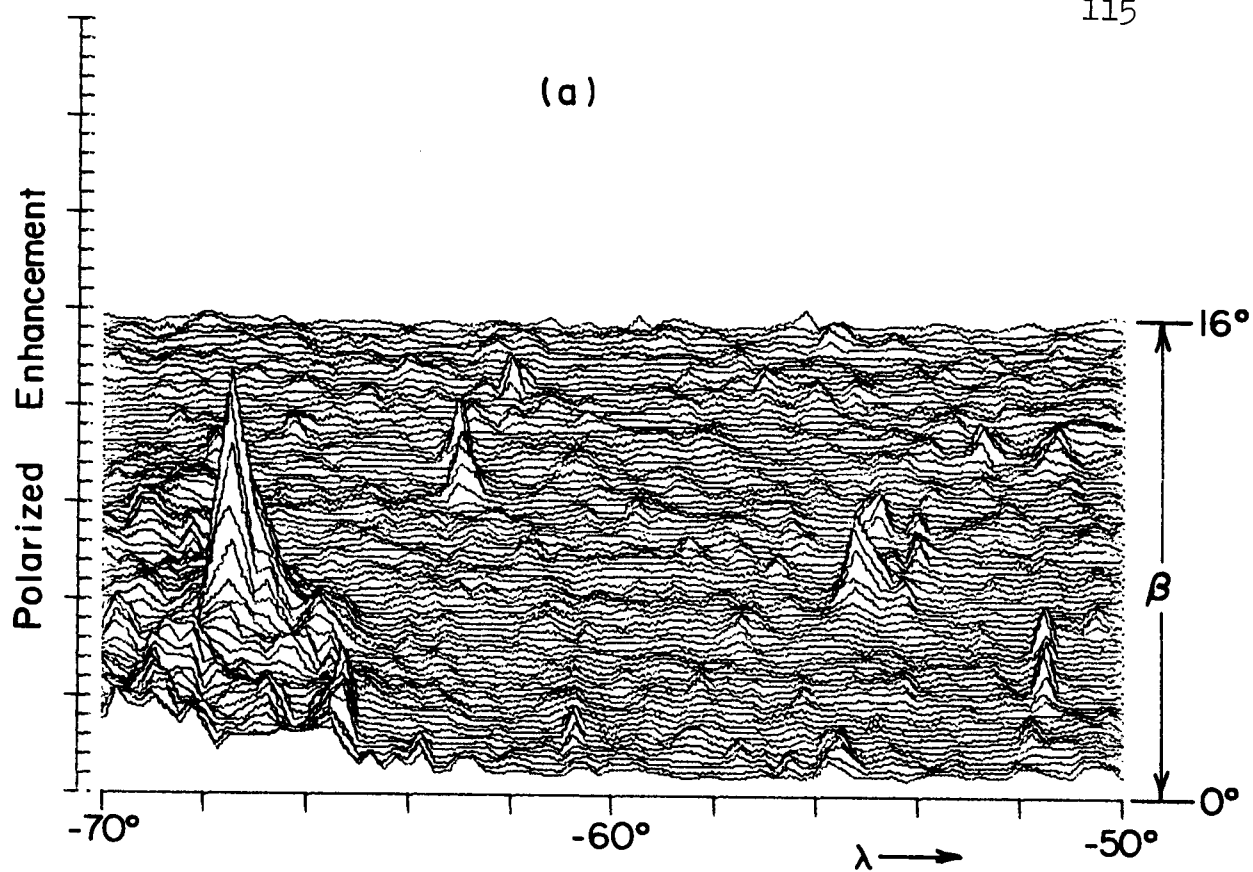
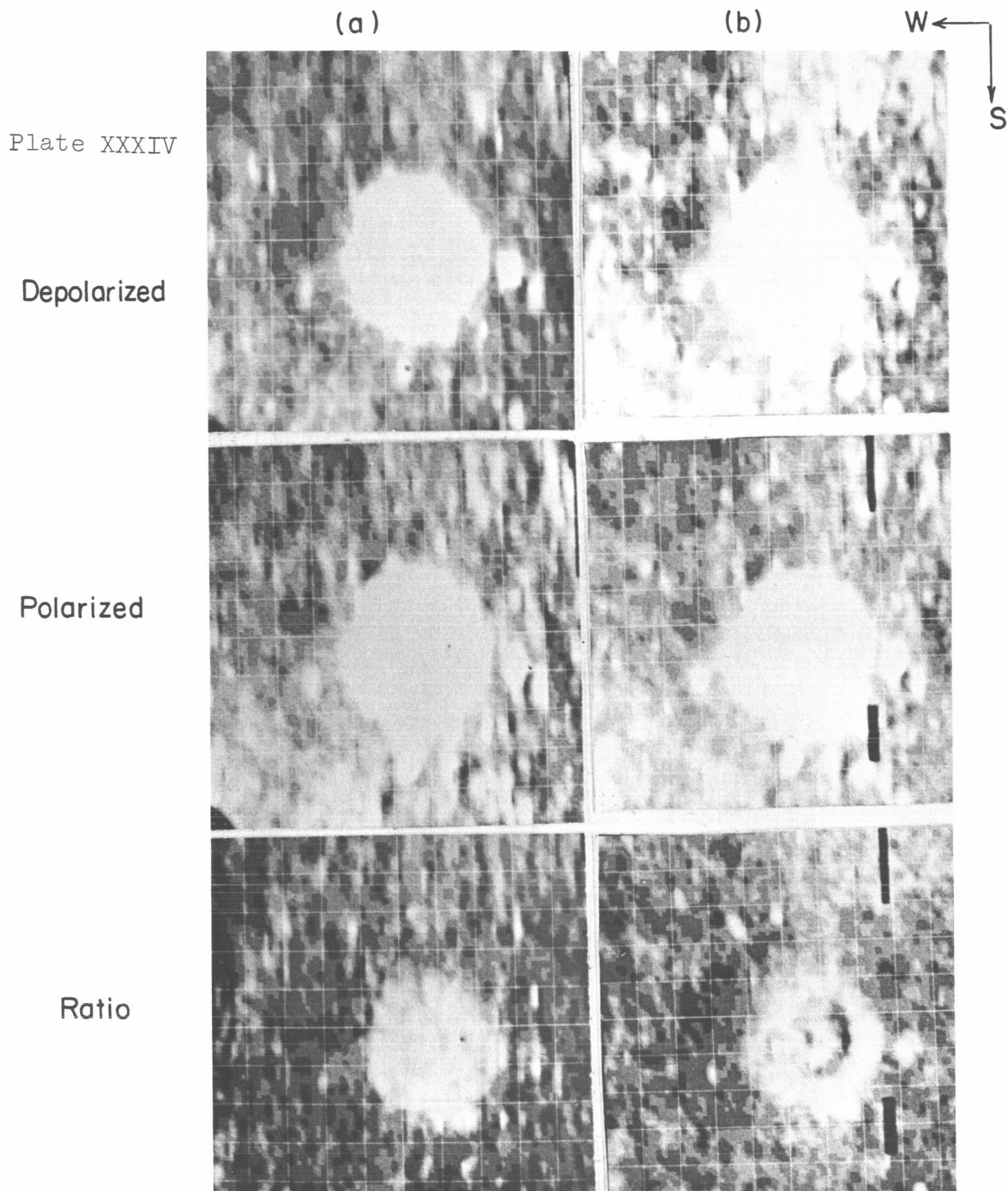


Plate xxxiii. Isometric Plots of Polarized Echoes from Area of Map LAC 56 Hevelius: (a) 19 February 1967; (b) 3 July 1967.



INDEPENDENT OBSERVATIONS OF LAC 80 LANGRENUS

Longitude = 50° , 70° Latitude = -16° , 0°

Observations (a) 18 Feb. 1967, (b) 3 July 1967

The isometric plots of the depolarized maps are shown in Plate xxxiv. The black strips in the polarized and ratio maps of (b) resulted from parity errors in the computer processing.

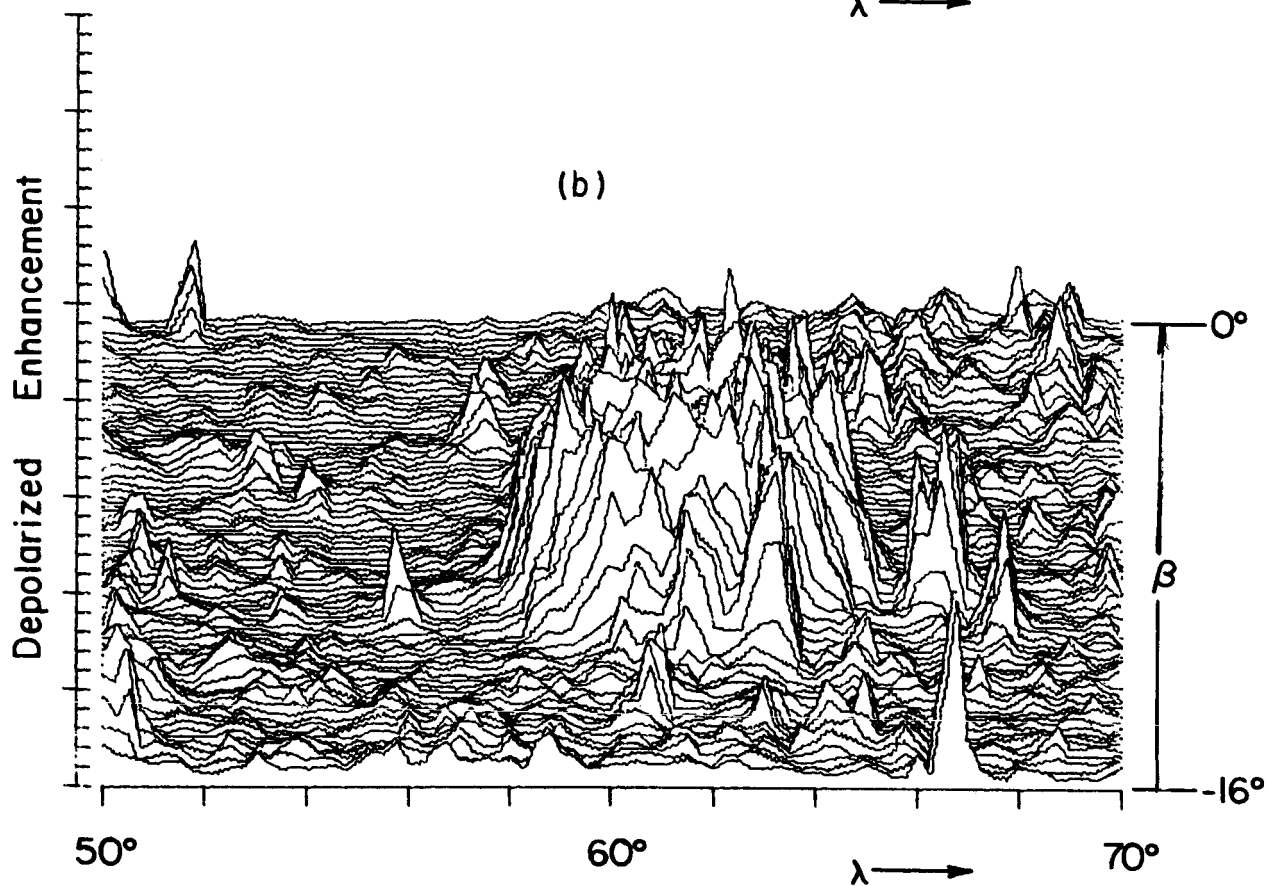
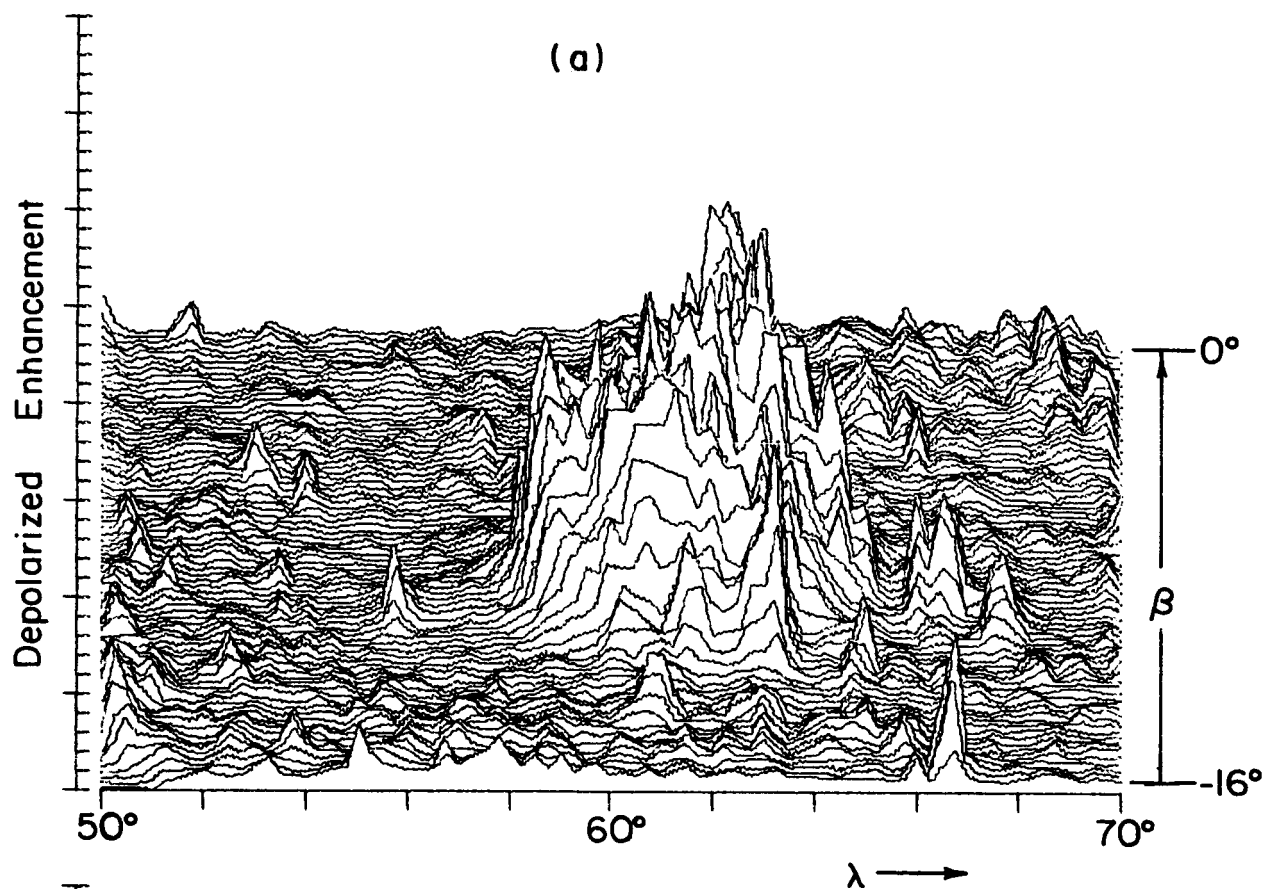


Plate xxxiv. Isometric Plots of Depolarized Echoes from Area of Map LAC 80 Langrenus: (a) 18 February 1967; (b) 3 July 1967.